



Universität für Bodenkultur Wien

Department of Water, Atmosphere and
Environment

Institute of Meteorology

Head: Ao.Univ.Prof. Dipl.-Ing. Dr.nat.techn. Josef
Eitzinger

Advisor: Ao.Univ.Prof. Mag.rer.nat. Dr.rer.nat. Philipp
Weihs

SPECTRAL SIMULATION TOOLS AS VALID
INSTRUMENTS TO DETERMINE SPECTRAL EFFECTS
ON PHOTOVOLTAIC SYSTEMS

Dissertation

for obtaining a doctorate degree

at the University of Natural Resources and Applied Life
Sciences Vienna

Submitted by

Dipl.-Ing. Giorgio Belluardo

Vienna, April 2016

Acknowledgements

I am thankful to my supervisor, Prof. Philipp Weihs, for accepting me as a doctoral student, and for his useful suggestions and helpfulness, that were important for the realization of this work.

I would like to thank my colleagues of the Institute for Renewable Energy of EURAC for all their tips and their support. Special thanks go to David Moser, who believed in me and in this doctoral work even before its start. In this regard, I am also thankful to the European Regional Development Fund (ERDF) for providing me with financial support through the Project 2-1a-97 "PV Initiative".

I would also like to thank the Photovoltaics Group of the Energy Department of AIT Vienna: a great crew, always keen on helping each other. My particular thanks go to Marcus Rennhofer, who contributed with new ideas, methodologies, and in revising this thesis. I would like to express my thanks to Josef, Jochen and his nice family, who made my temporary stay in Vienna very enjoyable.

A special thanks to Katrin, her family and all my family: their love and care motivate me in doing well every day!

Abstract

The spectrum of incoming sunlight affects the generation of current and the performance of photovoltaic (PV) systems. The magnitude of these spectral effects depends upon the PV technology (and in particular its spectral response) and the characteristics and variability of the solar spectrum in a specific location.

The present doctoral work is focused on the development of a novel methodology to evaluate and take account of spectral effects in PV systems, in order to increase the accuracy of the estimation of the loss of performance that gradually occurs during their lifetime.

This novel methodology can make use of either measured or simulated solar spectra. The presence of a spectroradiometer in proximity to a PV installation is rather rare, since these instruments are costly and their correct setting and maintenance is demanding. Therefore, the use of radiative transfer models (RTM) to simulate solar spectra is increasing. This study also attempts to deepen knowledge in the use of these simulation tools. On the one hand, an evaluation is made of how the use of different RTM and of different sources of input parameters affects the simulation results. On the other, a systematic and rigorous analysis of RTM uncertainty is carried out using the Monte Carlo statistical technique.

The doctoral work has been developed in six publications: three have been published in peer-review journals and three in conference proceedings. Summarizing the results of all the publications, it can be stated that spectral simulation tools are a good and reliable alternative to spectral measurements when the input parameters fed into the model are measured, or retrieved from satellite with high temporal frequency and spatial resolution. They can be therefore used in the photovoltaic sector to detect and evaluate spectral effects on existing or planned PV systems. In particular, it is demonstrated that a method for the estimation of the performance loss rates that takes spectral effects into account represents an improvement compared to other common methodologies, especially for crystalline-silicon based technologies.

The present study contributes to evaluate and reduce uncertainty in the estimation of the solar radiation available for conversion into electricity, and of the performance losses of PV systems. This is in turn beneficial for the entire PV value chain and, in the last instance, for the bankability of photovoltaic projects.

Keywords: spectral effect, spectral irradiance, radiative transfer model, performance loss, photovoltaic system.

Table of contents

1	Introduction	7
1.1	Motivation	7
1.2	Spectral measurements	8
1.3	Overview of radiative transfer models for spectral simulation	10
1.4	Indexes of spectral quality	11
1.5	Interaction of a PV device with the solar spectrum	12
2	List of publications	14
3	Overview of publications and their relation to the topic	15
4	Conclusions and outlook	17
5	References	19
6	Publications	23
6.1	Publication I	23
6.2	Publication II	30
6.3	Publication III	45
6.4	Publication IV	57
6.5	Publication V	67
6.6	Publication VI	80
7	CV	95

1 Introduction

1.1 Motivation

Photovoltaic (PV) modules (also commonly called *devices*) deployed outdoors are subject to variable sets of environmental conditions that very often deviate from the set of conditions of the so-called *Standard Test* (IEC60904-3:2008, 2008) performed to rate their power at the end of the production process. The deviation of each environmental factor from the corresponding Standard Test reference value generates an *effect* in terms of gain or loss of performance with respect to the reference rated power. The major effects influencing the behaviour of a PV device or system are:

- Irradiance effect. This is generated when the plane-of-array irradiance impinging the PV device differs from the standard value of 1000 W/m^2 . An increase of irradiance corresponds primarily to an increase of short-circuit current I_{sc} of the PV device, thus determining an increase of power output. A secondary effect is the so-called *light soaking*: depending on the technology, the power output measured under fixed environmental conditions gradually increases or decreases after its initial exposure to light and stabilizes after a certain value of cumulated radiation. The process can be either reversible or irreversible.
- Temperature (or thermal) effect. This is generated when the PV device temperature differs from the standard value of $25 \text{ }^\circ\text{C}$. A primary effect consists of a reduction of the open circuit voltage V_{oc} , and therefore of generated power, at increasing temperatures. A secondary effect, visible mainly in amorphous silicon technology and countering the primary effect, is the so-called *thermal annealing*. At increasing temperatures (approx. $>50^\circ\text{C}$), the internal structure of the semiconductor changes in such a way that it is able to improve its performance compared to a device operating at the same irradiance and kept cool.
- Reflection effect. This is the light lost by reflection from the flat surface of a PV module. In particular, reflection effects are null when the angle of incidence (AOI) of light, i.e. the angle between the sunbeam and a line perpendicular to the module's surface, is 0° . They increase at increasing values of AOI of light, and are particularly evident at AOIs higher than 55° (King et al., 2004).
- Spectral effect. This is generated when the spectrum of solar irradiance differs from the standard spectrum ASTM G173-03 AM 1.5 (ASTM G173-03:2012, 2012). In particular, the deviation concerns the shape of the spectrum, i.e. the distribution of irradiance depending on wavelength, rather than the integral value (this corresponds to the irradiance effect). PV technologies can react in different ways to the same incoming spectrum, depending on their spectral response, as will be explained in Chapter 1.5. Therefore, spectral effects can be either positive or negative.

The doctoral work focuses on spectral irradiance and spectral effects. The solar spectrum varies over time, depending not only on the geometrical position of the sun with respect to a PV device, but also and especially on the atmospheric composition and on the meteorological conditions. For this reason, a specific PV technology is subject to different strengths of spectral effects depending on its location on the Earth's surface. If the solar spectrum differs significantly between locations, this can also generate substantial differences in energy generation. Several authors have studied this topic in recent years and quantified gains or losses in several locations on a monthly or annual time basis (Alonso-Abella et al., 2014; Amillo et al., 2015; Behrendt et al., 2013; Dirnberger et al., 2015; Gottschalg et al., 2003; Ishii et al., 2011, 2013; Martín and Ruiz, 1999; Schweiger et al., 2012; Virtuani and Fanni, 2014; Pierro et al., 2015). Just to cite some results and with no aim to fully cover this topic, Alonso-Abella et al. (2014) quantified spectral effects on amorphous silicon-based PV systems to vary between -16% and $+4\%$ and between -3% and $+6\%$ on a monthly basis for, respectively, Stuttgart (Germany) and Tamanrasset (Algeria). On a yearly basis, this turns into -0.35% and $+2\%$ for the two locations. The overall results demonstrate that this effect, though variable in intensity depending on the specific PV technology and location, is not negligible. On the other

hand, the bankability of solar PV projects strictly depends upon an accurate forecast of the energy generated by a PV system and must therefore rely on an accurate forecast of all occurring losses, especially on large scale systems (MW scale). Therefore, it is clear that a reliable assessment of all the effects influencing the behaviour of a PV system is enormously important for the success of such projects and the attraction of capital to the PV sector.

In order to assess spectral effects properly, information about the spectral distribution of light received by a PV module is fundamental. However, measuring the spectrum is expensive and difficult. Spectroradiometers' price ranges from around €10,000 to more than €60,000 depending on the technology, their reliability and their accuracy, and need special expertise in calibration, instrument positioning, software set-up and maintenance. For these reasons, PV plants equipped with spectroradiometers are very rare and usually exploited only for scientific purposes. This problem can be overcome by using tools to simulate the solar spectrum, i.e. the radiative transfer models (RTM). Nowadays many computer software implementing RTMs are available, also for free. In general many studies have proven their accuracy by comparing simulation results with real outdoor measurements, to the point that they have been increasingly considered as a valid substitution for (and, in some cases, as a valid control of) spectral measurements. However, their use and application, although facilitated in some cases by user-friendly interfaces, demand knowledge of atmospheric physics.

Following the series of publications, which are introduced in Chapter 2 and discussed in Chapter 3, two main goals are pursued.

- The first goal is to investigate the use of spectral simulation tools to detect and quantify the spectral effects of different PV systems composed of modules based on different PV technologies. In particular, it is shown how spectral effects can be accounted for within an improved methodology for the estimation of the performance loss rate of the PV systems themselves.
- The second goal is to focus on radiative transfer models themselves, in particular on the relation between the accuracy of results (in comparison with spectral measurements) and the quality of input parameters. Furthermore, the uncertainty of one simulation software is evaluated using the Monte Carlo statistical method, since the equation implemented and solved within the RTM cannot be treated with the classical law of error propagation.

1.2 Spectral measurements

Spectroradiometers are instruments for the measurement of spectral irradiance, i.e. the power density at every wavelength of the light received by a surface and expressed in W/m^3 in SI, or commonly in $W/m^2/nm$ or in $W/m^2/\mu m$. There are two main families of instruments: scanning spectroradiometers (or monochromators) and array detector spectroradiometers (or polychromators).

Both types have input optics, such as integrating spheres, cosine correctors or Teflon diffusers, which collect and guide light to the internal part of the instrument. In some cases, optical fibres are used to connect optics with the instrument bench. The choice of the input optic type and material, as well as of the optical fibre length and diameter affects the portion of the spectrum and the amount of radiation reaching the instrument.

Before entering the optical bench, light passes through an entrance slit that defines a clear-cut object and determines the amount of light as well as the angle of entrance. These factors are in turn directly related to the resulting spectral resolution of the instrument.

The central part of a spectroradiometer is the grating, an element that diffracts the incoming light into its spectral components. In the case of scanning spectroradiometers, the grating rotates in order to diffract one specific wavelength at a time, i.e. to allow only photons of a certain wavelength to reach the next detector element. A continuous rotation is performed in order to scan a range of wavelengths. For this reason, scanning spectroradiometers are equipped with mechanically moving parts that must be protected with stable housing, and are therefore usually heavier and more difficult to transport. In some cases such instruments are equipped with a double monochromator, which considerably decreases the effect of stray light,

thus increasing optical performance. In the case of array detector spectroradiometers, the diffraction gratings are treated in such a way that they simultaneously produce multiple images corresponding to several wavelengths. This can be obtained either with ruled gratings (parallel grooves on the grating surface) or holographic gratings (with sinusoidal index of refraction variation). Polychromatic gratings are not supposed to move. For this reason, these instruments are smaller and lighter than the ones using rotating monochromators, thus more suitable for transportation. Another difference in the two types of instruments is the acquisition time. Due to the rotation of the grating, it takes some minutes for a monochromator to span the whole detectable spectral range. The acquisition time is much smaller, in the order of few microseconds to seconds, for a polychromator since the detection of the light is simultaneous. Consequently, polychromators are less prone to distortion in the measured spectra caused by rapidly varying meteorological conditions, such as the quick passage of a cloud.

The single (in the monochromator case) or multiple (in the polychromator case) detector elements convert the energy of the incoming portion of light into a signal intensity value with the support of a dedicated software. The detector material determines the upper wavelength limit that can be detected by the instrument. The most commonly used materials are Si and InGaAs that can detect up to 1117 nm and 1700 nm, respectively (BW Tek, 2016). Other materials with lower bandgap energy can provide detection limits of 2200 nm to 2600 nm but they are much more expensive. Monochromators usually use a photomultiplier tube (PMT) as detector, while polychromators' array of pixels can consist either of a charge coupled device (CCD) or an array of photodiodes (DAD).

The spectra measured by spectroradiometers are affected by different sources of noise:

- readout noise: caused by the characteristics of the internal elements and their operation;
- shot noise: associated with statistical variation in the number of photons incident on the detector;
- dark noise: associated with the thermal generation of electrons also in absence of incident light;
- fixed pattern noise: caused by variation in photo-response between neighbouring pixels.

Some of the noise can be minimized by changing acquisition settings with the dedicated software or regulating external factors (ambient temperature). In other cases, noise is related to factors intrinsic to the instrument, such as the characteristics and mutual connection of the elements it is composed of, and cannot therefore be modified. For this reason, the proper setting and use of a spectroradiometer is quite complex and experience is required also for validating measured spectra.

In order to overcome the above-mentioned complexity and increase mutual knowledge exchange, several intercomparisons of spectral measurements have been organized in different parts of the world. From an historical point of view, high interest in the ultraviolet (UV) part of the solar spectrum due to its effects on human health explains the high number of intercomparisons which focused on this spectral region (McKenzie et al., 1993; Seckmeyer et al., 1994, 1995; Thompson et al., 1997; Bais et al., 2001; Lantz et al., 2002; Bais et al., 2005; Blumthaler et al., 2008; Gies et al., 2015). As for spectral irradiance measurements at the Earth's surface in other spectral regions, interest has risen in the last decade, driven by the important implications for the PV sector. Therefore, some recent intercomparison campaigns have focused also on the sensitivity regions of photovoltaic materials, such as visible and near infrared. The main campaigns are listed in Table 1. Results show in general that differences between measurements obtained with different spectroradiometers are usually well within a $\pm 10\%$ range. Nevertheless, greater differences can exist in some cases, due to issues in instrument setting and management procedures as well as in measurement and calibration procedures.

Table 1: List of intercomparison campaigns of spectroradiometers for the measurement of solar spectrum at spectral regions of interest for photovoltaic applications. GHI: global horizontal irradiance, DNI: direct normal irradiance. SM: single-monochromator, DM: double-monochromator, P: polychromator.

Reference	Krawczynski et al. (2009)	Martínez-Lozano et al. (2003)	Habte et al. (2014)	Galleano et al. (2014)	Galleano et al. (2015)
Year	not reported	1999	2013	2011	2012
Place	Loughborough, UK	El Arenosillo, Spain	Golden, USA	Portici, Italy	Catania, Italy
Measured component	GHI	GHI, DNI	GHI	GNI, DNI	GNI, DNI
Number of instruments	7	4	10	6	7
Spectral range (nm)	350 - 1050	400 - 700	380 - 1100	360 - 1700	360 - 1700
Instrument type	P	SM, DM, P	SM, DM, P	SM, P	SM, P

1.3 Overview of radiative transfer models for spectral simulation

Radiative transfer models calculate the flow of electromagnetic radiation through a planetary atmosphere, such as the Earth's. The main difference between the available models is in the way they treat the process of interaction of electromagnetic radiation with atmospheric constituents and surfaces, consisting of emission, scattering, absorption and reflection. In general, three categories of RTM are identified.

The first category is represented by the so-called *sophisticated rigorous models*. These are based on the translation into mathematical terms of the radiative transfer equation (RTE), which describes the physical process of radiation transfer (Smith, 1985). A solution of RTE is then calculated numerically for each spectral wavelength using a discrete ordinate method. These models are made up of different parts, usually consisting in:

- an input manager that translates the atmospheric description (constituent profiles or quantities, meteorological variables etc.) into optical properties;
- a RTE solver, which is the core of the model;
- a post-processing manager, which performs further processing of the results obtained (convolution of spectra, spectral translation to tilted and oriented planes etc.).

Since the process of molecular absorption is treated as the sum of the contributions of the spectral lines of each gas species or aerosol constituting the atmosphere, these models are often called *line-by-line models*. An advantage in using such models is their high accuracy. On the other hand, execution time can be very high. Examples of such models are LOWTRAN (Kneizys et al., 1988), MODTRAN (Anderson, 1993; Berk et al., 1989), SBDART (Ricchiazzi et al., 1998), SBMOD (Yang et al., 1999), STREAMER (Key and Schweiger, 1998), FASTCODE (Clough et al., 1981), UVSPEC (Kylling, 1992). In particular, in this doctoral work mainly the RTE solvers DISORT (Stamnes et al., 1988) and SDISORT (Dahlback and Stamnes, 1991) have been used, which are implemented in the tool UVSPEC and included in the libRadtran software package (Mayer and Kylling, 2005). In order to decrease computation time, some of the above-mentioned models allow simplifications. One of the most common is the so-called *correlated K-distribution approximation*. Since the same set of values of gaseous absorption coefficients is encountered many times over a given spectral interval, or band, computation redundancy is eliminated by grouping these values. For example, the correlated-k approach of Kato et al. (1999) works with 32 bands in the whole solar spectrum. This way,

the transmittance calculation is performed only once for a given band, instead of once for each wavelength. Another important simplification is performed with the algorithm implemented in MAGIC (Mueller et al., 2009) and SPECMAGIC (Mueller et al., 2012). This method makes use of the so-called *lookup tables* (LUTs), which are discrete pre-computed radiative transfer model results. Once LUTs are available, the transmittance for a given atmospheric state can be extracted from the LUTs by interpolation, thus replacing a runtime computation. For this reason, MAGIC and SPECMAGIC cannot be considered as proper RTMs, but rather methods that use RTM calculations indirectly.

The second category of RTM consists of the so-called *parametrised models*. These are simpler tools than rigorous models because the different complex extinction processes of the radiative transfer equation are replaced by simple parametrized expressions. They have appeared in the literature since early 1980s with the aim of providing at hand solutions for engineering applications with low irradiance computation times, user-friendly interfaces and still acceptable accuracy. Examples of such models are SPCTRAL2 (Bird, 1984), SEDES (Nann and Riordan, 1991), SMARTS1 (Gueymard, 1993) and SMARTS2 (Gueymard, 1995).

The third category of RTM includes models that use the Monte Carlo statistical method. The interaction of photons with the atmospheric constituents is treated as a statistical process: random photons are emitted into the medium, and after a random distance depending on the mean free path length, they are absorbed or randomly scattered until they eventually leave the domain. Interaction lengths, scattering angles and absorption rates are determined on the basis of probability density functions chosen by the user. During the whole process the photons are tracked one by one, and are counted as they possibly exit the medium in order to obtain spectra. Examples of such models are MYSTIC (Mayer, 2009), GRIMALDI (Macke et al., 1997) and BRITE (Blättner et al., 1974).

There are other criteria to distinguish between models, such as wavelength range and resolution, inclusion of light polarization, geometry of the domain, licence type, capacity of treating ice and water clouds, type of generated output, user interface etc. In general, it is not possible to state which is the best model. Instead, depending on the specific application and problem to solve, there are models that are more suitable than others. In any case, numerous efforts have been made and are currently being made in order to compare the results of different RTMs, under different environmental conditions. One of the most famous is represented by the RAdiation transfer Model Intercomparison (RAMI), coordinated by the European Commission's Joint Research Center (Widlowski et al., 2013), which consists of a platform for assessing the capability, performance and agreement of RTMs under a framework of well-established rules and criteria.

1.4 Indexes of spectral quality

Given a solar spectrum, some indexes are available that quantify its shape, i.e. the shift in the distribution of irradiance over the spectrum. The most common ones are the average wavelength (λ_{ave}) and average photon energy (APE).

The average wavelength (Wagner et al., 2011) is the wavelength at which the integral value of spectrum calculated from the lower wavelength limit is exactly half of the broadband irradiance (integral of the spectrum over the entire wavelength range). λ_{ave} satisfies the following equivalence:

$$\int_{\lambda_{min}}^{\lambda_{ave}} G(\lambda) d\lambda = \int_{\lambda_{ave}}^{\lambda_{max}} G(\lambda) d\lambda \quad (1)$$

where $G(\lambda)$ is the spectral irradiance while λ_{min} and λ_{max} are the wavelength range limits of the solar spectrum.

Average photon energy, first proposed by Jardine et al. (2002), is defined as the average energy of all of the photons impinging upon a target surface:

$$APE = \frac{\int_{\lambda_{min}}^{\lambda_{max}} G(\lambda) d\lambda}{q \int_{\lambda_{min}}^{\lambda_{max}} \Phi(\lambda) d\lambda} \quad (2)$$

where q is the electronic charge and $\Phi(\lambda)$ is the photon flux density at wavelength λ , which is in turn calculated using the Planck-Einstein relation as follows:

$$\Phi(\lambda) = G(\lambda) \frac{\lambda}{hc} \quad (3)$$

c and h correspond to the speed of light in a vacuum and to the Planck constant, respectively. Spectra that are shifted towards lower wavelengths correspond to lower values of λ_{ave} and higher values of APE. Spectra that are more pronounced at higher wavelengths correspond to higher values of λ_{ave} and lower values of APE. Although they both describe spectral distribution by synthesizing a single number, the two indexes are not related with a formula.

1.5 Interaction of a PV device with the solar spectrum

The photovoltaic effect consists of the generation of an electric current when a semiconductor p-n junction material is exposed to light. Every semiconductor has a specific band gap. This is the minimum energy required by a photon to excite an electron to pass from the valence band into the conductive band of the material, leaving behind a hole. When a photon has a higher energy than the material bandgap, the electron quickly thermalizes back down to the conduction band edges and the excess of photon energy is turned into heat. If, on the other hand, the photon has less energy than the material bandgap, it is not absorbed by the material, and it passes through it as if it was transparent. A photovoltaic material consists of a semiconductor material that, through a doping process, has been provided with a p-n junction that generates a specific in-built voltage. This voltage is responsible, once the electron and hole (also called *carriers*) have been separated, to sweep them away to an external circuit before they can re-combine. Unfortunately, a generated electron-hole pair is not necessarily guided into the circuit, but this depends on the strength of the in-built voltage and on the distance between the p-n junction and the location of its generation. For example, photons with high energy tend to generate carriers near the surface, further away from the p-n junction, and are therefore more prone to recombination.

In macroscopic terms, the percentage of carriers which is collected by the solar cell with respect to the incoming photons, for each wavelength of the incoming light, is described by the *External Quantum Efficiency* (EQE). It is interesting to note that the EQE depends not only on the material's characteristics, but also on other factors that prevent the light from hitting the material: glass reflection, shading due to electrical contacts etc. The EQE of a solar material has two spectral wavelength limits. The maximum limit is given by the band gap: photons with energy lower than it are not effective and are thus lost. On the other hand, the lower limit depends on the absorption characteristics of the material, which determine surface recombination of carriers generated by high energy photons.

Another parameter used to characterize the efficiency of a solar cell in generating current is the *Spectral Response* (SR). This is defined, for each wavelength of the incoming light, as the ratio of current generated by the solar cell and the power (irradiance) incident on it. It is therefore expressed in A/W . The spectral response of a PV device is measured in laboratory by illuminating the sample with a monochromatic beam and registering the photocurrent generated as a function of wavelength. SR is an intrinsic characteristic of the PV device: given a specific cell technology, it varies from manufacturer to manufacturer depending on the module design and production process. Once the SR is known, it is possible to calculate the expected short-circuit current density of the PV device being tested $J_{SC_{dut}}$ as:

$$J_{sc_{dut}} = \int_a^b G_{in}(\lambda) SR_{dut}(\lambda) d\lambda \quad (4)$$

where $G_{in}(\lambda)$ is the incoming solar spectrum, $SR_{dut}(\lambda)$ is the spectral response of the PV device being tested, while a and b are integration limits that must include the spectral response of the PV device. This formula therefore explains how a PV device reacts to a specific incoming spectral irradiance, by generating an electric current.

As explained in Chapter 1.1, PV devices deployed outdoors are subject to ambient conditions that can sensibly diverge from Standard Test Conditions (STC). When the incoming spectrum is different from the standard spectrum ASTM G173-03 AM 1.5, a difference in power output with respect to standard spectral conditions arises, which is called *spectral effect*. In particular, the spectral effect can result in either higher (spectral gains) or lower (spectral losses) power output than under standard spectral conditions. These gains and losses are quantified with the spectral mismatch factor, defined as:

$$MM = \frac{\int_c^d G_{ref}(\lambda) SR_{ref}(\lambda) d\lambda}{\int_c^d G_{in}(\lambda) SR_{ref}(\lambda) d\lambda} \frac{\int_a^b G_{in}(\lambda) SR_{dut}(\lambda) d\lambda}{\int_a^b G_{ref}(\lambda) SR_{dut}(\lambda) d\lambda} \quad (5)$$

where $G_{ref}(\lambda)$ is the ASTM G173-03 AM 1.5 standard spectrum and $SR_{ref}(\lambda)$ is the reference spectral response, i.e. the spectral response of the device measuring the reference spectrum. If this is a pyranometer, with spectral response curve compared to quartz glass, $SR_{ref}(\lambda)$ is assumed equal to 1 for every wavelength. Integration limits c and d must include the reference spectral response. MM higher than 1 corresponds to spectral gain compared to STC, while MM lower than 1 corresponds to spectral loss.

2 List of publications

The following six publications constitute the scientific research work of the doctoral program.

Publication I

Belluardo, G., Wagner, J.E., Tetzlaff, A., Moser, D., 2013. Evaluation of spectral effect on module performance using modelled average wavelength. Proceedings 28th EU PVSEC, 3561-3566.

Publication II

Belluardo, G., Ingenhoven, P., Sparber, W., Wagner, J., Weihs, P., Moser, D., 2015. Novel method for the improvement in the evaluation of outdoor performance loss rate in different PV technologies and comparison with two other methods. Solar Energy 117, 139-152.

Publication III

Castelli, M., Stöckli, R., Zardi, D., Tetzlaff, A., Wagner, J.E., Belluardo, G., Zebisch, M., Petitta, M., 2014. The HeliMont method for assessing solar irradiance over complex terrain: validation and improvements. Remote Sensing of Environment 152, 603-613.

Publication IV

Belluardo, G., Rennhofer, M., Weihs, P., Pravettoni, M., Strepparava, D., Olefs, M., Baumgartner, D., Moser, D., 2014. Solar spectral characterization of three different locations at Alpine latitudes using Average Photon Energy. Proceedings EuroSun.

Publication V

Belluardo, G., Barchi, G., Baumgartner, D., Rennhofer, M., Weihs, P., Moser, D., 2016. Uncertainty analysis of a radiative transfer model using Monte Carlo method within 280-2500 nm region. Solar Energy 132, 558-569.

Publication VI

Belluardo, G., Barchi, G., Baumgartner, D., Rennhofer, M., Weihs, P., Moser, D., 2016. Uncertainty analysis of a radiative transfer model using Monte Carlo method: impact on PV device calibration parameters. Proceedings 31st Symposium Photovoltaic Solar Energy.

Publication I was published in the proceedings of the 28th European PV Solar Energy Conference and Exhibition in 2013.

Publications II and V were published in the peer-reviewed journal Solar Energy. This is the official journal of the International Solar Energy Society, devoted exclusively to the science and technology of solar energy applications. Journal impact factor 2014: 3.469.

Publication III was published in Remote Sensing of Environment, an interdisciplinary journal on terrestrial, oceanic, and atmospheric sensing. Journal impact factor 2014: 6.393.

Publication IV was published in the proceedings of the International Conference on Solar Energy and Buildings (EUROSUN) 2014, jointly organized by the International Solar Energy Society Europe and INES.

Publication VI was published in the proceedings of the OTTI's 31st Symposium Photovoltaic Solar Energy in 2016.

3 Overview of publications and their relation to the topic

Publication I evaluated the effects of solar spectral variability on five different photovoltaic technologies installed at Bolzano Airport (Italy). As this site is not equipped with a spectroradiometer, the tool SPECMAGIC (Mueller et al., 2012) was used to calculate solar spectra in a one-year period using satellite-retrieved values of atmospheric information as input. Simulations were validated by comparison with values of broadband irradiance measured with pyranometers installed both in the horizontal plane and in-plane with PV modules. The average wavelength was selected as the index to quantify the quality of spectral distribution, while the efficiency of each PV system was selected as the performance index. Performance data were filtered and corrected in order to minimize irradiance, temperature and reflection effects. The correlation of spectral data with the efficiency of the investigated technologies showed clear patterns. In general, the efficiency of thin film technologies (amorphous silicon, micromorph, Cadmium Telluride and CIGS) tends to decrease the more the solar spectrum has red content (red shift). On the other hand, crystalline silicon shows the opposite behaviour, and performs better under red-shifted conditions of solar spectrum. Considering only clear sky conditions, the solar spectrum tends to shift towards higher wavelengths when the value of air mass is higher, i.e. when the solar zenith angle decreases. This happens for example at the time of sunset or during winter, and is more pronounced at higher latitudes. Considering a variation range of the average wavelength in Bolzano of 675 to 725 nm, the maximum efficiency variation was found to be 4.8% for Cadmium Telluride, 10.8% for CIGS, 11.3% for micromorph silicon, 26.2% for amorphous silicon and 2.1% for polycrystalline silicon.

The methodology used in Publication I to detect spectral effects on PV technologies was further exploited in **Publication II** to correct the performance data of outdoor-deployed PV systems to ASTM G173-03 AM 1.5 spectral conditions. In fact, if all the external factors affecting the performance of a PV system (irradiance, temperature, solar spectrum, angle of incidence etc.) are isolated and data are duly filtered and corrected in order to eliminate their effect on PV system performance, what remains is the pure performance ascribable only to PV system behaviour, dependent upon the material and its natural degradation. In this way it was possible to identify a gradual loss of performance of the PV system as time passes. Publication II therefore presents a novel method for the calculation of the performance loss rate of a generic PV system by including data correction for spectral effects. It was demonstrated that adding spectral correction to irradiance and temperature correction reduces uncertainty in the evaluation of performance rate by 25% on average. This novel method was then compared with other well-established metrics, resulting in lower values of associated uncertainty when it was applied to crystalline-silicon based PV technologies, and comparable values of associated uncertainty for thin film technologies.

Publication III was dedicated to the validation of the HeliMont method (Stöckli, 2013), which uses SPECMAGIC for the calculation of solar spectra, to assess irradiance over extensive and complex terrains. SPECMAGIC (Mueller et al., 2012) is conceived to receive continuous and extensive data retrieved from Meteosat Second Generation (MSG), in particular monthly climatological values of atmospheric aerosol properties. It was therefore interesting to explore other simulation tools, such as UVSPEC (Kylling, 1992) with the radiative transfer equation solver DISORT (Stamnes et al., 1988), that allow the inclusion of input values measured by or retrieved from satellites with a higher frequency (e.g. daily averages). The article showed that using daily averages of aerosol optical depth (AOD), single scattering albedo and precipitable water measured on site with a sunphotometer belonging to the AERONET network (Holben et al., 1998), the irradiance values simulated with DISORT are closer to irradiance measurements than SPECMAGIC. Furthermore, also DISORT simulations performed using daily averages of AOD retrieved from the MODIS instrument mounted on board Terra and Aqua satellites (Levy et al., 2007) are more accurate than SPECMAGIC. It is therefore clear that it is preferable to use ground-measured values of atmospheric constituents (especially aerosol properties), coupled with a suitable radiative transfer equation solver like DISORT or SDISORT (Dahlback and Stamnes, 1991), when they are available. If this is not the case, satellite-retrieved input

parameters should be chosen that are available with a high frequency (at least daily values - like MODIS), and possibly with a high spatial resolution. The last assumption is particularly true in mountain areas. In this sense, the authors suggested for example the use of aerosol properties from re-analysis projects like MACC (Inness et al., 2013), which provides data by integrating satellite and in-situ measurements.

A further detailed confirmation of the former results was shown in **Publication IV**. Here, the spectral data from three different locations in the Alpine region (Kanzelhöhe, Vienna and Lugano) were compared to simulations performed again with the tool UVSPEC coupled with the radiative transfer equation solver DISORT, for specific clear-sky winter and summer days. Aerosol input parameters were selected according to their availability for the site. For example, when an AERONET station was available with good data quality, measurements of aerosol parameters were used. If not, daily averages of aerosol parameters from MODIS retrievals were used. When neither aerosol measurements nor satellite-retrieved were available, fixed values were used. Measurements and simulations were compared on the basis of solar spectral quality by means of the Average Photon Energy index. Results showed that simulations performed using ground measurements of aerosol are in better agreement with measurements than simulations performed with satellite-retrieved aerosol. The same work also showed the daily and seasonal variability of the APE index calculated from measured spectra, in the three different locations.

Results found in Publications III and IV suggest DISORT, or its version for spherical atmospheric geometry, SDISORT, as reference radiative transfer equation solver due to its ability to accept ground measurements with high temporal resolution as input. Furthermore, DISORT and SDISORT are flexible and allow simulations under cloudy-sky conditions, if reliable cloud information is available. On the other hand, the drawback of high computation time is overcome by using a correlated K-distribution approximation and by exploiting the High Performance Computing (HPC) system offered by the Vienna Scientific Cluster (VSC, 2015). Results published in Publication I and II are based on simulations performed with SPECMAGIC. It would be interesting to repeat the calculations using DISORT or SDISORT in order to improve their accuracy, while the methodologies developed in these publications remain valid.

Due to the current increasing spread of simulation tools as a valid substitution for expensive and maintenance-demanding spectroradiometers, the further research was focused on a deeper analysis of radiative transfer models (RTM). In particular, **Publication V** evaluated the uncertainty associated with the radiative transfer equation solver SDISORT, implemented in the RTM UVSPEC, by using the Monte Carlo statistical technique instead of the classical propagation of error with the sum of squares. The uncertainty was propagated from SDISORT input parameters to SDISORT-generated spectral and broadband irradiance, and minimum and maximum levels of uncertainty were identified that took different possible combinations of atmospheric constituents into account. For example, the uncertainty of broadband global horizontal irradiance due to the simultaneous propagation of the uncertainty of all selected input parameters was found to be between 2.9% and 5.9%. This is higher but still comparable to the uncertainty values typical of common spectroradiometers for outdoor spectral measurements.

Finally, **Publication VI** continued the logic development and investigation path of Publication V. The uncertainty of SDISORT-generated spectral irradiance was further propagated to parameters that directly derive from spectral irradiance. In particular, two parameters were selected that are important for the calibration of PV devices: the short-circuit current I_{sc} and the spectral mismatch factor MM , described in Chapter 1.5. Seven different technologies were selected whose spectral response SR had been measured in laboratory. The results showed that the lowest uncertainty variability occurs for the mono-crystalline silicon technology, the highest for the organic technology, for both parameters.

4 Conclusions and outlook

The solar spectrum affects the performance of a photovoltaic system in a way that depends both on the PV technology and on the spectral variability characterizing the specific location where the PV system is installed. Consequently, it is important to evaluate the spectral effects acting on PV systems in order to be able, for example, to accurately evaluate the natural performance loss occurring during their lifetime. On the other hand, spectral data is rarely measured in proximity of a PV system, due to cost and maintenance issues. Radiative transfer models are valid tools that simulate solar spectra. However, while many studies exist that have evaluated their accuracy by comparison with spectral measurements, a research gap still exists concerning their uncertainty. This is mainly due to the nature of the radiative transfer equation implemented in a RTM that, being nonlinear and not differentiable, does not allow to apply the classical law of propagation of errors.

The main achievements of the doctoral research can be summarized in three elements.

The first important element is the development of a new methodology for the detection of spectral effects in PV systems and for a more accurate estimation of their performance loss rate (PLR). In particular, the analysis has proven that this novel method, which includes corrections of spectral effects in addition to irradiance and temperature effects, is more accurate than other common methodologies for crystalline-silicon based technologies, while it produces comparable results for thin film technologies. In order to increase the accuracy also for the latter technologies (in particular amorphous silicon), some additional and technology-specific effects like light soaking and thermal annealing should be taken into account. In any case, uncertainty in PLR estimation associated with the novel method is on average 25% lower than it is when no spectral correction is performed.

Second, this research has shed light on the use of radiative transfer models, in particular on the relation between the quality of input and the quality of output. This relation is twofold. On one side, several simulations have been performed using different simulation tools and different sources for the model input parameters. Results have demonstrated that tools like UVSPEC, coupled in particular with the radiative transfer equation solvers DISORT or SDISORT, allow more flexibility in the choice of input sources than other tools like MAGIC or SPECMAGIC. In particular, the use of input parameters taken from measurements, as e.g. instantaneous or daily averages of aerosol properties from the AERONET network, ensure the highest level of agreement with spectral measurements. When measured input is not available, the use of satellite-retrieved values of atmospheric constituents ensure good results as well, provided that temporal frequency is high (at least daily averages). Satellite-retrieved data with higher spatial definition than actual MODIS with 10 km resolution, e.g. the new MODIS with 1 km resolution, or re-analysed data from the integration of satellite and in-situ measurements (like MACC project) look promising especially for mountain regions. These results have been achieved by comparing both the integral values of simulated or measured spectra and their shape, quantified with the Average Photon Energy index. However, a complete evaluation of the accuracy of RTMs, i.e. a comparison of simulated and measured spectra that highlights differences at different wavelengths and spectral regions has not been carried out yet. A good opportunity would be the annual intercomparison campaign of spectroradiometers organised by the Joint Research Center (Galleano et al., 2014, 2015). In past editions simulations were included in the campaign, but no extensive comparison of simulation results from different RTMs with spectral measurements was performed. In this sense, a RTM intercomparison might become complementary to the spectroradiometers intercomparison. On a chronological level, this second achievement occurred after the first one. Since the simulation of spectral data used to detect the spectral effects to be included in the novel method for PLR estimation was computed with the tool SPECMAGIC, the analysis could be repeated by using the radiative transfer equation solver DISORT with high temporal resolution of ground measurements of aerosol properties and water column as input.

Finally, the doctoral research has focused on a systematic evaluation of the uncertainty of RTM, specifically of UVSPEC coupled with the radiative transfer equation solver SDISORT. A Monte Carlo approach was applied in order to account for correlations between input

parameters that influence the propagation of uncertainty within the model. As a result, the contribution of each input parameter to the uncertainty of both spectral and broadband irradiance was evaluated in the range 280 nm - 2500 nm. An uncertainty region between a minimum and a maximum limits was determined in order to take different sets of atmospheric conditions that can occur in a location into account. In particular, the uncertainty of global horizontal irradiance calculated with SDISORT was estimated as ranging between 2.9% and 5.9%. These values are lower but still comparable to the typical uncertainty values of common spectroradiometers for outdoor spectral measurements. As a follow-up to these results, also the propagation of uncertainty from spectra simulated with SDISORT to PV device calibration factors (short-circuit current and mismatch factor) of seven different PV systems was analysed. It was shown that the uncertainty tends to amplify when propagating from SDISORT to short-circuit current for all investigated technologies. The uncertainty decreases for all technologies except organic and amorphous silicon when propagating to the spectral mismatch factor.

In general, it is possible to conclude that this doctoral research has:

- encouraged the improvement (reduction) of the uncertainty of measured or satellite-retrieved atmospheric constituents that are used as inputs of radiative transfer models. The reduction of uncertainty in solar resource estimation (both spectral and broadband) has a positive effect on the whole PV value chain, and fosters the bankability of solar energy projects because it reduces investment risks.
- improved the accuracy of methodologies for the estimation of the performance loss rate of PV systems. These methodologies include the use of outdoor PV performance and irradiance values and can be therefore applied also on long time-series of data. This is particularly important as the number of PV systems installed increases and ages, and the need for accurate estimation of their performance loss rate becomes urgently greater.

5 References

- Alonso-Abella, M., Chenlo, F., Nofuentes, G., Torres-Ramirez, M., 2014. Analysis of spectral effects on the energy yield of different PV (photovoltaic) technologies: The case of four specific sites. *Energy* 67, 435–443.
- Amillo, A. M. G., Huld, T., Vourlioti, P., Müller, R., Norton, M., 2015. Application of satellite-based spectrally-resolved solar radiation data to PV performance studies. *Energies* 8 (5), 3455–3488.
- Anderson, S. M., 1993. Ozone absorption cross section measurements in the Wulf bands. *Geophys. Res. Lett.* 20, 1579–1582.
- ASTM G173-03:2012, 2012. Tables for reference solar spectral irradiances: Direct normal and hemispherical on 37° tilted surface.
- Bais, A., Blumthaler, M., Webb, A., Seckmeyer, G., Thiel, S., Kazadzis, S., Redondas, A., Kift, R., Kouremeti, N., Schallhart, B., Schmitt, R., Pisulla, D., Diaz, J. P., Garcia, O., Diaz Rodriguez, A. M., Smedley, A., 2005. Intercomparison of solar UV direct irradiance spectral measurements at Izana in June 2005. In: *Proc. SPIE*, 588609–588610.
- Bais, A. F., Gardiner, B. G., Slaper, H., Blumthaler, M., Bernhard, G., McKenzie, R., Webb, A. R., Seckmeyer, G., Kjeldstad, B., Koskela, T., Kirsch, P. J., Gröbner, J., Kerr, J. B., Kazadzis, S., Leszczynski, K., Wardle, D., Josefsson, W., Brogniez, C., Gillotay, D., Reinen, H., Weihs, P., Svenoe, T., Eriksen, P., Kuik, F., Redondas, A., 2001. SUSPEN intercomparison of ultraviolet spectroradiometers. *J. Geophys. Res. Atmos.* 106, 12509–12525.
- Behrendt, T., Kuehnert, J., Hammer, A., Lorenz, E., Betcke, J., Heinemann, D., 2013. Solar spectral irradiance derived from satellite data: A tool to improve thin film PV performance estimations? *Sol. Energy* 98, 100–110.
- Berk, A., Bernstein, L. S., Robertson, D. C., 1989. MODTRAN: A moderate resolution model for LOWTRAN7. Tech. Rep. GL-TR-89-0122, Air Force Geophysical Laboratory, Hanscom, MA.
- Bird, R., 1984. A simple, solar spectral model for direct-normal and diffuse horizontal irradiance. *Sol. Energy* 32, 461–471.
- Blättner, W., Horak, H., Collins, D., Wells, M., 1974. Monte Carlo studies of the sky radiation at twilight. *Appl. Opt.* 13, 534–537.
- Blumthaler, M., Schallhart, B., Schwarzmann, M., McKenzie, R., Johnston, P., Kotkamp, M., Shiona, H., 2008. Spectral UV measurements of global irradiance, solar radiance, and actinic flux in New Zealand: Intercomparison between instruments and model calculations. *J. Atmos. Oceanic Technol.* 25 (6), 945–958.
- BW Tek, 2016. Spectrometer Knowledge – Part 3a: The detector. <http://bwtek.com/spectrometer-part-3a-the-detector/>, [accessed 2016-11-26].
- Clough, S., Kneizys, F., Rothman, L., Gallery, W., 1981. Atmospheric spectral transmittance and radiance: FASCOD1B. In: *Proc. SPIE, Atmospheric Transmission* 277 (2), 152-166.
- VSC - Vienna Scientific Cluster, 2015. <http://vsc.ac.at/>, [accessed: 2016-02-23].
- Dahlback, A., Stamnes, K., 1991. A new spherical model for computing the radiation field available for photolysis and heating at twilight. *Planet. Space Sci.* 39, 671-683.
- Dirnberger, D., Blackburn, G., Müller, B., Reise, C., 2015. On the impact of solar spectral irradiance on the yield of different PV technologies. *Sol. Energ. Mat. Sol. C.* 132, 431-442.
- Galleano, R., Zaïman, W., Strati, C., Bartocci, S., Pravettoni, M., Marzoli, M., Fucci, R., Leanza, G., Timio, G., Minuto, A., Catena, M., Aleo, F., Takagi, S., Akiyama, A., Nuñez, R., Belluardo, G., 2015. Second international spectroradiometer intercomparison: Results and impact on PV device calibration. *Progr. Photovolt.: Res. Appl.* 23 (7), 929–938.
- Galleano, R., Zaïman, W., Virtuani, A., Pavanello, D., Morabito, P., Minuto, A., Spena, A., Bartocci, S., Fucci, R., Leanza, G., Fasanaro, D., Catena, M., 2014. Intercomparison campaign of spectroradiometers for a correct estimation of solar spectral irradiance:

- Results and potential impact on photovoltaic devices calibration. *Prog. Photovolt: Res. Appl.* 22 (11), 1128–1137.
- Gies, P., Hooke, R., McKenzie, R., O'Hagan, J., Henderson, S., Pearson, A., Khazova, M., Javorniczky, J., King, K., Tully, M., Kotkamp, M., Forgan, B., Rhodes, S., 2015. International intercomparison of solar UVR spectral measurement systems in Melbourne in 2013. *Photochem. Photobiol.* 91 (5), 1237–1246.
- Gottschalg, R., Infield, D., Kearney, M., 2003. Experimental study of variations of the solar spectrum of relevance to thin film solar cells. *Sol. Energ. Mat. Sol. C.* 79 (4), 527–537.
- Gueymard, C., 1993. Development and performance assessment of a clear sky spectral radiation model. In: *Proc. 22nd ASES Conf., Solar '93, Washington D.C., U.S.A.*, 433–438.
- Gueymard, C., 1995. Simple model of the atmospheric radiative transfer of sunshine, version 2 (SMARTS2): Algorithms description and performance assessment. *Tech. Rep. FSEC-PF-270-95*, Florida Solar Energy Center.
- Habte, A., Andreas, A., Ottoson, L., Gueymard, C., Fedor, G., Fowler, S., Peterson, J., Naranen, E., Kobashi, T., Akiyama, A., S., T., 2014. Indoor and outdoor spectroradiometer intercomparison for spectral irradiance measurement. *Tech. Rep. NREL/TP-5D00-61476*, National Renewable Energy Laboratory.
- Holben, B. N., Eck, T. F., Slutsker, I., Tanré, D., Buis, J. P., Setzer, A., Vermote, E., Reagan, J. A., Kaufman, Y. J., Nakajima, T., Lavenu, F., Jankowiak, I., Smirnov, A., 1998. AERONET - A federated instrument network and data archive for aerosol characterization. *Remote Sens. Environ.* 66 (1), 1–16.
- IEC60904-3: 2008, 2008. Photovoltaic devices - Part 3: Measurement principles for terrestrial photovoltaic (PV) solar devices with reference spectral irradiance data.
- Inness, A., Baier, F., Benedetti, A., Bouarar, I., Chabrilat, S., Clark, H., et al., 2013. The MACC reanalysis: An 8 yr data set of atmospheric composition. *Atmos. Chem. Phys.* 13, 4073–4109.
- Ishii, T., Otani, K., Itagaki, A., Utsunomiya, K., 2013. A simplified methodology for estimating solar spectral influence on photovoltaic energy yield using average photon energy. *Energy Sci Eng* 1 (1), 18–26.
- Ishii, T., Otani, K., Takashima, T., 2011. Effects of solar spectrum and module temperature on outdoor performance of photovoltaic modules in round-robin measurements in Japan. *Prog. Photovolt: Res. Appl.* 19 (2), 141–148.
- Jardine, C., Betts, T., Gottschalg, R., Infield, D., Lane, K., 2002. Influence of spectral effects on the performance of multi-junction amorphous silicon cells. In: *Proc. 17th European Photovoltaic Solar Energy Conference and Exhibition, Munich, Germany.*
- Kato, S., Ackerman, T., Mather, J. H., Clothiaux, E., 1999. The k-distribution method and correlated-k approximation for a shortwave radiative transfer model. *J. Quant. Spectrosc. Radiat. Transfer* 62 (1), 109–121.
- Key, J. R., Schweiger, A. J., 1998. Tools for atmospheric radiative transfer: Streamer and FluxNet. *Comput. Geosci.* 24 (5), 443–451.
- King, D., Boyson, W., Kratochvil, J., 2004. Photovoltaic array performance model. *Tech. Rep. SAND2004-3535*, Sandia National Laboratories.
- Kneizys, F., Shettle, E., Abreu, L., Chetwynd, J., Anderson, G., Gallery, W., Selby, J., Clough, S., 1988. Users guide to LOWTRAN7. *Tech. Rep. AFGL-TR-88-0177*, Air Force Geophysics Laboratory.
- Krawczynski, M., Strobel, M., Gottschalg, R., 2009. Intercomparison of spectroradiometers for outdoor performance monitoring. In: *Proc. 24th European Photovoltaic Solar Energy Conference and Exhibition, Hamburg, Germany.* pp. 3406–3408.
- Kylling, A., 1992. Radiation transport in cloudy and aerosol loaded atmospheres. Ph.D. Thesis Alaska University.
- Lantz, K., Disterhoft, P., Early, E., Thompson, A., DeLuisi, J., Kiedron, P., Harrison, L., Berndt, J., Mou, W., Erhamjian, T., Cabausua, L., Robertson, J., Hayes, D., Slusser, J., Bigelow,

- D., Janson, G., Beaubian, A., Beaubian, M., 2002. The 1997 North American interagency intercomparison of ultraviolet spectroradiometers including narrowband filter radiometers. *J. Res. Natl. Inst. Stand. Technol.* 107, 19–62.
- Levy, R. C., Remer, L. A., Mattoo, S., Vermote, E. F., Kaufman, Y. J., 2007. Second-generation operational algorithm: Retrieval of aerosol properties over land from inversion of Moderate Resolution Imaging Spectroradiometer spectral reflectance. *J. Geophys. Res. Atmos.* 112, D13211.
- Macke, A., Mueller, J., Nagel, K., Stuhlmann, R., 1997. A cellular automaton model for cloud formation. In: *Proc. IRS96: Current Problems in Atmospheric Radiation*. pp. 234–237.
- Martín, N., Ruiz, J. M., 1999. A new method for the spectral characterisation of PV modules. *Prog. Photovolt: Res. Appl.* 7 (4), 299–310.
- Martínez-Lozano, J., Utrillas, M., Pedrós, R., Tena, F., Díaz, J., Expósito, F., Lorente, J., de Cabo, X., Cachorro, V., Vergaz, R., Carreño, V., 2003.
- Intercomparison of spectroradiometers for global and direct solar irradiance in the visible range. *J. Atmos. Oceanic Technol.* 20, 997–1010.
- Mayer, B., 2009. Radiative transfer in the cloudy atmosphere. *Eur. Phys. J. Conferences* 1, 75–99.
- Mayer, B., Kylling, A., 2005. Technical note: The libRadtran software package for radiative transfer calculations – Description and examples of use. *Atmos. Chem. Phys.* 5, 1855–1877.
- McKenzie, R. L., Kotkamp, M., Seckmeyer, G., Erb, R., Roy, C. R., Gies, H. P., Toomey, S. J., 1993. First southern hemisphere intercomparison of measured solar UV spectra. *Geophys. Res. Lett.* 20 (20), 2223–2226.
- Mueller, R., Behrendt, T., Hammer, A., Kemper, A., 2012. A new algorithm for the satellite-based retrieval of solar surface irradiance in spectral bands. *Remote Sensing* 4 (3), 622–647.
- Mueller, R. W., Matsoukas, C., Gratzki, A., Behr, H. D., Hollmann, R., 2009. The CM-SAF operational scheme for the satellite based retrieval of solar surface irradiance - A LUT based eigenvector hybrid approach. *Remote Sens. Environ.* 113 (5), 1012–1024.
- Nann, S., Riordan, C., 1991. Solar spectral irradiance under clear and cloudy skies - Measurements and a semi-empirical model. *J. Appl. Meteor.* 30, 447.
- Pierro, M., Bucci, F., Cornaro, C., 2015. Full characterization of photovoltaic modules in real operating conditions: Theoretical model, measurement method and results. *Prog. Photovolt: Res. Appl.* 23 (4), 443–461.
- Ricchiuzzi, P., Yang, S., Gautier, C., Sowle, D., 1998. SBDART: A research and teaching software tool for plane-parallel radiative transfer in the Earth's atmosphere. *Bull. Am. Meteorol. Soc.* 79, 2101–2114.
- Schweiger, M., Ulrich, M., Nixdorf, I., L., R., Jahn, U., Herrmann, W., 2012. Spectral analysis of various thin-film modules using high precision spectral response data and solar spectral irradiance data. In: *Proc. 27th European Photovoltaic Solar Energy Conference and Exhibition, Frankfurt, Germany*. pp. 3284–3290.
- Seckmeyer, G., Mayer, B., Bernhard, G., McKenzie, R. L., Johnston, P. V., Kotkamp, M., Booth, C. R., Lucas, T., Mestechkina, T., Roy, C. R., Gies, H. P., Tomlinson, D., 1995. Geographical differences in the UV measured by intercompared spectroradiometers. *Geophys. Res. Lett.* 22 (14), 1889–1892.
- Seckmeyer, G., Thiel, S., Blumthaler, M., Fabian, P., Gerber, S., Gugg-Helminger, A., Häder, D.-P., Huber, M., Kettner, C., Köhler, U., Köpke, P., Maier, H., Schäfer, J., Suppan, P., Tamm, E., Thomalla, E., 1994. Intercomparison of spectral-UV-radiation measurement systems. *Appl. Opt.* 33 (33), 7805.
- Smith, W. L., 1985. Satellites, chapter 10. *Handbook of applied meteorology*. John Wiley & Sons, New York.

- Stamnes, K., Tsay, S.-C., Wiscombe, W., Jayaweera, K., 1988. Numerically stable algorithm for discrete-ordinate-method radiative transfer in multiple scattering and emitting layered media. *Appl. Opt.* 27 (12), 2502.
- Stöckli, R., 2013. The HelioMont surface radiation processing. Scientific report MeteoSwiss, 93, MeteoSwiss: Federal Office of Meteorology and Climatology (119 pp.).
- Thompson, A., Early, E. A., DeLuisi, J., Disterhoft, P., Wardle, D., Kerr, J., Rives, J., Sun, Y., Lucas, T., Mestechkina, T., Neale, P. J., 1997. The 1994 North American interagency intercomparison of ultraviolet monitoring spectroradiometers. *J. Res. Natl. Inst. Stand. Technol.* 102, 279–322.
- Virtuani, A., Fanni, L., 2014. Seasonal power fluctuations of amorphous silicon thin-film solar modules: Distinguishing between different contributions. *Prog. Photovolt: Res. Appl.* 22 (2), 208–217.
- Wagner, J., Hasel, S., Laube, W., Weihs, P., Rennhofer, M., Berger, K., Leidl, R., Baumgartner, D., 2011. How large is the impact of spectral variability on the energy yield of a-Si, c-Si and CdTe modules? In: *Proc. Thin Film Conference, Munich, Germany*. pp. 153–159.
- Widlowski, J., Pinty, B., Lopatka, M., Atzberger, C., Buzica, D., Chelle, M., M., D., Gastellu-Etchegorry, J., Gerboles, M., Gobron, N., Grau, E., Huang, H., Kallel, A., Kobayashi, H., Lewis, P. E., Qin, W., Schlerf, M., Stuckens, J., Xie, D., 2013. The fourth radiation transfer model intercomparison (RAMI-IV): Proficiency testing of canopy reflectance models with ISO-13528. *J. Geophys. Res. Atmos.* 118, 1-22.
- Yang, S., Ricchiazzi, P., Gautier, C., 1999. Modified correlated k-distribution methods for remote sensing applications. *J. Quant. Spectrosc. Radiat. Transfer* 64, 585-608.

6 Publications

6.1 Publication I

Evaluation of spectral effect on module performance using modelled average wavelength

Giorgio Belluardo, Jochen Ernst Wagner, Anke Tetzlaff, A. and David Moser

*Proceedings of the 28th European Photovoltaic Solar Energy Conference and Exhibition, 3561-3566.
Paris, France, 2013*

EVALUATION OF SPECTRAL EFFECT ON MODULE PERFORMANCE USING MODELED AVERAGE WAVELENGTH

Giorgio Belluardo^{1*}, Jochen Wagner², Anke Tetzlaff², David Moser¹

¹Institute for Renewable Energy, EURAC Research, Viale Druso 1, 39100 Bolzano (BZ), Italy

²Institute for Applied Remote Sensing, EURAC Research, Viale Druso 1, 39100 Bolzano (BZ), Italy

*Phone: +39 0471 055626; Fax: +39 0471 055699; E-mail: giorgio.belluardo@eurac.edu

ABSTRACT: Since solar cells are spectrally selective, photovoltaic modules are affected by the spectral distribution of the in-plane irradiation. This is in turn dependent on the radiative transfer through the atmosphere.

Many parameters are used to characterize the quality of spectral distribution, i.e. its balance towards low rather than high wavelengths. They are based on measured or modeled solar spectra, and may or not require the measurement of the module spectral response.

This paper presents a method for the evaluation of spectral effect through the use of the average wavelength of modeled spectra. It results therefore useful when no measured spectral data is available, and does not require the measurement of the module spectral response.

The integral value of modeled spectral distribution is first validated through comparison with measured irradiance. The average wavelength is then used to assess the spectral effect on the performance of different PV technologies installed at Airport Bolzano Dolomiti (ABD) test facility and monitored by EURAC: polycrystalline silicon (pc-Si), single junction amorphous silicon (a-Si), micromorph silicon (a-Si/ μ c-Si), Cadmium Telluride (CdTe) and Copper Indium Gallium Selenide (CIGS). Daily, seasonal and meteorology-related variability of the parameter is also assessed.

Keywords: spectral effect, average wavelength, modeled spectrum, performance

1 INTRODUCTION

Many parameters are used to characterize the quality of spectral distribution: average photon energy [1, 2], average wavelength, air mass [3], useful fraction [4], spectral mismatch correction [5]. They are based on measured or modeled solar spectra, and may or not require the measurement of the module spectral response.

The purpose of this work is to present the effect of solar spectrum on the performance of different PV technologies using a methodology that does not require availability of ground measurements of spectral irradiance. The spectral distribution is represented by a unique value, the average wavelength, which is calculated from modeled spectra using satellite retrieved cloud information. The integral value of spectral distribution is validated through comparison with measured irradiance. This work also analyses the variability of spectral distribution during the day, with seasons, under different meteorological conditions, and the effect of shading due to adjacent mountains.

2 METHODOLOGY

2.1 Modeling of solar spectrum

Spectrally resolved solar surface irradiance is calculated with the SPECMAGIC algorithm [6]. This algorithm allows for a quick provision of highly accurate data records because it uses lookup tables (LUTs), i.e. pre-computed radiative transfer model (RTM) results which contain the transmittance for a variety of atmospheric and surface states. In this way, RTM does not need to be resolved for every satellite pixel and time, but the transmittance can just be extracted from the LUTs by interpolation. Finally, solar surface irradiance can be calculated from the transmittance by multiplication with the extraterrestrial incoming solar flux density.

The following input parameters are taken into

account:

- aerosol optical depth (from monthly climatologies)
- surface albedo (using land use maps)
- single scattering albedo (fixed value)
- total column ozone (fixed value)
- water vapor column (from monthly climatologies)
- Sun – Earth distance
- solar zenith and azimuth angle

In a first stage the direct and global clear sky spectral irradiance is calculated with the SPECMAGIC algorithm. In order to decrease the computation run-time the correlated-k approach of Kato et al. is used [7], which comes with 32 bands in the whole solar spectrum, each of which is characterized by a unique set of values of gaseous absorption coefficients. The component j of irradiance is derived as follows:

$$I_{j,mod}(\lambda) = I_{j,AM1.5}(\lambda) \frac{I_{j,mod}(k)}{I_{j,AM1.5}(k)}$$

where:

- $I_{j,AM1.5}(\lambda)$: irradiance of the standard spectrum at air mass 1.5
- $I_{j,mod}(k)$: irradiance modeled with SPECMAGIC, with resolution Kato
- $I_{j,AM1.5}(k)$: irradiance of the standard spectrum at air mass 1.5, with resolution Kato

The direct and global actual spectral irradiance is then obtained by attenuating the clear sky spectral irradiance according to the actual clouds using cloud index from MeteoSwiss [8]. The cloud index is converted to the clear sky index and direct and global irradiance are simply calculated as the product of clear sky irradiance and clear sky index. A height correction is also performed taking into account the site altitude and solar

zenith angle.

The modeled direct and global horizontal spectral irradiance are finally modified in order to take into account the shading of the surrounding mountains, and converted to tilted plane by applying a model which assumes an isotropic distribution of diffuse radiation and a fixed value of surface albedo.

2.2 Average wavelength index

The average wavelength of a solar spectrum is the wavelength for which the integral value of irradiance at lower wavelengths equals the integral value of irradiance at higher wavelengths. In other words, at the average wavelength the cumulative spectral irradiance is exactly half of the broadband irradiance.

The spectral range considered in this study is between 307 nm and 1965 nm (corresponding to Kato bands 4 to 27). This is done in order to consider the range of photovoltaic conversion of state of the art solar cells (about 300 nm to 1700 nm). The average wavelength values of the AM1.5 standard spectra in the abovementioned spectral range is 716 nm for direct irradiance and 699 nm for global irradiance.

3 EXPERIMENTAL SETUP

The photovoltaic technologies considered in this study are installed at the Airport Bolzano Dolomiti (ABD) test facility (46.45778 N, 11.32861 E), which has been connected to the medium-voltage grid in August 2010. The plant is composed of a commercial part of 662 kW with CdTe modules, and a 62 kW experimental part with 24 different types of modules, divided into 39 arrays ranging between 1 and 2 kW each, and mounted on fixed racks as well as on single- and dual axis trackers [9]. The technologies considered in this study have a fixed tilt of 30° and an azimuth angle of 8.5° West of South. The site elevation is 262 m above the sea level.

The production data is recorded by commercial inverters with a frequency of 15 minutes. The facility is also equipped with a meteo station for the measurement of horizontal (global and diffuse, secondary standard pyranometers) and global plane-of-array irradiance (secondary standard pyranometer), direct irradiance (secondary standard pyrliometer), and wind speed (2-axis ultrasonic anemometer) with a frequency of 1 minutes. Measured data are then averaged on a 15-minutes time basis.

4 RESULTS AND DISCUSSION

4.1 Validation of modeled data

In a first stage, the integral values of spectral irradiance on both horizontal and tilted (30°) planes are calculated with SPECMAGIC considering the range between 250 and 3000 nm, which is slightly broader than the spectral sensitivity of the secondary standard pyranometers (285-2800 nm). However, this spectral mismatch results in a difference of just 0.04% of irradiance for the standard spectrum 1.5G, mainly concentrated in the long-wave region.

The modeled data is then validated against the corresponding measured values, for year 2011. Figure 1 shows a good agreement, especially for points corresponding to clear sky conditions (ratio of diffuse to

global horizontal irradiance, D_tGHI , lower than 0.20), on the horizontal plane (Fig. 1b). The comparison on tilted plane presents a lower agreement with respect to the horizontal plane, thus indicating a need for a further improvement of the model.

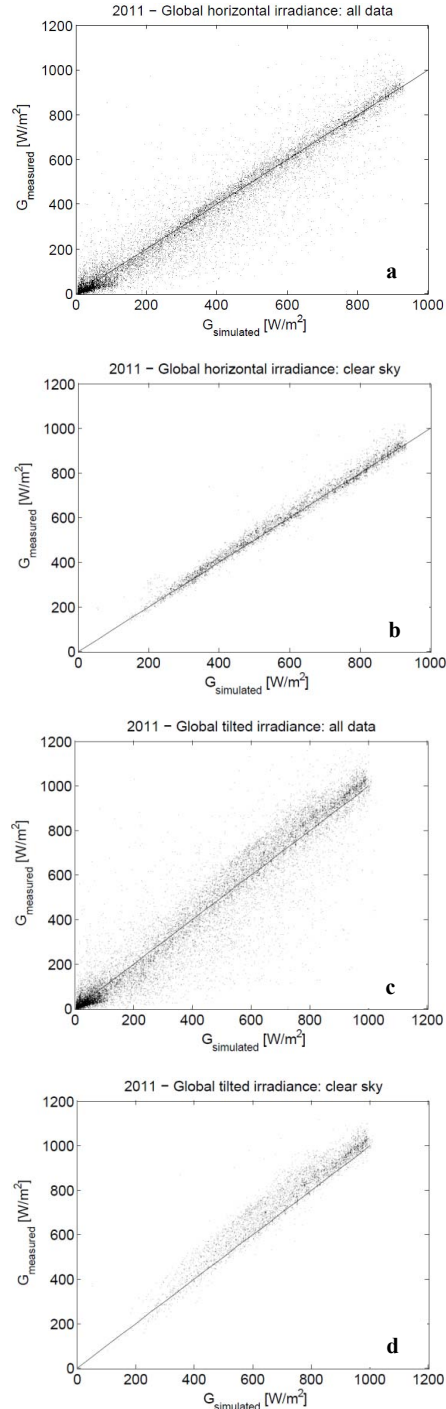


Figure 1: comparison of simulated and measured global irradiance at ABD test installation, year 2011. a) horizontal plane, unfiltered data ($R^2=0.918$) b) horizontal plane, clear sky conditions ($R^2=0.981$) c) tilted plane, unfiltered data ($R^2=0.909$) d) tilted plane, clear sky conditions ($R^2=0.935$)

Furthermore, a comparison between modeled and measured solar spectra data has to be carried out in order to increase the consistency of the model. This will be the object of a future study.

4.2 Site spectral characterization

In order to characterize the ABD site with respect to average wavelength, the variability of this index during the day and the year, and under the shading effect of mountains and cloud cover is analyzed.

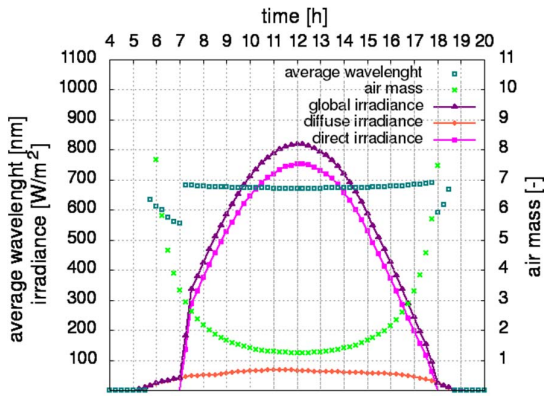


Figure 2: daily variation of average wavelength index over a clear sky day (28th August, 2011, $DtGHI$ 0.11). Direct, diffuse and global irradiance are also shown (left y-axis), as well as air mass (right y-axis). All values refer to the horizontal plane

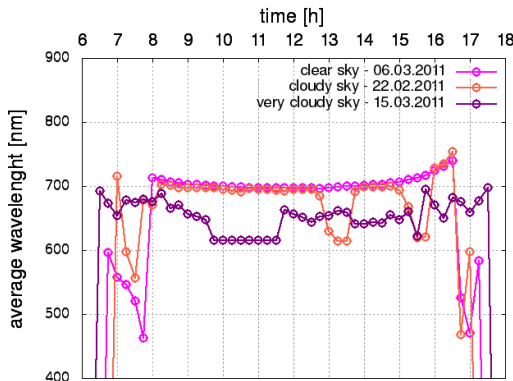


Figure 3: daily variation of average wavelength index due to cloud cover through comparison of a clear sky ($DtGHI$ 0.11), cloudy sky ($DtGHI$ 0.59) and very cloudy sky ($DtGHI$ 0.98) day in 2011. Values refer to tilted plane (30°)

On the horizontal plane, in a clear sky summer day (Figure 2), after sunrise (5:45 AM) the surrounding mountains shade the site and only the diffuse irradiance is visible. The average wavelength is therefore shifted towards wavelengths typical of this component, i.e. towards blue wavelengths, the more the air mass decreases. As soon as the direct irradiance reaches the site (7:15 AM), there is a switch towards red wavelengths, due to the influence of the red-shifted direct component. From this moment on, the index does not vary significantly, even though a minimum point is reached at noon, corresponding to the lowest value of air

mass and angle of incidence (AOI). As for sunrise, at sunset a blue-shift is clearly visible (mountain shading starts at approximately 6:00 PM).

Figure 3 shows the effect of meteorological conditions, basically cloud cover, over the index. Three days corresponding to clear sky conditions ($DtGHI$ close to 0), cloudy sky conditions ($DtGHI$ close to 0.50) and very cloudy sky conditions ($DtGHI$ close to 1) are considered. It is clear that clouds produce instability on the value of average wavelength. The more the sky is covered, the more the direct irradiance component weakens and the index is shifted towards blue wavelengths.

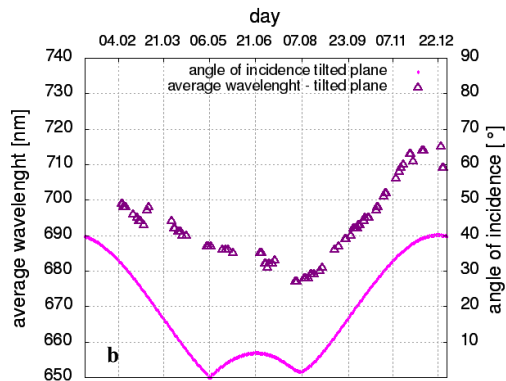
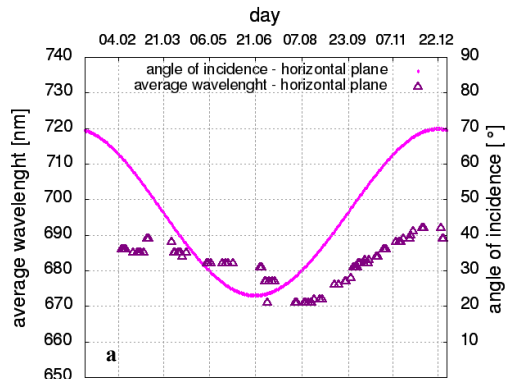


Figure 4: seasonal variation of average wavelength at around noon for year 2011, for a) horizontal and b) tilted (30°) plane, under clear sky conditions ($DtGHI < 0.20$). Corresponding angle of incidence is also displayed. Values for January are missing

The seasonal variation of average wavelength index is shown in Figure 4, both on the horizontal (Fig. 4a) and tilted plane (Fig. 4b). For each day only the value corresponding to the minimum of angle of incidence, that occurs at different times around noon depending on the season, has been considered and filtered for $DtGHI$ less than 0.20 in order to minimize the variability due to cloud cover. Results show that the average wavelength index does not follow the trend of the corresponding angle of incidence for both horizontal and tilted plane, thus indicating that the geometric effect is not the only factor influencing this index. The average wavelength presents an oscillation between a minimum value around August and a maximum value occurring around winter solstice. One would expect a minimum at around summer solstice for the horizontal plane, and a second minimum around

the beginning of May for the tilted plane. Actually, the mismatch between AOI and average wavelength trends seems to be more related to the substantial increase of aerosol and, to a greater extent, of water vapour content during summer in Bolzano [10], following the typical annual cycle in the mid-latitudes [11]. Since the absorption of aerosol and water vapour occurs mainly at the IR region, the spectrum results in a shift towards blue wavelengths, as observed by other authors [1, 12].

4.3 Spectral effects on PV performance

The relation of modeled average wavelength and module performance is evaluated for four different thin-film technologies: single junction amorphous silicon (a-Si), micromorph silicon (a-Si/ μ c-Si), Cadmium Telluride (CdTe) and Copper Indium Gallium Selenide (CIGS). A polycrystalline silicon technology (pc-Si) is also considered as reference.

The data is previously filtered for the following conditions:

- angle of incidence (AOI) less than 50° , in order to avoid angle dependence due to mismatch of cosine behaviour of pyranometer glass dome with respect to flat module plane [2] and minimize incident angle reflection losses
- clear sky conditions (DtGHI < 0.20)
- Performance Ratio range given by $PR_{avg} \pm \sigma$, in order to sort out not homogeneous irradiance conditions that can occur between pyranometer and module due to mountain shading or clouds [13]

As a second step, a temperature correction of array efficiency, η , to 25°C (T_{STC}) is performed in order to minimize temperature effects, using the following expression [14]:

$$\eta_{STC} = \eta \frac{1}{[1 + \gamma_{STC}(T_{cell} - T_{STC})]} \quad (1)$$

that is

$$\eta_{STC} = \eta \frac{1}{[1 + \gamma_{STC}(T_{cell} - 25)]} \quad (2)$$

where γ_{STC} is the temperature coefficient of power (%/ $^\circ\text{C}$) from datasheet. In this work, the module temperature is in turn calculated using the formula described in Skoplaki et al. [15]:

$$T_{cell} = T + (NOCT - T_{NOCT}) \frac{G}{G_{NOCT}} \frac{h_{w,NOCT}}{h_w(v)} \left[1 - \frac{\eta_{STC}}{\tau\alpha} (1 + \gamma_{STC} T_{STC}) \right] \quad (3)$$

T	ambient temperature ($^\circ\text{C}$)
$NOCT$	Nominal Operating Cell Temperature, calculated under the conditions $G=800 \text{ W/m}^2$, $T=20^\circ\text{C}$, $W=1 \text{ m/s}$, given by the manufacturer
T_{NOCT}	temperature under NOCT conditions
G	irradiance (W/m^2)
G_{NOCT}	irradiance under NOCT conditions
$h_w(v)$	wind convection coefficient
$h_{w,NOCT}$	wind convection coefficient at NOCT conditions
η_{STC}	efficiency under STC conditions, given by the manufacturer
τ	transmittance of the cover system
α	absorption coefficient of the cells

T_{STC} temperature under STC conditions

In particular, the wind convection coefficient is a linear function of local wind speed close to the module, v , given by [15]:

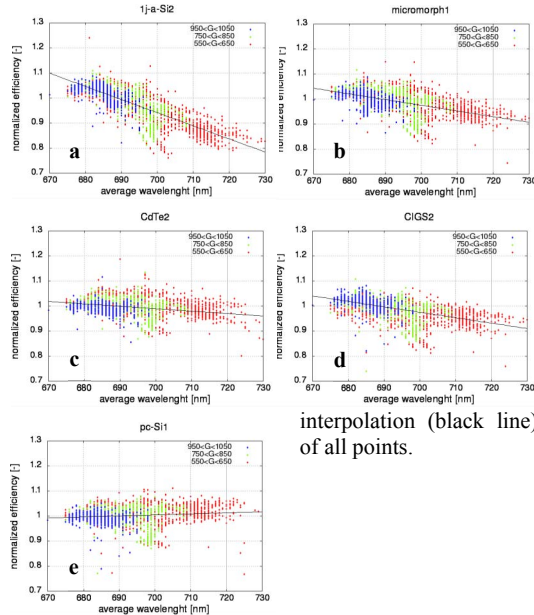
$$h_w(v) = 5.7 + 3.8v$$

while the product $\tau\alpha$ can be assumed as 0.9 [15]. Equation 3 has been demonstrated to better fit the measured values of module temperature at ABD test facility than just considering ambient temperature, because it takes into account the cooling effect of wind on module [16].

Finally, the efficiency is normalized to an efficiency value corresponding to Air Mass 1.5, calculated with a fit on the overall filtered and temperature-corrected points.

In Figure 5 the normalized efficiency is plotted against modeled average wavelength, for the 4 thin-film technologies and the reference polycrystalline. Points are grouped for different in-plane irradiance levels, around 600, 800 and 1000 W/m^2 . A linear fit of all points is also displayed. In Table 1 the percentage of the absolute variation of efficiency in the range between 675 and 725 nm is reported for each technology, together with the Root Mean Square Error (RMSE).

In general, higher irradiance levels correspond to more “blue-shifted” solar spectra, while lower irradiance levels span a broader range. In any case, the slope of cloud points corresponding to different irradiance levels seems to be the same, thus justifying the linear



interpolation (black line) of all points.

Figure 5: normalized efficiency against average wavelength, for clear sky conditions, angle of incidence less than 50° , sorted for shading and corrected to standard temperature of 25°C . Different in-plane irradiance levels ($950 < G < 1050 \text{ W/m}^2$, $750 < G < 850 \text{ W/m}^2$, $550 < G < 650 \text{ W/m}^2$) are displayed, as well as the linear fitting curve (black line). a) a-Si, b) micromorph, c) CdTe, d) CIGS, e) pc-Si.

Table 1 absolute value of efficiency variation in the range 675-725 nm for the considered technologies, and root mean square error of the linear interpolation.

Module name	variation %	RMSE
lj-a-Si1	26.2	0.038
micromorph1	11.3	0.036
CdTe2	4.8	0.031
CIGS2	10.8	0.034
pc-Si1	2.1	0.035

In general, the efficiency of thin-film technologies, corrected for temperature, decreases at increasing wavelength of the solar spectrum. A direct correlation between these results and spectral responsivity (SR) of the considered technologies cannot be done due to the lack of SR measurements. These vary significantly between technologies, as well as between modules of same technology but different manufacturers [2]. Nevertheless, the behavior of thin-film technology seems to be in line with the results reported by different authors [1, 2]. In particular, the variation of efficiency is more evident in amorphous-silicon, where the effects of light-soaking and thermal annealing may play a certain role in addition to spectral effect. However, it has been demonstrated that this effects have a slightly lower influence than spectral effects [4] on module behaviour.

On the other hand, the polycrystalline silicon shows a different performance due to its efficiency that increases at higher wavelengths, as expected considering the typical higher spectral responsivity at near infrared (NIR) wavelengths.

By quantitatively knowing the spectral effects on different technologies is then possible to compare indoor with outdoor data, namely electrical parameters and temperature coefficients.

5 CONCLUSIONS

The average wavelength index calculated from modeled solar spectra with SPEMAGIC algorithm using satellite retrieved cloud information is used to spectrally characterize the Airport Bolzano Dolomiti (ABD) photovoltaic test installation site. Results show that the spectrum is shifted towards red wavelengths in presence of direct component of irradiance, and blue wavelengths in case of prevailing diffuse component due to cloud cover or mountain shading. The spectral content is in general related to air mass and angle of incidence, but also to aerosol and water vapour content of the atmosphere. In particular, their higher concentration during summer months results in a spectral shift towards lower wavelengths, thus giving a minimum level of average wavelength for the year.

The spectral effect of 4 different thin-film technologies and a polycrystalline silicon is also assessed through the relation between efficiency and average wavelength. Thin-films decrease their performance at increasing wavelengths. The efficiency variation in the range 675-725 nm results in 4.8% for CdTe, 10.8% for CIGS, 11.3% for micromorph, 26.2% for a-Si. The latter considerably higher value may be due to the addition of light-soaking and thermal annealing effects. The polycrystalline silicon shows the opposite trend, with increasing performance at increasing wavelengths. The efficiency variation results in 2.1% for this technology.

In general, the integral value of spectral irradiance calculated with SPECMAGIC shows a good agreement with the corresponding irradiance data measured at ABD, especially for the horizontal plane. A comparison between modeled and measured spectra will be also carried out in a future work in order to strengthen the consistency of this model.

6 ACKNOWLEDGMENTS

This work is financed through the project 2-1a-97 "PV Initiative" in cooperation with the autonomous province of Bolzano-Alto Adige (GB, DM), through the Stiftung Suedtiroler Sparkasse (DM), and through the Interreg program IV Italy - Swiss by the European Funds for Regional Development (EFRE) (DM, JW, AT).

7 REFERENCES

- [1] C. Cornaro, A. Andreotti, Influence of average photon energy index on solar irradiance characteristics and outdoor performance of photovoltaic modules, *Progress in Photovoltaics: Research and Applications*, 2012.
- [2] M. Schweiger, M. Ulrich, I. Nixdorf, L. Rimmelspacher, U. Jahn, W. Herrmann, Spectral analysis of various thin-film modules using high precision spectral response data and solar spectral irradiance data, *27th European Solar Energy Conference and Exhibition, Frankfurt, 2012, 3284-3290*.
- [3] A. Virtuani, L. Fanni, Seasonal power fluctuations of amorphous silicon thin-film solar modules: distinguishing between different contributions, *Progress in Photovoltaics: Research and Applications*, 2012.
- [4] R. Gottschalg, D.G. Infield, M.J. Kearney, Experimental study of variations of the solar spectrum of relevance to thin film solar cells, *Solar Energy Materials and solar cells, Volume 79, September 2003, pp. 527-537*.
- [5] B. Marion, Influence of Atmospheric Variations on Photovoltaic Performance and Modeling Their Effects for Days with Clear Skies, *38th IEEE Photovoltaic Specialists Conference, Austin, June 2012*.
- [6] R. Mueller, T. Behrendt, A. Hammer, A. Kemper, A new algorithm for the satellite-based retrieval of solar surface irradiance in spectral bands, *Remote Sensing, Volume 4, September 2012, pp. 622-647*.
- [7] S. Kato, T. Ackerman, J. Mather, E. Clothiaux, The k-distribution method and correlated-k approximation for a short-wave radiative transfer, *Journal of Quantitative Spectroscopy and Radiative Transfer, Volume 62, 1999*.
- [8] Meteoswiss: CM SAF Data and Methods [Online]. Available at http://meteosuisse.ch/web/en/research/current_projects/climate/cmsaf/data_methods.html [Accessed: 26-Feb-2012].

[9] G. Belluardo, M. Pichler, D. Moser, M. Nikolaeva-Dimitrova, One-year comparison of different thin film technologies at Bolzano Airport Test Installation. *Fuelling the Future: Advances in Science and Technologies for Energy Generation, Transmission and Storage*, pp. 229-234.

[10] NASA: Aerosol Robotic Network (AERONET) [Online]. Available at <http://aeronet.gsfc.nasa.gov/> [Accessed: 06-Sept-2013].

[11] J.P. Ortiz de Galisteo, Y. Bennouna, C. Toledano, V. Cachorro, P. Romero, M.I. Andrés, B. Torres, Analysis of the annual cycle of the precipitable water vapour over Spain from 10-year homogenized series of GPS data. *Quarterly Journal of the Royal Meteorological Society*, May 2013.

[12] M. Chegaar, P. Mialhe, Effect of atmospheric parameters on the silicon solar cells performance, *Journal of Electron Devices*, Volume 6, 2008, pp. 173-176.

[13] D. Moser, M. Pichler, M. Nikolaeva-Dimitrova, Filtering procedures for reliable outdoor temperature coefficients in different photovoltaic technologies, *Journal of Solar Energy Engineering*, Volume 136, August 2013.

[14] A. Colli, W.J. Zaaiman, Maximum-Power-Based PV Performance Validation Method: Application to single-Axis tracking and fixed-tilt c-Si systems in the Italian Alpine region, *Progress in Photovoltaics: Research and Applications*, Volume 4, October 2012, pp. 555-563.

[15] E. Skoplaki, A.G. Boudouvis, J.A. Palyvos, A simple correlation for the operating temperature of photovoltaic modules of arbitrary mounting, *Solar Energy Materials & Solar Cells* 92, 2008, pp. 1393-1402.

[16] C. Schwingshackl, M. Petitta, J. E. Wagner, G. Belluardo, D. Moser, M. Castelli, M. Zebisch, A. Tetzlaff, Wind effect on PV module temperature: analysis of different techniques for an accurate estimation, *Energy Procedia*, Vol. 40, 2013, pp. 77-86.

6.2 Publication II

Novel method for the improvement in the evaluation of outdoor performance loss rate in different PV technologies and comparison with two other methods

Giorgio Belluardo, Philip Ingenhoven, Wolfram Sparber, Jochen Ernst Wagner, Philipp Weihs and David Moser

Solar Energy 117, 139-152



Novel method for the improvement in the evaluation of outdoor performance loss rate in different PV technologies and comparison with two other methods

Giorgio Belluardo^{a,c,*}, Philip Ingenhoven^a, Wolfram Sparber^a, Jochen Wagner^b, Philipp Weihs^c, David Moser^a

^a Institute for Renewable Energy, EURAC Research, Viale Druso 1, 39100 Bolzano, Italy

^b Institute for Applied Remote Sensing, EURAC Research, Viale Druso 1, 39100 Bolzano, Italy

^c Institute of Meteorology, University of Natural Resources and Life Sciences, Peter-Jordan-Straße 82, 1190 Vienna, Austria

Received 11 February 2015; received in revised form 21 April 2015; accepted 22 April 2015

Communicated by: Associate Editor Nicola Romeo

Abstract

The interest in the assessment of performance loss rate (*PLR*) of Photovoltaic (PV) modules and arrays has been increasing as long as the global installed power expands and ages. Reliable performance metrics, statistical methods and filtering techniques exploiting continuous outdoor measurements are therefore needed, in order to foster solar bankability of PV systems. This work presents an improved estimation method to decrease the uncertainty associated to *PLR* assessment by (a) using the array generated power metric corrected to Standard Test Conditions (STC), namely $P_{max,STC}$, to minimize seasonal oscillations, (b) applying a filtering technique to eliminate outliers and (c) performing linear interpolation on $P_{max,STC}$ monthly averages series. Estimated *PLR* and its uncertainty are assessed using three-years data from twenty-four grid-connected PV arrays representing nine different PV technologies and results are compared with two other widely-recognized performance metrics, namely: the Array Performance Ratio (PR_a) and the Array Photovoltaic for Utility Systems Applications ($PVUSA_a$). Results show (a) that adding spectral correction to irradiance and temperature correction reduces the uncertainty of 25% on average and (b) that the uncertainty associated to $P_{max,STC}$ metric is reduced to more than 60% on average with respect to the other investigated metrics for crystalline silicon-based technologies, while it is comparable in the case of thin-film technologies. Finally, two procedures estimating the first year *PLR* and the the first five months *PLR* are presented and discussed. © 2015 Elsevier Ltd. All rights reserved.

Keywords: Performance loss rate; Degradation; Initial degradation; Spectral correction

1. Introduction

PV technology has become one of the most important renewable sources in the world. The total installed power

has reached some 139 GW in 2013 on a global level, with an increase of 32% of added capacity in 2013, while over the last five years a 55% average annual capacity growth was reported (REN21 Secretariat, 2014). This trend is favoured by a levelling of module prices coupled with a fall in production costs, while solar cell efficiency increases steadily. At the same time, new technologies and new industrial processes are appearing that assure a higher level of product reliability, which is a key factor when evaluating

* Corresponding author at: Institute for Renewable Energy, EURAC Research, Viale Druso 1, 39100 Bolzano, Italy. Tel.: +39 471 055626; fax: +39 471 055699.

E-mail address: giorgio.belluardo@eurac.edu (G. Belluardo).

possible investments in new plant facilities. For this reason, PV modules producers provide warranties on the performance losses occurring in at least 20 years lifetime. Here uncertainty arises: from the investor's side there is a need for standardized procedures on how to monitor and assess the process of degradation during and at the end of modules lifetime in order to incontrovertibly verify warranty accomplishment; from the manufacturer's side, there is the need to collect as much field data in order to verify the real degradation rate of their products, under different climatic conditions, and tune accelerated ageing tests.

The assessment of degradation is also an essential contribution to the procedure for the estimation of module energy rating, i.e. performance assessment based on the energy output under real operating conditions (Huld et al., 2013; Dirnberger et al., 2015) rather than on the power output measured in laboratory under Standard Test Conditions. For this reason, the energy rating is considered more representative of the module outdoor performance and it will be used in the future as a tool to classify module performance in several standard climatic zones (Huld et al., 2013). The increasing gain of importance within the PV research community is testified by the currently on-going implementation of an *ad hoc* standard (IEC 61853) – already partly published (IEC61853-1:2011, 2011).

The factors and mechanisms behind degradation are well known. PV modules are affected by continuous cycles of temperature, humidity, irradiation, mechanical stress, spotted soiling that can induce corrosion of the metallic connections, delamination, discolouration and breakages of the module, cracks of the cells, hot spots, bubbles and other failures (Ndiaye et al., 2013; Quintana et al., 2002; Köntges et al., 2013; Sharma and Chandel, 2013). In addition to material degradation a PV module or array under outdoor operating conditions is exposed to other factors directly acting on its electric performance. These are diffuse soiling, snow, shading, modules and cell mismatch. For the purposes of this study, it is therefore more appropriate to speak about performance loss rate (*PLR*) rather than degradation rate. The *PLR* of a PV module or system depends on:

- (a) the technology, i.e. the photovoltaic material, the quality of the components and the assembling process;
- (b) the local climatic conditions;
- (c) the experimental and analysis methodology used for its assessment.

Several studies have been conducted on this topic. Jordan and Kurtz (2013) collected nearly 2000 *PLRs* from studies from the last 40 years, calculating an average $-0.7\%/year$ and median $-0.5\%/year$ performance loss rate for crystalline silicon technologies, and an average $-1.5\%/year$ and median $-1\%/year$ for thin-film technologies. In general, *PLRs* for crystalline silicon technologies

resulted more concentrated around the median, while thin-film technologies showed more dispersed values, with a minimum of $-4.2\%/year$. Another study on the same database (Jordan et al., 2012) found short-circuit current (I_{sc}) and, in lesser extent, fill factor (FF) as the largest contributor to power degradation in crystalline silicon technologies, especially in hot and humid climates. As for thin-film technologies, FF was reported to play a major role particularly for humid climates. Skoczek et al. (2009) analysed the long-term performance of 204 crystalline silicon-based modules installed in the 1980s representing 53 module types from 20 producers. The continuous exposure time ranged between 19 and 23 years. Results showed an average $-0.8\%/year$ *PLR*, with 82.4% of modules respecting the typical manufacturers' warranty of 90% of the initial power after 10 years and 80% after 25 years.

In general, the assessment of *PLR* can exploit measurements performed indoor (Sharma and Chandel, 2013; Carr and Pryor, 2004; Polverini et al., 2013) and outdoor (Kahoul et al., 2014; Munoz et al., 2011; Ndiaye et al., 2014; Makrides et al., 2014; Kamei et al., 2014). As for the latter, the electrical parameters can be recorded in dedicated test sites mainly built for research purposes and equipped with *I/V* curve tracers that acquire data with a frequency not lower than 10 min (Kahoul et al., 2014; Munoz et al., 2011; Ndiaye et al., 2014). Another category of outdoor measurements involves the use of electrical records from systems continuously kept at Maximum Power Point (MPP), performed using also commercial inverters (Makrides et al., 2014; Kamei et al., 2014). This last kind of studies is particularly interesting to plant owners and installers, since it can be performed on any kind of PV plant connected to the grid, just provided that a reliable irradiance measurement is available.

In general, the calculation of *PLR* from field measurements involves the adoption of a performance metric and of a statistical method. The first consists in an analysis technique to calculate representative performance estimators on a selected time scale (usually monthly). Amongst these, the Array Performance Ratio (PR_a) and Array PVUSA ($PVUSA_a$) indexes are the most commonly used (Jordan and Kurtz, 2013). The statistical methods are mathematical algorithms applied on the time series of performance estimators in order to extract a trend. The most common is linear regression but also classical series decomposition (CSD) (Kendall, 1976), locally weighted scatterplot smoothing (LOESS) (Chambers et al., 1983) and autoregressive integrated moving average (ARIMA) (Bartholomew et al., 1971) are used.

The calculation of *PLR* is more accurate, the more the applied performance metrics, statistical methods and filtering techniques succeed in minimizing seasonal oscillation and eliminate outliers (Makrides et al., 2014; Phinikarides et al., 2014). The scope of this paper is therefore to apply an improved method based on the use of the array generated power metric (P_{max}) corrected for irradiance, temperature and spectral effects to Standard Test Conditions

(STC) associated to suitable filtering technique and linear regression, with the aim of decreasing the overall uncertainty in the estimation of PLR . For simplification, this method is named after its metric, $P_{max,STC}$, and is compared to other methods based on the two widely-recognized metrics PR_a and $PVUSA_a$, to which the same filtering technique and linear regression are applied. The comparison is performed on the base of PLR and of the associated uncertainty. The study is performed on nine different PV technologies, and considers the period between the 6th and the 41st operation month. Finally, a methodology to extrapolate spectral and broadband irradiance is also presented, coupled with an estimation of the first year and initial (first five months of modules operation) performance loss.

2. Experimental setup

The investigated PV technologies are part of the outdoor test facility of Airport Bolzano Dolomiti (ABD) (position ca. 46.46N, 11.33E, elevation: 262 m) located in South Tyrol, Italy (Belluardo et al., 2012). Twenty-four different module types (technology, manufacturer and design) are installed at a fixed tilt of 30° and an orientation of 8.5° West of South. For the main characteristics of the modules see Table 1. The DC-side electrical parameters of each array are measured every 15 min by commercial inverters that assure a good level of accuracy in current (I_{mpp}) and voltage (V_{mpp}), with an average difference from a dedicated system of less than 5% and less than 2%, respectively, further decreasing at higher irradiance (Fanni et al., 2014). An independent meteo station provides data of horizontal global and diffuse irradiance, global plane-of-the-array (POA) irradiance, wind speed and ambient temperature with a frequency of 1 min, which is then averaged on a 15-min time interval. The sensors are systematically cleaned and periodically calibrated in order to comply with the standard IEC61724:1998 (1998). Electrical data have been recorded since August 2010, while weather data are available from February 2011.

3. Improved methodology

3.1. P_{max} metric corrected to STC

The proposed improved method is based on the estimation of monthly averages of array generated power P_{max} corrected to STC conditions, $P_{max,STC}$: irradiance of 1000 W/m², cell temperature of 25 °C and Air Mass 1.5. Data for angle of incidence (AOI) higher than 50° are filtered out, in order to minimize incident angle reflection losses (Schweiger et al., 2012; King et al., 2004).

First, P_{max} corrected for irradiance and temperature, $P_{T,G,corr}$, is computed using the following expression:

$$P_{T,G,corr} = P_{max} \frac{G_{STC}}{G} \frac{1}{[1 + \gamma \cdot (T_{cell} - T_{STC})]} \quad (1)$$

Table 1

Main characteristics of investigated PV arrays. Nominal Power per module ($P_{n,mod}$) and total array ($P_{n,tot}$), temperature coefficient (T_{coef}) and Nominal Operating Cell Temperature ($NOCT$) from datasheet. mc-Si: mono-crystalline silicon; pc-Si: poly-crystalline silicon; ribbon: poly-crystalline silicon with ribbon technology; micro: micromorph silicon; CIGS: Copper Indium Gallium Selenide; CdTe: Cadmium Telluride; 1/2/3j-a-Si: single/double/triple junction amorphous silicon.

Tech	N_{mod} –	$P_{n,mod}$ W	$P_{n,tot}$ kW	T_{coef} %/K	$NOCT$ °C
mc-Si1	14	140	1.96	−0.50	45.0
mc-Si2	16	124	1.98	−0.50	45.0
mc-Si3	8	220	1.76	−0.50	45.0
mc-Si4	4	300	1.20	−0.38	45.0
mc-Si5	4	300	1.20	−0.38	45.0
pc-Si1	18	222	4.00	−0.43	45.0
pc-Si2	18	230	4.14	−0.45	45.0
pc-Si3	24	175	4.20	−0.44	46.9
pc-Si7	11	225	2.48	−0.50	47.9
pc-Si8	9	225	2.03	−0.45	47.0
pc-Si9	9	230	2.07	−0.45	47.0
ribbon1	20	205	4.10	−0.45	44.8
micro1	10	110	1.10	−0.25	48.4
micro2	10	115	1.15	−0.25	46.0
micro3	8	135	1.08	−0.24	48.0
CIGS2	20	55	1.10	−0.25	46.0
CIGS3	14	80	1.12	−0.36	47.0
CIGS4	14	80	1.12	−0.36	47.0
CdTe2	90	77.5	6.98	−0.25	45.0
1j-a-Si1	20	50	1.00	−0.19	46.0
1j-a-Si2	12	100	1.20	−0.20	49.0
2j-a-Si1	36	27	0.97	−0.20	46.0
3j-a-Si1	3.5	272	0.95	−0.21	46.0
3j-a-Si2	3.5	272	0.95	−0.21	46.0

where γ is the temperature coefficient in power (%/°C) from datasheet, P_{max} and G are the 15-min based measured array generated power and POA irradiance, and G_{STC} and T_{STC} are the irradiance and module temperature at STC conditions. Cell temperature, T_{cell} , is in turn calculated with the following formula (Skoplaki and Palyvos, 2009):

$$T_{cell} = T + (NOCT - T_{NOCT}) \frac{G}{G_{NOCT}}, \quad (2)$$

where T is the ambient temperature and $NOCT$ is the Nominal Operating Cell Temperature from datasheet, determined under the conditions $T_{NOCT} = 20$ °C, $G_{NOCT} = 800$ W/m², $W = 1$ m/s. The modeling of T_{cell} data was motivated by the incomplete set of back-of-module temperature measurements available during the investigated period at ABD test site.

3.1.1. Spectral correction

To correct P_{max} also to spectral conditions corresponding to AM1.5 (G03 Committee, 2012) an index is needed that quantifies the shape of the solar spectrum, i.e. its shift towards lower or higher wavelengths. In this work, the average wavelength index λ_{ave} was used, and computed from

simulated spectra. The average wavelength of a solar spectrum is defined as the wavelength for which the integral value of irradiance at lower wavelengths equals the integral value of irradiance at higher wavelengths (Wagner et al., 2011):

$$\int_{\lambda_{min}}^{\lambda_{ave}} G_{solar}(\lambda) d\lambda = \int_{\lambda_{ave}}^{\lambda_{max}} G_{solar}(\lambda) d\lambda, \quad (3)$$

where G_{solar} is the global solar spectral irradiance while λ_{min} and λ_{max} are the wavelength range limits of the solar spectrum.

A linear relation between $P_{T,G_{corr}}$ and the average wavelength was found, as shown in Fig. 1 (top) for one technology:

$$P_{G,T_{corr}}(\lambda_{ave}) = c \cdot \lambda_{ave} + d \quad (4)$$

At STC conditions the previous is:

$$P_{max,STC} = P_{G,T_{corr}}(\lambda_{ave}^{AM1.5}) = c \cdot \lambda_{ave}^{AM1.5} + d \quad (5)$$

Combining (4) and (5) $P_{max,STC}$ is found as:

$$P_{max,STC} = P_{G,T_{corr}}(\lambda_{ave}) - c \cdot (\lambda_{ave} - \lambda_{ave}^{AM1.5}) \quad (6)$$

Therefore, the estimation of $P_{max,STC}$ requires the estimation of the regression parameter c from Eq. (4) and the average wavelength at AM 1.5, $\lambda_{ave}^{AM1.5}$. The latter can be estimated using a phenomenological logarithmic interpolation of the relation between average wavelength and Air Mass, as shown in Fig. 1 (bottom):

$$\lambda_{ave} = e + f \cdot \log(g \cdot AM + h), \quad (7)$$

where $e, f, g,$ and h are the regression parameters that are used to determine $\lambda_{ave}^{AM1.5}$.

3.1.2. Spectral simulation

Since measurements of solar spectrum are not available at the ABD test facility, spectral information was retrieved with simulation using the fast SPECMAGIC algorithm (Mueller et al., 2012). The considered wavelength range

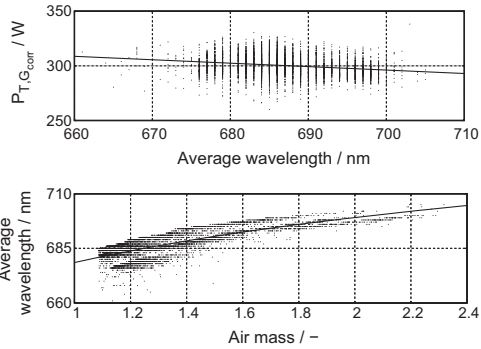


Fig. 1. (top) Relation between average wavelength and P_{max} corrected to irradiance and temperature according to Eq. (1) and (bottom) correlation of average wavelength and Air Mass, for mc-Si5. Values correspond to POA irradiance higher than 800 W/m^2 and $\overline{PR}_a - \sigma < PR_a < \overline{PR}_a + \sigma$.

was between 307 nm and 1965 nm, in order to be sure to include the range of spectral responsivity of state-of-the-art solar cells (about 300–1700 nm). The following input parameters were used:

- Aerosol optical depth (from monthly climatologies).
- Surface albedo (using land use maps).
- Single scattering albedo (fixed value).
- Total column ozone (fixed value).
- Water vapor column (from monthly climatologies).
- Sun–Earth distance.
- Solar zenith and azimuth angle.

First, the direct and global horizontal clear sky spectral irradiance were calculated using the SPECMAGIC algorithm coupled with the correlated-k approach of Kato et al. (1999), in order to further decrease the computation run-time. These spectra were then corrected in order to account for real-sky conditions and shading from the surrounding mountains using the cloud index from MeteoSwiss (Meteoswiss, 2012) and a Digital Elevation Model (DEM), respectively. Finally, conversion to POA was achieved by applying a transposition model assuming an isotropic distribution of diffuse radiation (Duffie and Beckman, 2006).

The simulated values of global horizontal and POA irradiance were validated against the corresponding measured values using the method described in Castelli et al. (2014) for the period 2011–2013, see Fig. 2. The statistical parameters used to evaluate the quality of the simulations were the mean bias deviation (MBD), the mean absolute deviation (MAD), and the root mean square error (RMSE) which are defined as

$$MBD = \frac{1}{n} \sum_{i=1}^n (G_{sim} - G_{meas}), \quad (8)$$

$$MAD = \frac{1}{n} \sum_{i=1}^n |G_{sim} - G_{meas}|, \quad (9)$$

$$RMSE = \sqrt{\frac{1}{n} \sum_{i=1}^n (G_{sim} - G_{meas})^2}. \quad (10)$$

The statistical parameters found for the simulation are given in Table 2.

3.2. Preliminary filtering

Prior to any computation, a first filter validating only values of 15-min based POA irradiance higher than 800 W/m^2 is applied. This in order to decrease the uncertainty deriving from the use of temperature coefficient from datasheet, which is retrieved at POA irradiance of 1000 W/m^2 .

A second filter considers only points whose 15-min based Array Performance Ratio (PR_a), defined later in Section 4.1, is within the range $\overline{PR}_a \pm \sigma$, where \overline{PR}_a is the average PR_a of a specific month and technology, and σ is

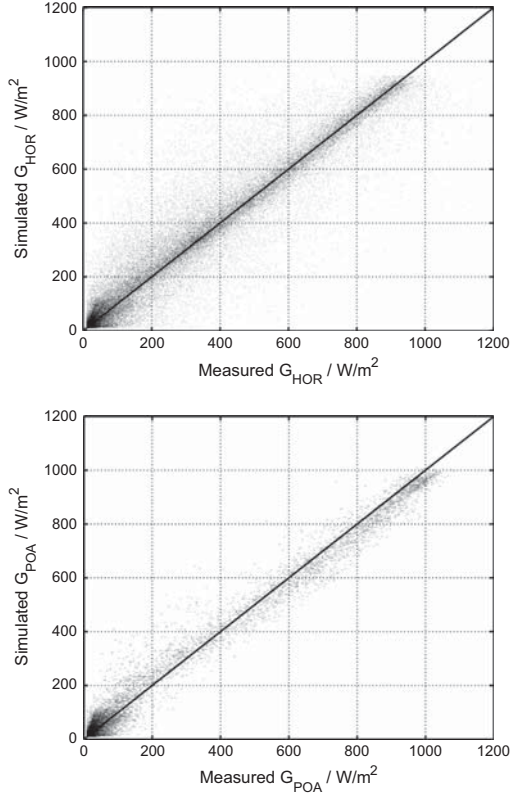


Fig. 2. Scatter plot of measured vs simulated irradiance values for the period 2011–2013. (top) Global horizontal and (bottom) global POA irradiance.

Table 2
Statistical parameters associated to the simulated values of horizontal and POA irradiance, referring to the period 2011–2013.

	G_{HOR} (W/m ²)	G_{POA} (W/m ²)
MBD:	-11.3	-12.0
MAD:	50.4	68.4
RMSE:	81.2	108.4

the associated standard deviation. In this way, around 68% of data points is validated, thus eliminating values corresponding to inhomogeneous irradiance conditions on the irradiance sensor and the PV module (Moser et al., 2013), e.g. for not-uniform cloud cover or shading due to close obstacles.

3.3. Estimation of PLR

A linear least square fit is applied to the series of monthly averages of $P_{max,STC}$, $\bar{P}_{max,STC}$. The fitted trend line is given by:

$$\hat{P}_{max,STC}(t) = a \cdot t + b \quad (11)$$

where $\hat{P}_{max,STC}$ is the modeled average of $P_{max,STC}$ at month number t . The regression parameters a and b represent, respectively, the estimated monthly absolute loss (if negative) or gain (if positive) of $P_{max,STC}$, and the initial estimated value of $P_{max,STC}$. Therefore, the quantity:

$$PL = 12 \cdot a, \quad (12)$$

represents the absolute estimated performance gain or loss in one-year time, and the quantity:

$$PLR = \frac{12 \cdot a}{b} \quad (13)$$

the estimated performance loss (or gain) rate PLR .

The uncertainty associated to estimated PLR as defined by Eq. (13) is computed according to the procedure proposed by the Guide to the Expression of uncertainty measurement (GUM - JCGM 100:2008, 2008), and is given by:

$$u_{PLR} = \sqrt{\left(\frac{\partial PLR}{\partial a}\right)^2 \cdot u_a^2 + \left(\frac{\partial PLR}{\partial b}\right)^2 \cdot u_b^2} \quad (14)$$

where

$$\frac{\partial PLR}{\partial a} = \frac{12}{b} \quad (15)$$

$$\frac{\partial PLR}{\partial b} = -\frac{12 \cdot a}{b^2} \quad (16)$$

and u_{PLR} , u_a and u_b are the standard deviations associated to PLR , a and b , respectively. The error between the estimated linear model $\hat{P}_{max,STC}$ and $\bar{P}_{max,STC}$ is computed as:

$$\epsilon_i = \bar{P}_{max,STC_i} - \hat{P}_{max,STC_i} \quad (17)$$

where i is the generic i th month for which $\bar{P}_{max,STC}$ is available (and therefore referred also to as available month), and should not be confused with t . Since ϵ_i has been verified to be normally distributed, the following expressions are valid (Montgomery et al., 2012):

$$u_a^2 = \sigma_a^2 = \frac{\sum_{i=1}^N (\epsilon_i)^2}{N-2} \cdot \frac{1}{\sum_{i=1}^N (t_i - \bar{t})^2} \quad (18)$$

$$u_b^2 = \sigma_b^2 = \frac{\sum_{i=1}^N (\epsilon_i)^2}{N-2} \cdot \left(\frac{1}{N} + \frac{\bar{t}^2}{\sum_{i=1}^N (t_i - \bar{t})^2} \right) \quad (19)$$

where N is the total number of available months and:

$$\bar{t} = \frac{\sum_{i=1}^N t_i}{N} \quad (20)$$

is the average t . Eq. (14) does not contain any covariance term since it is reasonable to assume that a and b are independent variables.

3.4. Optimization of P_{max} metric

The filtering and correction techniques described in the previous sections are, among different analysed combinations, those minimizing the uncertainty of estimated PLR

defined by Eq. (14). More specifically, the following combinations were tested:

1. $\overline{PR}_a \pm \sigma$ and $G > 800 \text{ W/m}^2$ filter, no correction (no use of Eqs. (1) and (6)).
2. $\overline{PR}_a \pm \sigma$ and $G > 800 \text{ W/m}^2$ filter, G and T correction (only Eqs. (1) and (6)).
3. $\overline{PR}_a \pm \sigma$ and $G > 50 \text{ W/m}^2$ filter, G , T and spectral correction (Eqs. (1) and (6)).
4. $\overline{PR}_a \pm \sigma$ and $G > 800 \text{ W/m}^2$ filter, G , T and spectral correction (Eqs. (1) and (6)).

The resulting uncertainties associated to estimated PLR , calculated using Eq. (14) are displayed in Fig. 3. Option 4 shows the lowest uncertainty for all investigated technologies with the only exception of ribbon, and was therefore selected as combination of filtering and correction techniques to be applied within the proposed improved $P_{max,STC}$ method.

It is interesting to compare results from Option 4 and Option 2, which applies the same conditions of Option 4 but does not include spectral correction. In Fig. 4 the relative difference in estimated PLR uncertainty between these two options is shown. In general, option 4 assures 25% on average less uncertainty than option 2, with a peak of 42%. In general, it is possible to affirm that a correction for at least irradiance and temperature coupled with a filtering for irradiance levels above 800 W/m^2 should be included when assessing PV performance loss outdoor using $P_{max,STC}$ metric. A further correction for spectral effects would considerably improve the accuracy of this metric, thus making the inclusion of solar spectral information, e.g. by installing a spectroradiometer, advisable. On the other hand, although the cost of this type of sensor is decreasing, the installation in PV systems for non-scientific applications is still inconvenient. A valuable alternative is the simulation of solar spectra, as performed in this study and presented in Section 3.1.2.

Option 3 applies a less stringent filter on irradiance levels thus validating a more consistent number of data points. This way $P_{max,STC}$ values result available also for winter

months, which is not the case when applying a filter on $G > 800 \text{ W/m}^2$ (see Section 5), at the latitude of Bolzano. This option produces higher values of estimated PLR uncertainty than options 2 and 4, but results more reliable than methods not performing any kind of correction. This implies that the reduction of seasonal oscillation of monthly values of $P_{max,STC}$ metric, and supposedly of other performance metrics, plays a bigger role than their temporal continuity.

4. Other metrics

4.1. Array Performance Ratio method

The Performance Ratio is a number between 0 and 1 (under STC conditions) indicating the overall effect of losses on the array's rated output due to array temperature, incomplete utilisation of the irradiation, and system component inefficiencies or failures (IEC61724:1998, 1998; Woyte et al., 2014) over a given time period:

$$PR = \frac{Y_f}{Y_r}, \quad (21)$$

where Y_f is the final yield, i.e. the generated AC-energy per kW of installed PV array, and Y_r is the reference yield, i.e. the ratio of POA irradiance and irradiance at STC conditions. Though not mentioned in IEC 61724 standard (IEC61724:1998, 1998), the PR based on the array yield Y_a , i.e. the generated DC-energy per kW of installed PV array, is also commonly used:

$$PR_a = \frac{Y_a}{Y_r}, \quad (22)$$

and is named as Array Performance Ratio. This way only losses attributable to the PV array are accounted for, while losses attributable to BOS inefficiencies (e.g. inverter losses) are excluded. The advantage of PR_a method is the normalization to the irradiance. However, the strong temperature dependence reflects on the strong seasonality of the PR_a metric.

In this work the PR_a metric is calculated according to Eq. (22) on a monthly base, by summing up all the

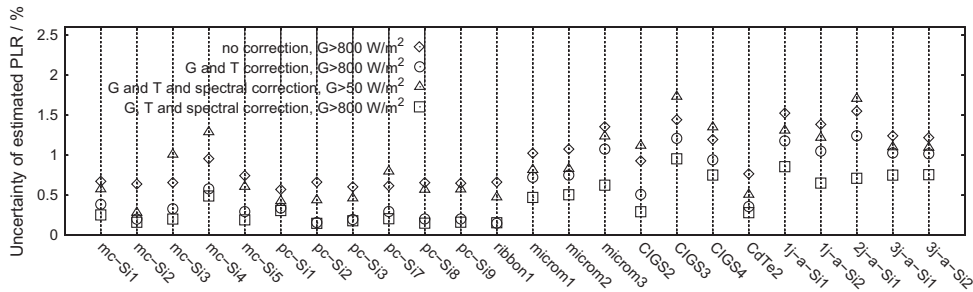


Fig. 3. Uncertainty of estimated PLR as defined by Eq. (14) resulting from applying $P_{max,STC}$ metric with different filtering and correction techniques and linear interpolation of monthly averages.

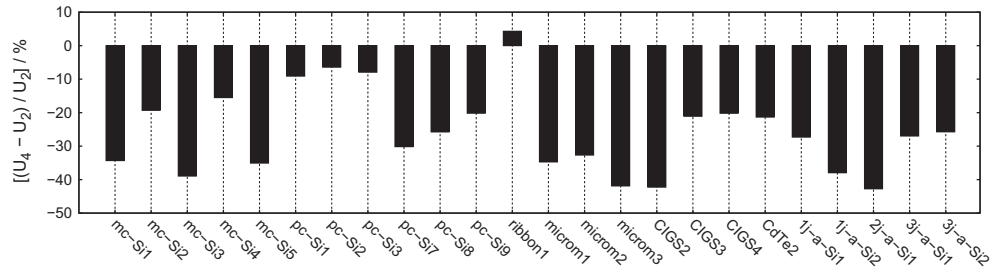


Fig. 4. Relative difference of estimated PLR uncertainty resulting from applying $P_{max,STC}$ metric according to Option 2 and Option 4 filtering and correction techniques, and linear interpolation of monthly averages.

15-min based contributes of Y_a and Y_r , validated by filters discussed in Section 3.2. The estimated PLR and its associated uncertainty are then computed following the procedure described in Section 3.3, where one has to substitute PR_a to $P_{max,STC}$ in Eq. (11) and in Eq. (17).

4.2. Array PVUSA method

Photovoltaics for Utility Scale Applications (PVUSA) was developed by NREL in the 1990s (Whitaker et al., 1997) as a methodology to evaluate the performance of PV systems under Performance Test Conditions (PTC). The method consists in finding the best-fit correlation between measured system generated power P and measured POA irradiance, G , wind speed, W , and ambient temperature, T according to the following parametrized equation:

$$P = G(a + b \cdot G + c \cdot W + d \cdot T) \quad (23)$$

The parameters a , b , c , and d are then used to estimate the power at PTC conditions ($G = 1000 \text{ W/m}^2$, $T = 20 \text{ }^\circ\text{C}$, $W = 1 \text{ m/s}$).

In this work the PVUSA metric is calculated on a monthly base, and regression parameters are retrieved by fitting the cloud of 15-min based combinations of measured DC-side P_{max} , G , W , and T . For this reason we refer to Array PVUSA, $PVUSA_a$. The estimated PLR and its associated uncertainty are then computed following the procedure described in Section 3.3, where one has to substitute $PVUSA_a$ to $P_{max,STC}$ in Eq. (11) and in Eq. (17). This method involves a higher number of variables than PR_a method, but is expected to be less influenced by the climatic parameters because of the regression performed.

5. Medium-term performance loss

In this section, the results of PLR estimated with the three selected methods are presented. Calculations were performed exploiting experimental data covering a three-years time span, corresponding to the 6th up to the 41st operation month (from January 2011 to December

2013). For this reason, we refer to estimated medium-term PLR . Figs. 5 and 6 show the monthly series of the three performance metrics calculated as described in Sections 3, 4.1 and 4.2, for each investigated technology. The interpolation line is also displayed to qualitatively indicate the trend of performance loss or gain. In order to compare PR_a results with $P_{max,STC}$ and $PVUSA_a$, the latter were normalized by the nominal power P_n .

In general, a constant rate of performance loss or gain is evident, with the exception of CIGS3 and CIGS4, for which the initial faster degradation might not have finished at 6th operation month, yet. Actually these two PV arrays, with modules from the same manufacturer, showed an unusual degradation through the years, with a 20–30% loss with respect to initial rated power and the disagreement with the producer claimed warranties after already four years of operation.

The unusual trend of 2j-a-Si1 is actually due to the disconnection of the junction box of one module, which occurred between October 2012 and July 2013 thus causing the partial electrical disconnection of the modules of the PV group. These months have therefore not been taken into consideration when estimating PLR for this technology.

Triple junction amorphous silicon groups (3j-a-Si1 and 3j-a-Si2) show an overall performance gain instead of loss. A possible explanation might be that these modules consist of film laminated with a flexible polymer glued on an aluminum-zinc plate steel sheeting, which is in turn superimposed onto a corrugated metal sheet. This mounting system, which does not allow an effective module cooling by ventilation, is unique in the ABD test field, since all other groups are mounted on metal extruded bars. As a consequence, the 3j-a-Si modules have higher operating temperatures. As demonstrated by Pola et al. (2007) in a study comparing 3j-a-Si modules of same type mounted on a thermally isolated and on a ventilated structure, the thermal annealing generated by high temperatures can be as much as significant to reverse the main degradation mechanism. In particular, the annealing mechanism is activated at $50 \text{ }^\circ\text{C}$, and is more effective when close to $80 \text{ }^\circ\text{C}$.

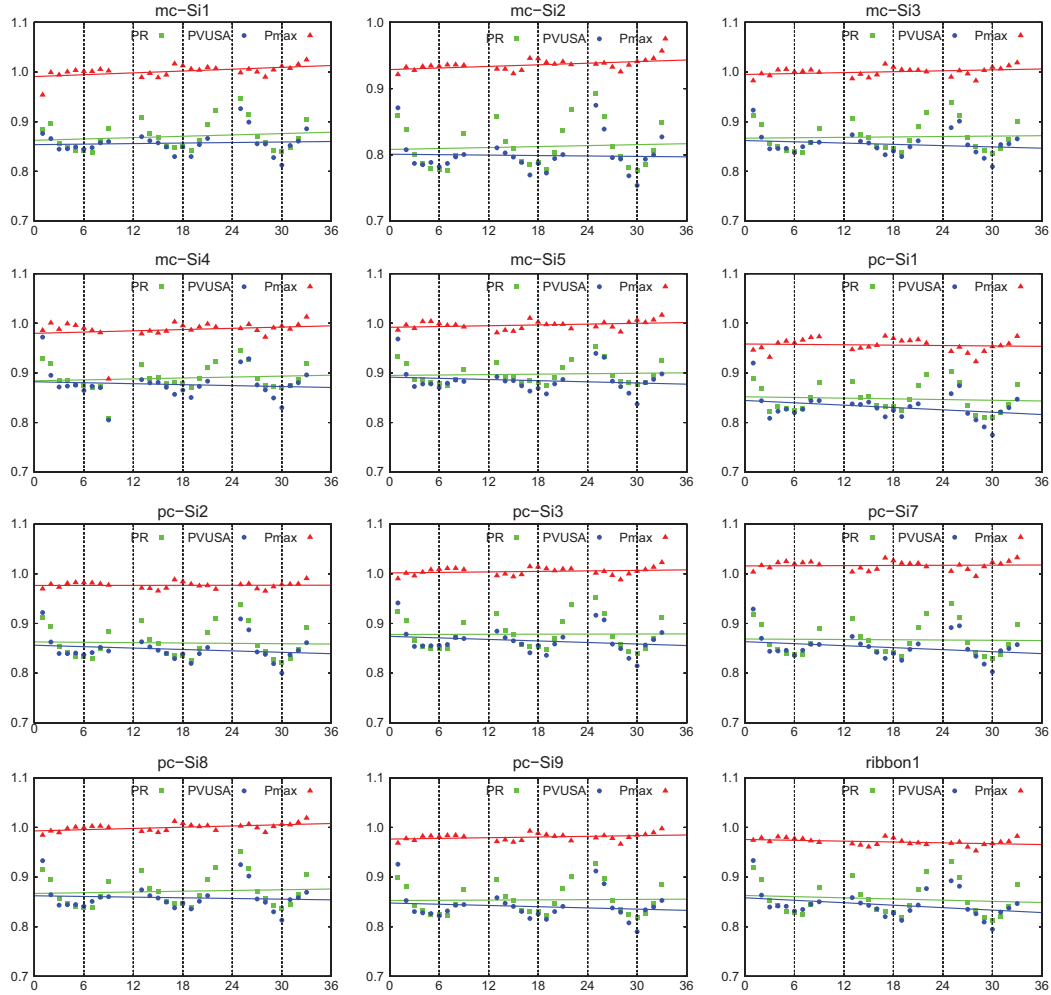


Fig. 5. Monthly values of performance metrics $P_{max,STC}$, PR_a and $PVUSA_a$, for crystalline silicon technologies (0 = January 2011; 12 = January 2012; 24 = January 2013; 36 = January 2014). Linear regression is also displayed, whose parameters a and b are used to estimate PLR according to Eq. (13) and its uncertainty according to Eq. (14). $P_{max,STC}$ and $PVUSA_a$ metrics are normalised by nominal power P_n in order to be comparable.

Thermal annealing occurs also for the other amorphous silicon-based technologies, as it is shown in Fig. 6: higher performance metrics occur in summer, from June to September, lower in winter. This is visible also when using the $P_{max,STC}$ metric, since this method does not account for thermal annealing effects. It was found that during the period 2011–2013 the average monthly ambient temperature increased of $0.3\text{ }^\circ\text{C}/\text{year}$ under irradiance levels higher than $800\text{ W}/\text{m}^2$. This increase in ambient temperature might have boosted the operating temperatures and consequently the thermal annealing effects in the triple junction to such an extent that the performance improvement due to it

has overcome the loss of performance. In order to validate this hypothesis it should be verified if the higher temperatures reached indeed the level where the main degradation mechanism can be reversed.

As discussed in Section 1, a good evaluation method that ensures the calculation of PLR with a low level of uncertainty should minimize the seasonal oscillation of the performance metric series. Figs. 5 and 6 show that this is in general fulfilled by the $P_{max,STC}$ method, less by PR_a and $PVUSA_a$ methods, as also confirmed by the values of uncertainty displayed in Table 3. More specifically, for the crystalline silicon technology the $P_{max,STC}$ method reduces

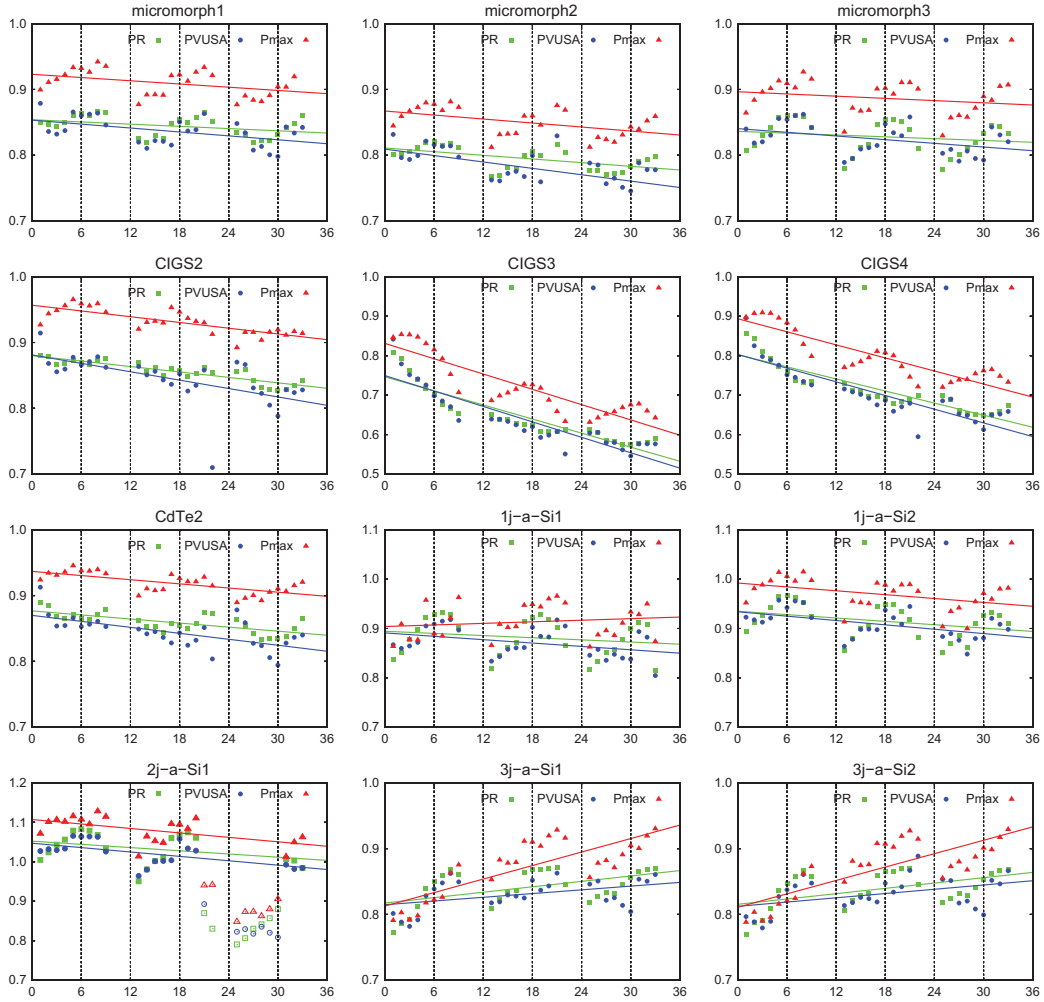


Fig. 6. Monthly values of performance metrics $P_{max,STC}$, PR_a and $PVUSA_a$, for thin-film technologies (0 = January 2011; 12 = January 2012; 24 = January 2013; 36 = January 2014). Linear regression is also displayed, whose parameters a and b are used to estimate PLR according to Eq. (13) and its uncertainty according to Eq. (14). $P_{max,STC}$ and $PVUSA_a$ metrics are normalized by nominal power P_n in order to be comparable.

estimated PLR uncertainty from 18% up to 84% of the uncertainty associated to the other investigated methods, with an average reduction of 66% and 62% with respect to PR_a and $PVUSA_a$ methods, respectively. The same method produces uncertainty levels comparable to the most reliable method amongst PR_a and $PVUSA_a$ (PR_a for micromorph, CIGS, CdTe, and $PVUSA_a$ for single and double junction amorphous silicon) in the case of thin-film technology.

Focusing the analysis on the values of estimated PLR , Table 3 also shows that results computed with $P_{max,STC}$ method are very similar to those obtained with PR_a method, with the exception of amorphous silicon-based technologies. In general it is possible to affirm that:

- PR_a and $P_{max,STC}$ methods are associated to less negative (lower performance loss), and more positive (more performance gain) values of estimated PLR than $PVUSA_a$ method.
- For crystalline silicon-based technologies (mc-Si, pc-Si and ribbon), PR_a and $P_{max,STC}$ methods produce positive values of estimated PLR (performance gain) for most of the considered groups, while $PVUSA_a$ always gives negative values (performance loss). Taking error bars into account, it is possible to estimate a performance loss rate almost null for this technology, and in any case higher than $-0.7\%/year$, calculated as average value on the three investigated methods.

Table 3
Values of estimated PLR (R) and associated uncertainty (u) calculated with different evaluation methods.

Tech	PR_a		$PVUSA_a$		$P_{max,STC}$	
	R %/y	u %	R %/y	u %	R %/y	u %
mc-Si1	0.6	±0.8	0.2	±0.6	0.8	±0.3
mc-Si2	0.4	±1.0	-0.2	±0.8	0.5	±0.2
mc-Si3	0.2	±0.8	-0.6	±0.6	0.4	±0.2
mc-Si4	0.4	±0.7	-0.4	±0.8	0.5	±0.5
mc-Si5	0.2	±0.6	-0.5	±0.7	0.3	±0.2
avg.	0.4	±0.8	-0.3	±0.7	0.5	±0.3
pc-Si1	-0.3	±0.8	-1.1	±0.7	-0.2	±0.3
pc-Si2	-0.2	±0.9	-0.7	±0.7	0.0	±0.1
pc-Si3	0.0	±0.8	-0.7	±0.7	0.2	±0.2
pc-Si7	-0.1	±0.9	-0.9	±0.7	0.1	±0.2
pc-Si8	0.3	±0.8	-0.3	±0.7	0.5	±0.2
pc-Si9	0.1	±0.8	-0.6	±0.8	0.3	±0.2
avg.	0.0	±0.8	-0.7	±0.7	0.2	±0.2
ribbon1	-0.5	±0.9	-1.1	±0.7	-0.3	±0.2
micro1	-0.8	±0.4	-1.4	±0.5	-1.1	±0.5
micro2	-1.4	±0.4	-2.4	±0.9	-1.4	±0.5
micro3	-0.7	±0.7	-1.3	±0.6	-0.7	±0.6
avg.	-0.9	±0.5	-1.7	±0.7	-1.1	±0.5
CIGS2	-1.9	±0.3	-2.9	±0.8	-1.8	±0.3
CIGS3	-9.1	±1.2	-9.9	±1.4	-9.3	±1.0
CIGS4	-7.3	±1.0	-8.3	±1.2	-7.4	±0.8
avg. ^a	-1.9	±0.3	-2.9	±0.8	-1.8	±0.3
CdTe2	-1.4	±0.3	-2.1	±0.5	-1.3	±0.3
1j-a-Si1	-1.0	±1.0	-1.5	±0.7	0.7	±0.9
1j-a-Si2	-1.4	±0.8	-1.9	±0.6	-1.6	±0.7
avg.	-1.2	±0.9	-1.7	±0.7	-0.4	±0.8
2j-a-Si1	-1.5	±1.0	-2.1	±0.7	-2.0	±0.7
3j-a-Si1	2.0	±0.7	1.4	±0.6	5.1	±0.8
3j-a-Si2	2.0	±0.7	1.6	±0.7	5.0	±0.8
avg.	2.0	±0.7	1.5	±0.7	5.1	±0.8

^a CIGS3 and CIGS4 excluded.

- Estimated PLR for micromorph technology ranges between $-0.9\%/year$ and $-1.7\%/year$, while it is around $-2\%/year$ and $-1.5\%/year$ for CIGS and CdTe, respectively (values calculated as average on the three investigated methods).
- 1j-a-Si1 shows contradictory results, with positive values of estimated PLR for $P_{max,STC}$ method, and quite strong negative values of estimated PLR for PR_a and $PVUSA_a$ methods. Omitting the positive value, the estimated PLR of single and double junction amorphous silicon technologies can be estimated between $-1\%/year$ and $-2\%/year$.

Fig. 7 shows the variation of estimated PLR and its related uncertainty at increasing number of years considered for the analysis, for the mc-Si5 group. All the investigated technologies actually show similar results: estimated PLR and related uncertainty can significantly differ at the first year depending on the evaluation methodology, and tend to converge from the third year. This trend seems

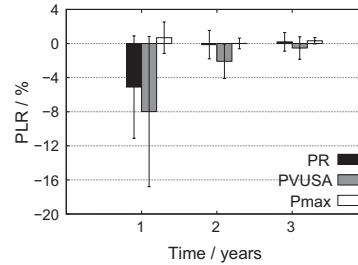


Fig. 7. Estimated PLR at varying number of years of analysis and related error bars, for mc-Si5.

therefore to confirm several studies (Makrides et al., 2014; Jordan et al., 2010) that recommend a minimum period of three years of continuous outdoor data to perform a reliable evaluation of PLR .

5.1. First year and initial performance loss

In this section, two methods are presented that calculate the first year and the initial performance loss rate, respectively. Due to the lack of POA irradiance measurements during the first 6 months of plant operation (August 2010–January 2011), simulated irradiance values were used, see Section 3.1.2 for the description of the simulation methodology. The simulated data were then improved by applying corrective factors retrieved from a linear fit of simulated and measured values, for the following years on a monthly base. For example, data for August 2010 were retrieved by linearly fitting simulated and measured values of pool August 2011, 2012, 2013 and then applying the fitting parameters to the simulated data of August 2010. This way the simulated values matched the measurements better and a more consistent data set was retrieved for the analysis described in this section. Fig. 8 shows the monthly performance metric obtained with the $P_{max,STC}$ method as described in Section 3 for the period February 2011–December 2013 using measured, simulated, and fitted irradiance data as input. Only one example is given to represent each of the nine investigated technologies. The root mean square error for the different technologies, as defined by Eq. (10), was found to be between 0.018 and 0.025 for fitted values, and between 0.034 and 0.045 for simulated values, thus justifying the application of the fitting procedure.

In order to calculate the first year performance loss rate ($FYPLR$) of the investigated technologies, the relative difference between $P_{max,STC}$ of August 2010 and August 2011 was computed:

$$FYPLR = \frac{P_{max,STC, Aug2010} - P_{max,STC, Aug2011}}{P_{max, Aug2010}} \quad (24)$$

An example for this procedure is given in the top of Fig. 9, where $P_{max,STC, Aug2010}$ is the first empty point, and $P_{max,STC, Aug2011}$ corresponds to month number 7. Values of $FYPLR$ are

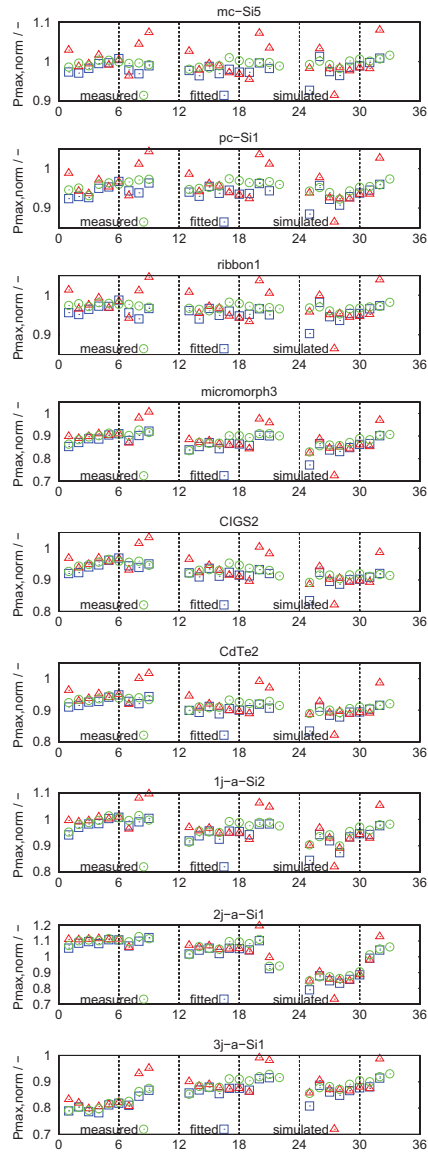


Fig. 8. Monthly performance series calculated with $P_{max,STC}$ evaluation method as described in Section 3, using measured, simulated, and fitted irradiance data (0 = January 2011; 12 = January 2012; 24 = January 2013; 36 = January 2014). $P_{max,STC}$ metric is normalized by nominal power P_n in order to be comparable with Figs. 5 and 6.

shown in Table 4. Only technologies characterized by low scatter in 2010 values are displayed.

As expected, amorphous silicon-based technologies are those showing the highest rate of first year performance loss, with values between -10% and -15% . Similar results

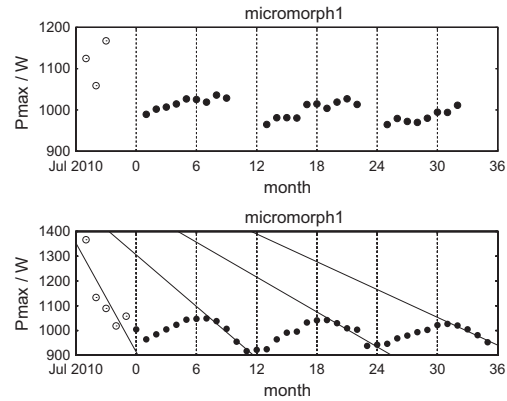


Fig. 9. (top) Example of methodology for the calculation of $FYPLR$, as in Eq. (24). The first empty point represents $P_{max,STC}$ in August 2010, the month 7 corresponds to $P_{max,STC}$ in August 2011. (lower) example of methodology for the estimation of $IPLR$, using Eq. (26). Empty points correspond to the period August–December 2010.

are obtained for CIGS3 and CIGS4, even though these technologies are affected by anomalous degradation process, as discussed in Section 5. More significant is the value for CIGS2, equal to -5.3% . Amongst the other thin-film technologies, micromorph and CdTe tend to lose, respectively, around -9.5% and -7.5% of the initial nominal power during the first year. The last value is in agreement with findings by Makrides et al. (2010), which state -6.2% for the same module technology and manufacturer. Values of $FYPLR$ related to crystalline silicon technologies are between -1% and -1.5% , with the exception of mc-Si4 and mc-Si5 which shows a $FYPLR$ around -5% . In the authors' opinion, these two values are actually too high for such a technology, also with respect to values of -2% to -4% found in literature (Makrides et al., 2010).

Another methodology was developed in an attempt to estimate the initial performance loss rate ($IPLR$). Performance losses occur during the first months of plant operation, mainly due to the process of stabilization of material to electromagnetic irradiance and other environmental constraints. This phase is followed by stabilized performance losses at a constant and usually lower rate (what we called PLR). The duration of stabilization processes depends on the technology, the total received irradiation, the operation temperature (King et al., 2000; DGS, 2013; Ishii et al., 2014). For example, for amorphous silicon technology exposed at Sandia laboratories this process resulted over within the first six months (King et al., 2000). By subtracting the absolute performance loss of the stabilized period to the absolute performance loss of the first months of plant operation, it is possible to isolate the only component ascribable to the stabilization process, here named initial performance loss. To estimate the correspondent rate, $IPLR$, we focus on the first five months of plant operation (August–December 2010). The absolute

Table 4

First year performance loss rate for the investigated technologies, as defined in Eq. (24). Only technologies with low scatter of values of $P_{max,STC}$ in 2010 are displayed.

Tech	FYPLR (%)
mc-Si1 ^a	−1.1
mc-Si4	−5.2
mc-Si5	−4.6
pc-Si8 ^a	−1.4
ribbon1	−1.1
micro1	−9.4
micro2	−10.4
micro3	−9.2
CIGS2	−5.3
CIGS3	−17.0
CIGS4	−13.5
CdTe2	−7.6
1j-a-Si1	−15.1
1j-a-Si2	−10.1
2j-a-Si1	−12.7
3j-a-Si1	−15.3
3j-a-Si2	−15.3

^a Value calculated using September, since production data are not available for August 2010.

performance loss occurred during this five-months period, PL_{2010} , was computed by interpolating monthly averages of $P_{max,STC}$ using Eq. (11) and applying the following expression in place of Eq. (12):

$$PL_{2010} = 5 \cdot a \quad (25)$$

The same procedure was applied to the same months range in the following years to determine PL_{2011} , PL_{2012} and PL_{2013} . $IPLR$ was therefore calculated as follows:

$$IPLR = \frac{PL_{2010} - \frac{PL_{2011} + PL_{2012} + PL_{2013}}{3}}{P_{max,STC, Aug2010}} \quad (26)$$

This way the estimated performance loss occurred in August–December 2010 was cleaned from the estimated average performance loss occurring during the stabilized period, before dividing by the initial estimated value of $P_{max,STC}$ (corresponding to parameter b in Eq. (11)). An example of procedure is shown in the lower Fig. 9 for micromorph1. It is important to note that $P_{max,STC}$ was calculated with Eqs. (1) and (6), i.e. by filtering for $G > 50 \text{ W/m}^2$ and applying irradiance, temperature and spectral corrections. This way, a complete set of $P_{max,STC}$ values can be obtained (filtering for $G > 800 \text{ W/m}^2$ would leave only three points in the period August–December, as displayed in top Fig. 9). On the other hand, as seen in Section 3.4 this method accounts for lower accuracy than filtering for $G > 800 \text{ W/m}^2$ and applying the same corrections. In an attempt to mitigate the uncertainty of this method, especially due to the non-linearity between $P_{max,STC}$ and irradiance values at lower irradiance levels, average monthly $P_{max,STC}$ values were weighted on irradiance in place of computing the arithmetic average. Despite this, the uncertainty associated to the estimation of $IPLR$ is still too high. For example, the micromorph1

displayed in Fig. 9 has an estimated $IPLR$ of -14.9% and an associated uncertainty of 24.9% , which is well above the uncertainty levels calculated for the entire period 2011–2013 and shown in Fig. 4. As a consequence, the values of initial performance loss rate estimated cannot be considered reliable, and are for this reason not reported in this paper.

The methodology proposed, though affected by a high degree of uncertainty, is in the authors' opinion promising. Furthermore, at the authors' knowledge no procedure is currently available to calculate the initial performance loss rate from field data. A possible improvement could be achieved by improving the simulation of broadband and spectral irradiance for the period August 2010–January 2011, e.g. by adopting daily, or even hourly, values of aerosol optical depth instead of monthly values, as well as increasing the time resolution of the other atmospheric input parameters. This would in turn be beneficial to the fitting procedure described in this section as well as to the spectral correction and, in a last instance, to the computation of monthly averages of $P_{max,STC}$.

6. Conclusions

An improved method for the estimation of PLR , named $P_{max,STC}$, is presented and discussed in this paper. It is based on the use of the array generated power metric (P_{max}) corrected for irradiance, temperature and spectral effects to Standard Test Conditions (STC), associated to suitable filtering technique and linear regression. Estimated PLR and its uncertainty are assessed using three years data from twenty-four grid-connected PV arrays representing nine different PV technologies.

The proposed combination of filtering and correction techniques is demonstrated to minimize the uncertainty of estimated PLR , when compared to other combinations. In particular, this study demonstrates that the correction for irradiance, temperature and spectrum of STC conditions improves the accuracy of 25% on average than simply applying a correction for irradiance and temperature.

Results of $P_{max,STC}$ method are then compared with two other widely-recognized performance metrics, namely: the Array Performance Ratio (PR_a) and the Array Photovoltaic for Utility Systems Applications ($PVUSA_a$) (Jordan and Kurtz, 2013). From this comparison it is possible to conclude that the proposed $P_{max,STC}$ method assures the lowest uncertainty of estimated PLR , with a decrease of uncertainty of more than 60% on average with respect to PR_a and $PVUSA_a$ methods when applied on crystalline silicon-based technologies: mc-Si, pc-Si, ribbon. For thin-film technologies, the uncertainty of estimated $P_{max,STC}$ is comparable to the lowest uncertainty between PR_a and $PVUSA_a$ methods. In the authors' opinion, still space for a further improvement of this method exists.

PLR values estimated with $P_{max,STC}$ method are very close to those obtained with PR_a method, with the

exception of amorphous silicon-based technology. In any case, estimated $PLRs$ from $P_{max,STC}$ and PR_a methods are less negative or more positive than $PVUSA_a$ method. Considering the average value of PLR estimated with the three investigated methodologies, this study found typical rates of more than $-0.7\%/year$ for crystalline-based technologies, around $-1.4\%/year$ for micromorph, $-2.2\%/year$ for CIGS, $-1.6\%/year$ for CdTe, $-1.3\%/year$ for 1j-a-Si and $-1.9\%/year$ for 2j-a-Si.

Finally, the first year performance loss rate is assessed by calculating the relative difference between $P_{max,STC}$ of August 2010 and August 2011. In order to extrapolate POA irradiance during the period August–December 2011, for which measurements are not available, a simulation and fitting procedure was used which satisfactorily reproduced the irradiance measurements. Results show rates of -1% to 1.5% for most of crystalline silicon-based technologies (with a few questionable exceptions of about -5%), -9.5% for micromorph, -5% for CIGS, -7.5% for CdTe, and between -10% and -15% for amorphous silicon-based technologies.

Another methodology is proposed to estimate the initial performance loss rate, i.e. the performance loss occurring during the first months solely due to the process of material stabilization. Though affected by a high level of uncertainty, this procedure is in the author's opinion promising to fill the current gap in research of a method to estimate the initial performance loss rate using field data, and will be further improved in future works.

In general, the above mentioned improvements will mainly focus:

- (a) On the adoption of more complex mathematical expressions for module temperature, e.g. by adopting formulas that take the effect of wind cooling into account, and that a study on ABD test facility data has proven to well approximate the corresponding measured values (Skoplaki and Palyvos, 2009).
- (b) On the improvement of the spectral and broadband irradiance simulation methodology, e.g. by increasing the time resolution of atmospheric input parameters. This in order to improve the spectral correction as well as the extrapolated irradiance dataset for missing measurement periods. The use of more than three years of field data will also reduce the error bars and help reducing the uncertainty of all three evaluation methods.
- (c) On the improvement of $P_{max,STC}$ method in order to take thermal annealing effects into account. As shown in Fig. 6, this would further reduce the seasonality in amorphous silicon-based technology, with a further decrease of uncertainty.

This paper shows that the proposed method based on the P_{max} metric corrected for irradiance, temperature and spectral effects to Standard Test Conditions, associated to

suitable filtering technique and linear regression, represents a valid tool for PV module manufactures and installers to reliably estimate the outdoor performance loss rate of both crystalline and thin-film technologies.

Acknowledgements

The authors wish to acknowledge the European Regional Development Fund (ERDF) for financing the project 2-1a-97 PV Initiative and the Stiftung Südtiroler Sparkasse for financing the institute's participation in the IEA Task 13. The authors would also like to thank Reto Stöckli for providing cloud index data and G. Barchi for the fruitful discussion.

References

- Bartholomew, D., Box, G., Jenkins, G., 1971. Time series analysis forecasting and control. *Operat. Res. Quart.* 22 (2), 199–201.
- Belluardo, G., Pichler, M., Moser, D., Nikolaeva-Dimitrova, M., 2012. One-year comparison of different thin film technologies at Bolzano airport test installation. In: Mendez-Vilas, A. (Ed.), *Fuelling the Future: Advances in Science and Technologies for Energy Generation, Transmission and Storage*.
- Carr, A.J., Pryor, T.L., 2004. A comparison of the performance of different PV module types in temperate climates. *Sol. Energy* 76 (1–3), 285–294.
- Castelli, M., Stöckli, R., Zardi, D., Tetzlaff, A., Wagner, J.E., Belluardo, G., Zebisch, M., Petitta, M., 2014. The HeliMont method for assessing solar irradiance over complex terrain: validation and improvements. *Rem. Sens. Environ.* 152, 603–613.
- Chambers, J., Cleveland, W., Kleiner, B., 1983. *Graphical Methods for Data Analysis*. Wadsworth International Group.
- DGS, 2013. *Planning and Installing Photovoltaic Systems: A Guide for Installers, Architects and Engineers*, Routledge.
- Dirnberger, D., Blackburn, G., Müller, B., Reise, C., 2015. On the impact of solar spectral irradiance on the yield of different PV technologies. *Sol. Energ. Mater. Sol. C* 132, 431–442.
- Duffie, J., Beckman, W., 2006. *Solar Engineering of Thermal Processes*, 3rd ed. John Wiley & Sons Inc., New Jersey.
- Fanni, L., Giussani, M., Marzoli, M., Nikolaeva-Dimitrova, M., 2014. How accurate is a commercial monitoring system for photovoltaic plant? *Prog. Photovolt.: Res. Appl.* 22 (8), 910–922.
- G03 Committee, 2012. *Tables for Reference Solar Spectral Irradiances: Direct Normal and Hemispherical on 37 Tilted Surface*. Tech. rep., ASTM International.
- GUM – JCGM 100:2008, 2008. *Evaluation of Measurement Data Guide to the Expression of Uncertainty in Measurement*.
- Huld, T., Dunlop, E., Beyer, H.G., Gottschalg, R., 2013. Data sets for energy rating of photovoltaic modules. *Sol. Energy* 93, 267–279.
- IEC61724:1998, 1998. *Photovoltaic System Performance Monitoring Guidelines for Measurement, Data Exchange, and Analysis*.
- IEC61853-1:2011, 2011. *Photovoltaic (PV) Module Performance Testing and Energy Rating – Part 1: Irradiance and Temperature Performance Measurements and Power Rating*.
- Ishii, T., Otani, K., Takashima, T., Ikeda, K., 2014. Change in IV characteristics of thin-film photovoltaic (PV) modules induced by light soaking and thermal annealing effects. *Prog. Photovolt.: Res. Appl.* 22 (9), 949–957.
- Jordan, D., Smith, R., Osterwald, C., Gelak, E., Kurtz, S., 2010. Outdoor PV degradation comparison. In: 35th IEEE Photovoltaic Specialists Conference, Honolulu, Hawaii, pp. 002694–002697.
- Jordan, D., Wohlgemuth, J., Kurtz, S., 2012. Technology and climate trends in PV module degradation. In: 27th European Photovoltaic

- Solar Energy Conference and Exhibition, Frankfurt, Germany, pp. 3118–3124.
- Jordan, D.C., Kurtz, S.R., 2013. Photovoltaic degradation rates—an analytical review. *Prog. Photovolt.: Res. Appl.* 21 (1), 12–29.
- Kahoul, N., Houabes, M., Sadok, M., 2014. Assessing the early degradation of photovoltaic modules performance in the Saharan region. *Energy Convers. Manage.* 82, 320–326.
- Kamei, A., Yoshida, S., Takakura, H., Minemoto, T., 2014. Ten years outdoor operation of silicon based photovoltaic modules at central latitude of Japan. *Renew. Energy* 65, 78–82.
- Kato, S., Ackerman, T., Mather, J.H., Clothiaux, E., 1999. The k-distribution method and correlated-k approximation for a shortwave radiative transfer model. *J. Quant. Spectrosc. Radiat. Transfer* 62 (1), 109–121.
- Kendall, M., 1976. *Time-Series*, second ed. Dover.
- King, D., Boyson, W., Kratochvil, J., 2004. Photovoltaic Array Performance Model. Tech. rep., SAND2004-3535. Sandia National Laboratories.
- King, D., Kratochvil, J., Boyson, W., 2000. Stabilization and performance characteristics of commercial amorphous-silicon PV modules. In: 28th IEEE Photovoltaic Specialists Conference, Anchorage, Alaska, pp. 1446–1449.
- Köntges, M., Kurtz, S., Jahn, U., Berger, K., Kato, K., Friesen, T., Liu, H., Van Iseghem, M., 2013. Review of Failures of Photovoltaic Modules. Tech. rep., IEA-PVPS T13-01:2014.
- Makrides, G., Zinsser, B., Georghiou, G., Schubert, M., Werner, J., 2010. Degradation of different photovoltaic technologies under field conditions. In: 35th IEEE Photovoltaic Specialists Conference, Honolulu, Hawaii, pp. 2332–2337.
- Makrides, G., Zinsser, B., Schubert, M., Georghiou, G.E., 2014. Performance loss rate of twelve photovoltaic technologies under field conditions using statistical techniques. *Sol. Energy* 103, 28–42.
- Meteoswiss, 2012. CMSAF – Satellite Based Climatologies. <<http://www.meteosuisse.admin.ch>>
- Montgomery, D.C., Peck, E.A., Vining, G.G., 2012. *Introduction to Linear Regression Analysis*. John Wiley & Sons.
- Moser, D., Pichler, M., Nikolaeva-Dimitrova, M., 2013. Filtering procedures for reliable outdoor temperature coefficients in different photovoltaic technologies. *J. Sol. Energy Eng.* 136 (2), 21006.
- Mueller, R., Behrendt, T., Hammer, A., Kemper, A., 2012. A new algorithm for the satellite-based retrieval of solar surface irradiance in spectral bands. *Rem. Sens.* 4 (3), 622–647.
- Munoz, M.A., Alonso-Garcia, M.C., Vela, N., Chenlo, F., 2011. Early degradation of silicon PV modules and guaranty conditions. *Sol. Energy* 85 (9), 2264–2274.
- Ndiaye, A., Charki, A., Kobi, A., Kebe, C.M.F., Ndiaye, P.A., Sambou, V., 2013. Degradations of silicon photovoltaic modules: a literature review. *Sol. Energy* 96, 140–151.
- Ndiaye, A., Kebe, C.M.F., Charki, A., Ndiaye, P.A., Sambou, V., Kobi, A., 2014. Degradation evaluation of crystalline-silicon photovoltaic modules after a few operation years in a tropical environment. *Sol. Energy* 103, 70–77.
- Phinikarides, A., Kindyni, N., Makrides, G., Georghiou, G.E., 2014. Review of photovoltaic degradation rate methodologies. *Renew. Sustain. Energy Rev.* 40, 143–152.
- Pola, I., Chianese, D., Bernasconi, A., 2007. Flat roof integration of a-Si triple junction modules laminated together with flexible polyolefin membranes. *Sol. Energy* 81 (9), 1144–1158.
- Polverini, D., Field, M., Dunlop, E., Zaaiman, W., 2013. Polycrystalline silicon PV modules performance and degradation over 20 years. *Prog. Photovolt.: Res. Appl.* 21 (5), 1004–1015.
- Quintana, M., King, D., McMahon, T., Osterwald, C., 2002. Commonly observed degradation in field-aged photovoltaic modules. In: 29th IEEE Photovoltaic Specialist Conference, New Orleans, Louisiana, pp. 1436–1439.
- REN21 Secretariat, 2014. *Renewables 2014 – Global Status Report*. Tech. rep., Renewable Energy Policy Network for the 21st Century (REN21).
- Schweiger, M., Ulrich, M., Nixdorf, I., Rimmelspacher, L., Jahn, U., Herrmann, W., 2012. Spectral analysis of various thin-film modules using high precision spectral response data and solar spectral irradiance data. In: 27th European Photovoltaic Solar Energy Conference and Exhibition, Frankfurt, Germany, pp. 3284–3290.
- Sharma, V., Chandel, S.S., 2013. Performance and degradation analysis for long term reliability of solar photovoltaic systems: a review. *Renew. Sustain. Energy Rev.* 27, 753–767.
- Skoczek, A., Sample, T., Dunlop, E.D., 2009. The results of performance measurements of field-aged crystalline silicon photovoltaic modules. *Prog. Photovolt.: Res. Appl.* 17 (4), 227–240.
- Skoplaki, E., Palyvos, J., 2009. On the temperature dependence of photovoltaic module electrical performance: a review of efficiency/power correlations. *Sol. Energy* 83 (5), 614–624.
- Wagner, J., Hasel, S., Laube, W., Weihs, P., Rennhofer, M., Berger, K., Leidl, R., Baumgartner, D., 2011. How large is the impact of spectral variability on the energy yield of a-Si, c-Si and CdTe modules? In: Thin Film Conference, Munich, Germany, pp. 153–159.
- Whitaker, C., Townsend, T., Newmiller, J., King, D., Boyson, W., Kratochvil, J., Collier, D., Osborn, D., 1997. Application and validation of a new PV performance characterization method. In: 26th IEEE Photovoltaic Specialists Conference 1997, Anaheim, California, pp. 1253–1256.
- Woyte, A., Richter, M., Moser, D., Reich, N., Green, M., Mau, S., Beyer, H., 2014. Analytical Monitoring of Grid-Connected Photovoltaic Systems – Good Practices for Monitoring and Performance Analysis. Tech. rep., IEA-PVPS T13-03:2014.

6.3 Publication III

The HeliMont method for assessing solar irradiance over complex terrain: validation and improvements

Mariapina Castelli, Reto Stöckli, Dino Zardi, Anke Tetzlaff, Jochen Ernst Wagner, Giorgio Belluardo, Mark Zebisch, Marcello Petitta

Remote Sensing of Environment 152, 603-613



Contents lists available at ScienceDirect

Remote Sensing of Environment

journal homepage: www.elsevier.com/locate/rse

The HelioMont method for assessing solar irradiance over complex terrain: Validation and improvements



M. Castelli^{a,c,*}, R. Stöckli^b, D. Zardi^a, A. Tetzlaff^c, J.E. Wagner^c, G. Belluardo^d, M. Zebisch^c, M. Petitta^e

^a Atmospheric Physics Group, Department of Civil, Environmental and Mechanical Engineering, University of Trento, via Mesiano 77, 38123 Trento, Italy

^b Federal Office of Meteorology and Climatology MeteoSwiss, Krähbühlstrasse 58, 8044 Zürich, Switzerland

^c Institute for Applied Remote Sensing, European Academy of Bolzano, via Druso 1, 39100 Bolzano, Italy

^d Institute for Renewable Energy, European Academy of Bolzano, Via Luis-Zuegg 11, 39100 Bolzano, Italy

^e UPRISE, ENEA Casaccia, Via Anguillarese 301, 00123 Roma, Italy

ARTICLE INFO

Article history:

Received 15 May 2013

Received in revised form 19 June 2014

Accepted 20 July 2014

Available online 13 August 2014

Keywords:

Solar surface irradiance

Diffuse radiation

Aerosols

Radiative transfer modeling

Remote sensing

ABSTRACT

This study evaluates the suitability of the method HelioMont, developed by MeteoSwiss, for estimating solar radiation from geostationary satellite data over the Alpine region. The algorithm accounts for the influence of topography, clouds, snow cover and the atmosphere on incoming solar radiation. The main error sources are investigated for both direct and diffuse solar radiation components by comparison with ground-based measurement taken at three sites, namely Bolzano (IT), Davos (CH) and Payerne (CH), encompassing different topographic conditions. The comparison shows that the method provides high accuracy of the yearly cycle: the Mean Absolute Bias (MAB) is below 5 W m^{-2} at the lowland station Payerne and below 12 W m^{-2} at the other two mountainous stations for the monthly averages of global and diffuse radiation. For diffuse radiation the MAB is in the range $11\text{--}15 \text{ W m}^{-2}$ for daily means and $34\text{--}40 \text{ W m}^{-2}$ for hourly means. It is found that the largest errors in diffuse and direct radiation components on shorter time scales occur during summer and for cloud-free days. In both Bolzano and Davos the errors for daily-mean diffuse radiation can exceed 50 W m^{-2} under such conditions. As HelioMont uses monthly climatological values of atmospheric aerosol characteristics, the effects of this approximation are investigated by simulating clear-sky solar radiation with the radiative transfer model (RTM) libRadtran using instantaneous aerosol measurements. Both ground-based and satellite-based data on aerosol optical properties and water vapor column amount are evaluated. When using daily atmospheric input the estimation of the hourly averages improves significantly and the mean error is reduced to $10\text{--}20 \text{ W m}^{-2}$. These results suggest the need for a more detailed characterization of the local-scale clear-sky atmospheric conditions for modeling solar radiation on daily and hourly time scales.

© 2014 The Authors. Published by Elsevier Inc. This is an open access article under the CC BY-NC-ND license (<http://creativecommons.org/licenses/by-nc-nd/3.0/>).

1. Introduction

An accurate estimation of solar radiation at the Earth surface is a key requirement for climate monitoring and for hydrological and biological applications. Indeed, various biophysical and biochemical processes on the Earth surface are driven by solar radiation, with feedbacks to the rest of the climate system (Bonan, 2002). These include the diurnal development of the atmospheric boundary layer in response to diurnal exchanges of energy, mass and momentum between the atmosphere and the Earth surface and thermally driven flows over complex terrain (Serafin & Zardi, 2010a,b, 2011). Solar radiation is also a main driver for plant photosynthesis and evapotranspiration (Sellers et al., 1997). The spatial and temporal quantification of solar radiation is required for planning and modeling purposes in various areas, such as agriculture,

forestry and oceanography. In particular the role of radiation on the peculiar energy budgets occurring in urban areas and the related effects, such as the urban heat island, have been the subject of recent investigations (Giovannini, Zardi, & de Franceschi, 2011, 2013; Giovannini, Zardi, de Franceschi, & Chen, 2014). Models for quantifying evapotranspiration, which is a major input in soil water balance analyses, also use solar radiation as input, together with other meteorological variables and soil properties (Carrer et al., 2012; Sellers et al., 1996). The assessment of solar energy is also essential in applications converting solar radiation into electricity, such as photovoltaic plants and concentrated solar power systems. One main limitation of the competitiveness of photovoltaic and concentrated solar power systems with other sources of energy is the high cost of the active solar materials. Besides the current research on innovative and more economic semiconductor materials (Barber et al., 2011), another way towards improving the efficiency of solar power is a more accurate estimation of solar radiation at the project development stage. In fact, the evaluation of the direct and diffuse

* Corresponding author at: Via Druso 1, 39100 Bolzano, Italy. Tel.: +39 0471 055 381. E-mail address: mariapina.castelli@eurac.edu (M. Castelli).

components of solar radiation is essential for supporting the choice of the best available technology, i.e. the one that most effectively exploits the radiation available in a target area. Accordingly, the present work aims at investigating the accuracy of the latest modeling techniques for estimating solar radiation at the Earth surface from satellite data in the Alps.

One way for assessing solar irradiance is the analysis of data from ground-based radiometers. The expected error in irradiance calculation is due to the difference between operation and calibration conditions. For high quality and well maintained instruments, such as those used in this study, the World Meteorological Organization (WMO) guidelines admit maximum errors in the hourly radiation totals of 3% (World Meteorological Organization, 2008). Unfortunately in most cases ground networks of radiometers do not cover sufficiently the area of interest. For example in the province of Bolzano, in the Italian Alps, which is the area of major interest for the project which motivated the present work, all measurement stations are located more than 5 km from each other, whereas the spatial autocorrelation of solar radiation is generally less than 1 km (Dubayah, 1992; Dubayah & Paul, 1995). In addition conventional weather stations usually include global radiometers and only few of them are equipped with radiometers measuring either the diffuse or direct component of radiation. Considering the limitations of the network of ground-based instruments, especially over complex terrain, it is necessary to consider other ways for addressing the problem of estimating surface radiation.

Radiative transfer models (RTMs), simulating the incoming solar radiation through all its interactions with the atmosphere and the Earth surface, can for instance be used. These models can simulate the absorbing and scattering effects of atmospheric gases and particles, clouds or surface reflections and shadows (Kato, Ackerman, Mather, & Clothiaux, 1999; Liou, 2002; Stamnes et al., 1988; Stamnes, Tsay, Wiscombe, & Laszlo, 2000). The disadvantage of using RTMs is that accurate calculations are time consuming, thus not convenient for application to large areas. RTMs also require a substantial amount of information concerning rapidly changing atmospheric conditions, such as clouds and aerosol properties. However, the radiative forcing of clouds and, to a certain degree, also aerosol properties can be retrieved from satellite observations. In particular, geostationary satellite data offer a high frequency of observation, thus allowing to observe the daily variability of cloud cover. The main drawbacks of using geostationary satellite data are their coarse spatial resolution and large view angles for higher latitudes. These limitations are particularly severe in mountainous regions, where the altitude varies sharply and affects not only surface related parameters, but also the state of the atmosphere. Furthermore satellite radiometers measure visible radiation reflected by the Earth's atmosphere, thus the retrieval of downward radiation at the Earth surface is not trivial, and requires the modeling of the physical interactions between radiation and aerosols, gases and clouds.

The main effort for retrieving solar radiation at the Earth surface from meteorological satellite data was done in the late eighties (Cano et al., 1986) for Meteosat radiometers data. The idea was to correlate the observed reflectivity of each pixel with its cloudiness. First a reference surface albedo map was evaluated statistically. Then a cloud index n , a surrogate for the cloud radiative forcing of a pixel, was calculated. It was defined as the measured albedo, ρ , normalized to the difference between its maximum (ρ_{max}), observed under overcast sky conditions, and minimum (ρ_{min}), corresponding to a reference albedo calculated for cloud-free conditions:

$$n = \frac{\rho - \rho_{min}}{\rho_{max} - \rho_{min}} \quad (1)$$

A linear proportionality was assumed between irradiance at the top of the atmosphere and global radiation at the Earth surface, the coefficient of proportionality being the so called atmospheric transmission factor, K . The factor K was calculated as an empirical function of n by

using pyranometric measurements as test dataset (Fontoynt et al., 1997, 1998; Hammer et al., 2003). The original radiation retrieval method was called HELIOSAT and was proposed in many formulations following different sensor generations (Beyer, Costanzo, & Heinemann, 1996; Hammer et al., 2003; Rigollier, Lefèvre, & Wald, 2004), mainly changing the clear-sky model used for calculating cloud-free irradiance and the relation between n and K .

One version of HELIOSAT which analyzes the peculiar conditions of mountainous areas was proposed by Dürr and Zelenka (2009) specifically for the Alps. This model includes snow detection, pixel georeferencing, satellite view angle distortion fixing, and terrain shading calculation. Despite its comprehensiveness, this algorithm approximates the transmissivity of the atmosphere only through monthly climatological values of the Linke turbidity coefficient (Remund, Wald, Lefvre, Ranchin, & Page, 2003). The turbidity is included in the empirical clear-sky model of Kasten, Dehne, Behr, and Bergholter (1984), and does not affect the procedure used to calculate the diffuse radiation fraction. At the same time a new clear-sky model for HELIOSAT was proposed: the algorithm SOLIS (Müller et al., 2004). The latter is based on RTM simulations of clear-sky irradiance. Later on SOLIS was modified introducing the computationally efficient *look up tables* approach, which means that RTM runs were performed for discrete values of the atmospheric parameters, and then an interpolation was performed in dependence of atmospheric input data. This model was called MAGIC (Müller et al., 2009). Radiation values obtained with the *look up tables* approach differ from the exact RTM solutions by no more than $1\text{--}2 \text{ W m}^{-2}$. Recently MeteoSwiss has coupled the MAGIC clear-sky model with a new processing scheme for the all-sky retrieval of solar radiation at surface. This new algorithm, called HelioMont, is comprehensively documented in Stöckli (2013) and briefly described in the next section.

HELIOSAT versions including the *look up tables* approach were variously validated and results are reported in many papers. For example in Ineichen et al. (2009) the hourly averages of global irradiance were validated against 8 European stations during 4 months. An overall Root Mean Square Error (RMSE) between 80 and 100 W m^{-2} and Mean Bias Deviation (MBD) between -15 and 20 W m^{-2} were found. Clear-sky and overcast conditions were also considered separately, finding an underestimation in the first case and an overestimation in the second one. The underestimation in clear-sky cases was also correlated to an overestimation of the Aerosol Optical Thickness (AOT) used for the interpolation from the look up tables. Furthermore, Journée and Bertrand (2010) validated global irradiance at 13 sites in Belgium. The 10 minute averages of ground measurements were compared to the satellite estimations derived from the corresponding instantaneous observations, with a resolution of 1 h. Mean Absolute Bias (MAB) larger than 60 W m^{-2} and MBD between -18 and 8 W m^{-2} were observed. An underestimation in clear-sky conditions has been noticed also in the last mentioned paper. Some validation results can also be found in Betcke et al. (2006). However, to the best of our knowledge, no detailed analysis of the diffuse and direct irradiance components calculated with the *look up tables* approach has been done so far. Moreover no validation studies have been performed with satellite-derived solar irradiance over complex terrain, with the exception of Dürr et al. (2010).

This paper aims at assessing the reliability of the HelioMont method for retrieving irradiance from Meteosat Second Generation (MSG) satellite data at three specific measurement locations in the Alps encompassing different topographic conditions. In particular the realism of the algorithm in estimating the direct and diffuse components of solar radiation is investigated with respect to atmospheric input data, such as aerosol properties.

The structure of this paper is as follows: Section 2 describes the algorithm HelioMont and gives the technical details of the ground measurements used for the validation; Section 3 presents the results of the validation on different time scales and under different sky conditions; Section 4 shows the results of RTM simulations of solar radiation to emphasize the role of aerosols; in the last section the conclusions

derived from the outcome of the present analysis are summarized and discussed, and possible applications of the results are proposed.

2. Data and method

The present study validates shortwave solar radiation at the Earth surface, derived by MeteoSwiss from MSG data, against surface based point measurements. We investigated separately global irradiance (SIS, Surface Incoming Shortwave Radiation) and its diffuse (SISDIF, Surface Incoming Shortwave Radiation – Diffuse component) and direct normal (SISDNI, Surface Incoming Shortwave Radiation – Direct Normal Irradiance) components, since they can be used in different applications and their relative amount influences the efficiency of their exploitation.

The statistical parameters adopted here to compare the irradiance components are the Mean Bias Deviation (MBD), the Mean Absolute Bias (MAB), the Root Mean Square Error (RMSE), and the R squared correlation coefficient of the linear regression between satellite estimate and ground-based measurements (R^2). All these parameters are calculated according to the formulation of Wilks (2011), i.e.:

$$MBD = \frac{1}{n} \sum_{i=1}^n (S_i - G_i) \quad (2)$$

$$MAB = \frac{1}{n} \sum_{i=1}^n |S_i - G_i| \quad (3)$$

$$RMSE = \sqrt{\frac{1}{n} \sum_{i=1}^n (S_i - G_i)^2} \quad (4)$$

where S_i is the modeled variable and G_i is the observed variable averaged in the i th time interval. Since the processing of MSG data is limited to slots corresponding to sun elevation angles above 3° , we filled the few missing MSG data using the relation between all-sky and cloud-free irradiance, whose ratio is generally referred to as clear-sky index (k). We calculated the daily average clear-sky index (k_d), both for global and direct irradiance, as the ratio between the daily mean irradiance and the daily mean clear-sky radiation:

$$k_d = \frac{SIS_d}{SIS_{d, \text{cloud-free}}} \quad (5)$$

Afterwards we replaced instantaneous missing data with the product of k_d and the instantaneous clear-sky irradiance, which is modeled with the MAGIC approach:

$$SIS(\text{missing}) = k_d \times SIS_{\text{cloud-free}} \quad (6)$$

The cloud-free SISDNI was calculated as the ratio between the cloud-free direct irradiance and the cosine of the sun zenith angle θ .

After filling the gaps for missing values, we generated hourly and daily means of MSG data from instantaneous measurements taken every 15 min, while we aggregated hourly and daily averages of ground-based data from measurements taken at 1 min sampling interval. In both cases monthly means were produced from daily means, considering only those days in which both satellite and ground measurements were available. The procedure, generally adopted in literature, of comparing instantaneous satellite data with the synchronous 10 min averages of ground measurements, was not used in this paper, because the scope was to investigate if the model describes properly the variability of solar radiation at different time resolutions, rather than if it accurately reproduces ground measurements at the time of acquisition.

First we validated *all-sky* data. Then we split them according to three sky condition categories, namely *cloud-free*, *thin clouds* and *overcast*, and

repeated the validation for each class. The discrimination was performed coherently with the cloud mask calculated with the method of Stöckli (2013), presented in the next subsection.

2.1. The method HelioMont for deriving SIS from MSG data

The algorithm implemented by MeteoSwiss for retrieving solar radiation from MSG data is presented in detail in Stöckli (2013) and shortly summarized here. Data from the SEVIRI (Spinning Enhanced Visible and Infrared Imager) instrument onboard the MSG satellites are used. This instrument has 12 channels in the visible and infrared bands for monitoring the reflected solar radiation and thermal emission of the Earth. SEVIRI has a spatial resolution at nadir of around 1 km for the high resolution visible channel and 3 km for the other channels.

The retrieval of the clear-sky global and direct beam irradiance is based on the GNU-MAGIC clear-sky model (Müller et al., 2009). RTM simulations with libRadtran (Mayer et al., 2005) are conducted for discrete values of aerosol optical properties, total column water vapor and ozone concentrations. The resulting look up tables are then applied to 6-hourly atmospheric states (water vapor and ozone) determined on the basis of numerical model output from ECMWF (Dee et al., 2011) and a monthly aerosol climatology (Kinne, 2009).

The cloud effect on clear-sky SIS is calculated by applying the well established HELIOSAT algorithm for dark surfaces, extended by a newly developed near-infrared and infrared cloud index for bright surfaces such as snow and desert. For identifying the state of each pixel MeteoSwiss adopts a probabilistic cloud mask based on the algorithm SPARC (Separation of Pixels using Aggregated Rating over Canada), proposed by Khlopenkov and Trishchenko (2007). The method was originally developed for AVHRR (Advanced Very High Resolution Radiometer) and adapted by MeteoSwiss to MSG SEVIRI (Fontana, Stöckli, & Wunderle, 2010). While most cloud masks use a classification tree, SPARC produces an additive rating from individual tests, which represents the probability of cloud contamination for each pixel. In addition to analyzing temperature, reflectance, and their spatial uniformity, two new tests are added to SPARC for testing the temporal variability of reflectance and temperature.

The surface radiation is finally calculated by scaling the expected clear-sky radiation with the clear-sky index (k), which is a function of the cloud index:

$$SIS = k(n) \times SIS_{\text{cloud-free}} \quad (7)$$

MeteoSwiss has also implemented correction methods accounting for the effects of topography, such as shadowing, reflection, local horizon elevation angle and sky view factor. The Shuttle Radar Topography Mission (SRTM) digital elevation model, with a spatial resolution of 3 arc sec, is upscaled to $0.02^\circ \times 0.02^\circ$ and used to determine the altitude and the horizon of each pixel.

2.2. Ground-based radiation data

We used three ground stations for the validation, two in the Swiss Alps and one in the Italian Alps (Fig. 1). All of the stations measure SIS, SISDIF and SISDNI.

The station of Bolzano (IT) is located at the valley floor, at an altitude of 262 MSL, at the junction of the three valleys: Val d'Isarco, Val Sarentina and Val d'Adige. The instruments are mounted at 1 m above ground, and in the surroundings there are the airport runway, crops and industrial facilities. In Bolzano observations are collected by three Kipp & Zonen instruments, i.e. 2 pyranometer model CMP11 (one measuring global irradiance and the other one combined with a sun tracker equipped with a shadow sphere that intercepts direct solar radiation for measuring diffuse radiation), and a pyrhelimeter model CHP1 measuring direct irradiance. All the instruments used for the validation are regularly calibrated once per year.

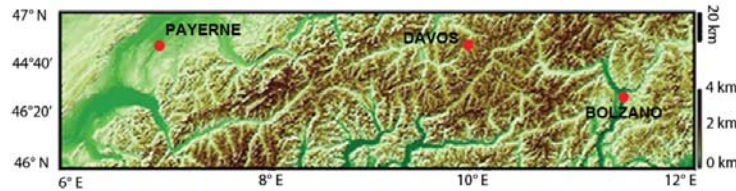


Fig. 1. Digital elevation model of the area of interest. Data from SRTM/NASA (Shuttle Radar Topography Mission) at 3 arc-second resolution. The red dots represent the measurement stations of solar radiation which we used in this study.

In Davos (CH) instruments are mounted at the Physical-Meteorological Observatory and World Radiation Center (PMO/WRC), at an altitude of 1610 MSL, on the wind mast of the Swiss Meteorological Institute, with grassland underneath. Data from Davos used in the present analysis were measured by two Kipp & Zonen CM21 pyranometers, one for global and the other for diffuse irradiance, and a Kipp & Zonen CHP1 pyrliometer for direct normal irradiance. All the radiation instruments are mounted on an arm fixed at about 2 m distance from the main mast and about 4–8 m above the ground. The pyranometer measuring diffuse irradiance is equipped with a fixed shadow band pointing South.

The station of Payerne (CH) is part of the Baseline Surface Radiation Network (BSRN), which is a project of the Radiation Panel from the Global Energy and Water Cycle Experiment. The experiment aims at acquiring the best possible surface radiation budget information, and was initiated by the World Climate Research Programme. The radiation instruments of Payerne are located at MeteoSwiss, at an altitude of 491 MSL, and have grassland with crops in the vicinity. In Payerne direct normal irradiance is measured with a Kipp & Zonen CHP1, whereas global and diffuse irradiance are measured by two Kipp & Zonen CM21 pyranometers.

For this validation study we adopted 2011 as test year for performing the comparison between satellite and ground data in Bolzano and Davos, while in Payerne we carried out the analysis with data since 2004 to 2009, according to the availability of ground measurements.

2.3. Satellite and ground-based atmospheric data

In order to test the sensitivity of radiation components to atmospheric input, we also simulated solar radiation and its direct and diffuse components with the RTM libRadtran by using atmospheric inputs with a higher temporal resolution than the climatological ones used in the method of Stöckli (2013).

At the first stage, we took AERONET (AERosol RObotic NETWORK) measurements of Aerosol Optical Thickness (AOT), Single Scattering Albedo (SSA), and precipitable water. AERONET is a global network of Sun Photometers (Holben et al., 1998). The sun photometer performs one direct measurement pointing at the sun, and one direct at the sky, at different wavelengths in the range 0.3–1.02 μm . This set of measurements allows a direct estimation of aerosol macro-physical properties such as AOT, and an indirect estimation of micro-physical properties, like the SSA. All the data from the sites around the world are collected and processed by NASA. Level 1.5 (cloud-screened) AOT, SSA and water vapor data for the stations of Bolzano and Davos have been downloaded from the AERONET website (<http://aeronet.gsfc.nasa.gov>).

At the second stage, considering the low number of AERONET stations in the Alps, for water vapor column amount we used the ERA Interim reanalysis of the ECMWF (European Centre for Medium-Range Weather Forecasts) at 0.25×0.25 degree grid, and for aerosol satellite data, specifically MODIS (MODerate resolution Imaging Spectroradiometer) retrieval of AOT, and OMI (Ozone Monitoring Instrument) SSA product. The instrument MODIS is on the EOS (Earth Observing System) Terra and Aqua polar orbiting satellites. It has 36 spectral bands between 0.41 and 14 μm . The satellites Terra and Aqua

cross Europe at around 10:30 and 13:30 local solar time. MODIS AOT Collection 5 (Levy, Remer, Mattoo, Vermote, & Kaufman, 2007) overland retrievals use four channels centered at 0.47, 0.66, 1.24 and 2.1 μm with a nominal resolution of 500 or 250 m at nadir. To reduce noise, the AOT at 0.55 μm is calculated in boxes of $10 \times 10 \text{ km}^2$, averaging the 20 to 50 percentile of surface reflectance in each box. OMI is on EOS Aura polar orbiting satellites. Its measurements cover the spectral region between 264 and 504 nm, with a spectral resolution between 0.42 nm and 0.63 nm and a nominal ground footprint of $13 \times 24 \text{ km}^2$ at nadir. Complete global coverage is achieved in one day.

3. Results

3.1. Validation of all-sky SIS, SISDIF and SISDNI

The results of the validation for the three stations of interest are summarized in Tables 1–3, respectively on the hourly, daily and monthly time scale, in terms of MAB and MBD, including both the all-sky and the specific sky conditions.

The validation of the monthly averages (Fig. 2(a)–(b)) indicates that the satellite estimation is useful to reproduce the seasonal cycle of the components of global radiation with a MAB of 3 W m^{-2} in flat terrain like Payerne and 7 and 12 W m^{-2} in steep terrain like Davos and Bolzano, respectively. Despite the agreement between the monthly averages of satellite and ground-based data, both in Bolzano and Davos diffuse irradiance is always overestimated by the satellite algorithm in the period of analysis (Table 3). This makes it interesting to investigate what happens on shorter time scales.

In Bolzano positive values of MBD were observed for all the irradiance components, both in the monthly, daily and hourly validation, suggesting that satellite data generally overestimate irradiance at this location. The local minimum of the monthly averages of SIS and SISDNI in June (Fig. 2(a)) is clearly associated with the low number of cloud-free days (only 2) and with the secondary peak of convective precipitations

Table 1

MAB and MBD (W m^{-2}) of the validation of hourly averages of global (GLO), diffuse (DIF) and direct normal (DNI) radiation for different sky conditions in Bolzano, Davos and Payerne.

Station	Years	Sky cond.	MAB [W m^{-2}]			MBD [W m^{-2}]		
			GLO	DIF	DNI	GLO	DIF	DNI
Bolzano (IT)	2011	All sky	52	40	128	6	15	-10
		Cloud-free	40	45	116	17	36	-24
		Thin clouds	51	31	121	4	-1	16
		Overcast	62	35	137	-17	-10	-18
Davos (CH)	2011	All sky	52	42	144	-6	14	-49
		Cloud-free	27	41	134	-5	38	-89
		Thin clouds	54	30	182	6	9	2
		Overcast	72	48	136	-12	-2	-45
Payerne (CH)	2004–2009	All sky	40	34	110	2	-5	22
		Cloud-free	20	30	96	10	12	-6
		Thin clouds	46	29	148	15	-13	73
		Overcast	49	38	89	-8	-11	17

Table 2
MAB and MBD ($W m^{-2}$) of the validation of daily averages of global (GLO), diffuse (DIF) and direct normal (DNI) radiation for different sky conditions in Bolzano, Davos and Payerne.

Station	Years	Sky cond.	MAB [$W m^{-2}$]			MBD [$W m^{-2}$]		
			GLO	DIF	DNI	GLO	DIF	DNI
Bolzano (IT)	2011	All sky	14	15	33	4	8	4
		Cloud-free	30	40	91	19	31	-5
		Thin clouds	46	30	115	1	-2	9
Davos (CH)	2011	Overcast	47	21	124	-20	-7	-31
		All sky	14	15	33	-2	7	-11
		Cloud-free	19	34	102	1	33	-70
Payerne (CH)	2004–2009	Thin clouds	49	24	162	7	4	22
		Overcast	51	29	102	-16	-2	-34
		All sky	10	11	31	1	-3	12
		Cloud-free	19	24	91	12	3	24
		Thin clouds	41	27	140	14	-13	74
Overcast	32	25	70	-9	-12	16		

which is typically observed in the Alps. The validation of the daily averages (Table 2) outlines difficulties in estimating diffuse irradiance from satellite data ($R^2 = 0.758$, $MBD = 8 W m^{-2}$, $MAD = 15 W m^{-2}$). Analogous results were observed for the hourly averages (Table 1) ($R^2 = 0.735$, $MBD = 15 W m^{-2}$, $MAD = 40 W m^{-2}$).

In Davos (Fig. 2(b)) the validation gives results similar to those recorded for Bolzano. A minimum of SIS and SISDNI is observed again in summer, and is associated with the high number of cloudy days (in June and July there were only 2 cloud-free days in total). Both monthly, daily and hourly analyses show that satellites overestimate diffuse irradiance ($MBD > 12\%$) and underestimate direct normal irradiance ($MBD < -4\%$), although global irradiance turns out to be slightly underestimated in the hourly ($MBD = -6 W m^{-2}$) and daily ($MBD = -2 W m^{-2}$) analysis. Like for Bolzano, daily averages of diffuse irradiance are not as strongly correlated with ground data ($R^2 = 0.808$) as for global irradiance ($R^2 = 0.909$).

In Payerne (Fig. 2(c)) the validation shows high accuracy of the monthly-mean satellite global irradiance ($MAB = 3 W m^{-2}$, $MBD = 1 W m^{-2}$), and diffuse irradiance is only slightly underestimated ($MBD = -3 W m^{-2}$), whereas direct normal irradiance is overestimated ($MBD = 14 W m^{-2}$). The daily averages of the diffuse component over the 6 years of analysis are underestimated ($MAB = -3 W m^{-2}$) with $R^2 = 0.853$.

After having summarized the outcome of the analysis, it is important to clarify that the results obtained in Payerne are not climatologically equivalent to the ones obtained for the other two stations. The periods of investigation, in fact, have different lengths and do not overlap. In Bolzano and Davos we validated data of the year 2011 only, thus results are affected by the specific conditions of the year under investigation and are suitable for understanding if the satellite algorithm describes properly the short term variability of the irradiance components. On the other hand, results for Payerne were derived from the analysis of six years of data, consequently they can be considered representative

Table 3
RMSE, MAB and MBD ($W m^{-2}$) for the monthly averages of global (GLO), diffuse (DIF) and direct normal (DNI) radiation in Bolzano, Davos and Payerne. The second row indicates for each station the same parameters in percentage of the corresponding mean value of ground measurements.

Station	GLO			DIF			DNI		
	RMSE	MAB	MBD	RMSE	MAB	MBD	RMSE	MAB	MBD
Bolzano	16	12	6	12	10	9	27	23	8
	6%	7%	4%	22%	1%	16%	14%	12%	4%
Davos	9	7	-1	9	7	7	18	13	-11
	5%	5%	0.2%	14%	14%	13%	9%	10%	-9%
Payerne	4	3	2	6	5	-3	21	18	14
	3%	2%	1%	9%	8%	-4%	15%	12%	10%

for the long term pattern of the error in the satellite estimation of solar radiation.

3.2. Validation of the mean diurnal cycle of SIS, SISDIF and SISDNI

In Bolzano and Davos the mean diurnal cycle (Fig. 3) reveals a strong overestimation of diffuse irradiance. Furthermore global irradiance is overestimated in the morning and underestimated during the rest of the day.

In Payerne the mean diurnal cycle (Fig. 4) shows a strong overestimation of direct normal irradiance, while diffuse irradiance is underestimated around noon, and global irradiance is overestimated in the morning and underestimated in the afternoon, similarly to the results observed for Bolzano and Davos.

The strong diurnal cycle of the estimation error is likely connected to the difference in spatial footprint of the data that we compared. A satellite pixel of $2 km^2$ represents, in fact, the mean over substantial subgrid-scale topographic variability (slope, orientation, horizon altitude) and surface reflectance, whereas a station measurement is representative only for a small part of these topographic boundary conditions.

3.3. Validation of SIS, SISDIF and SISDNI under different sky conditions

In order to examine the most problematic conditions, we split data in classes according to the season and to the cloudiness status. Three cloudiness classes, i.e. cloud-free, thin clouds and overcast, were adopted, in accordance with the cloud mask computed by HelioMont. We considered an hour either cloud-free or overcast only if the cloud mask was equal to 0 or 2 respectively for all the time slots, while we classified an hour as thin clouds for mean hourly values of the cloud mask between 0.8 and 1.2. The remaining intermediate cases were excluded for avoiding mixing different sky conditions. For computing daily averages we selected only those hours in which both satellite and ground data belonging to a specific class were available.

The hourly (Table 1) and daily (Table 2) validation shows that in cloud-free conditions the estimation error of the irradiance components is much higher than in the other cases, especially in Bolzano and Davos, where diffuse radiation is strongly overestimated (MBD is in the range $31-38 W m^{-2}$) and direct normal irradiance is underestimated up to $89 W m^{-2}$. Considering these results, we calculated the monthly averages of diffuse radiation including only the time interval between 10 a.m. and 2 p.m., in order to quantify the influence on the yearly cycle of the estimation error considering only those hours in which most radiation is available (Fig. 5). In Bolzano and Davos MBD and MAB resulted much higher than under the other sky conditions, while in Payerne there was the opposite situation (see Table 4 for MBD and MAD values under thin clouds and overcast conditions). For direct normal radiation, MAD under cloud-free conditions was equal to 67, 103 and $55 W m^{-2}$ respectively in Bolzano, Davos and Payerne. In this case the error was comparable to the one observed under the other sky conditions.

In the next subsection we examine possible causes of error in the satellite estimation of diffuse radiation under clear-sky conditions.

3.4. Sources of error in the estimation of diffuse radiation

The behavior observed under clear-sky conditions can be partially explained considering processes and factors contributing to diffuse irradiance in the absence of clouds. They can be summarized as follows, together with a description of the model simplifications:

1. Mie scattering by aerosols is weakly wavelength selective, and particularly effective on visible light, where most of solar energy is concentrated: monthly values of aerosol optical characteristics are used to interpolate irradiance values from the look up tables. The

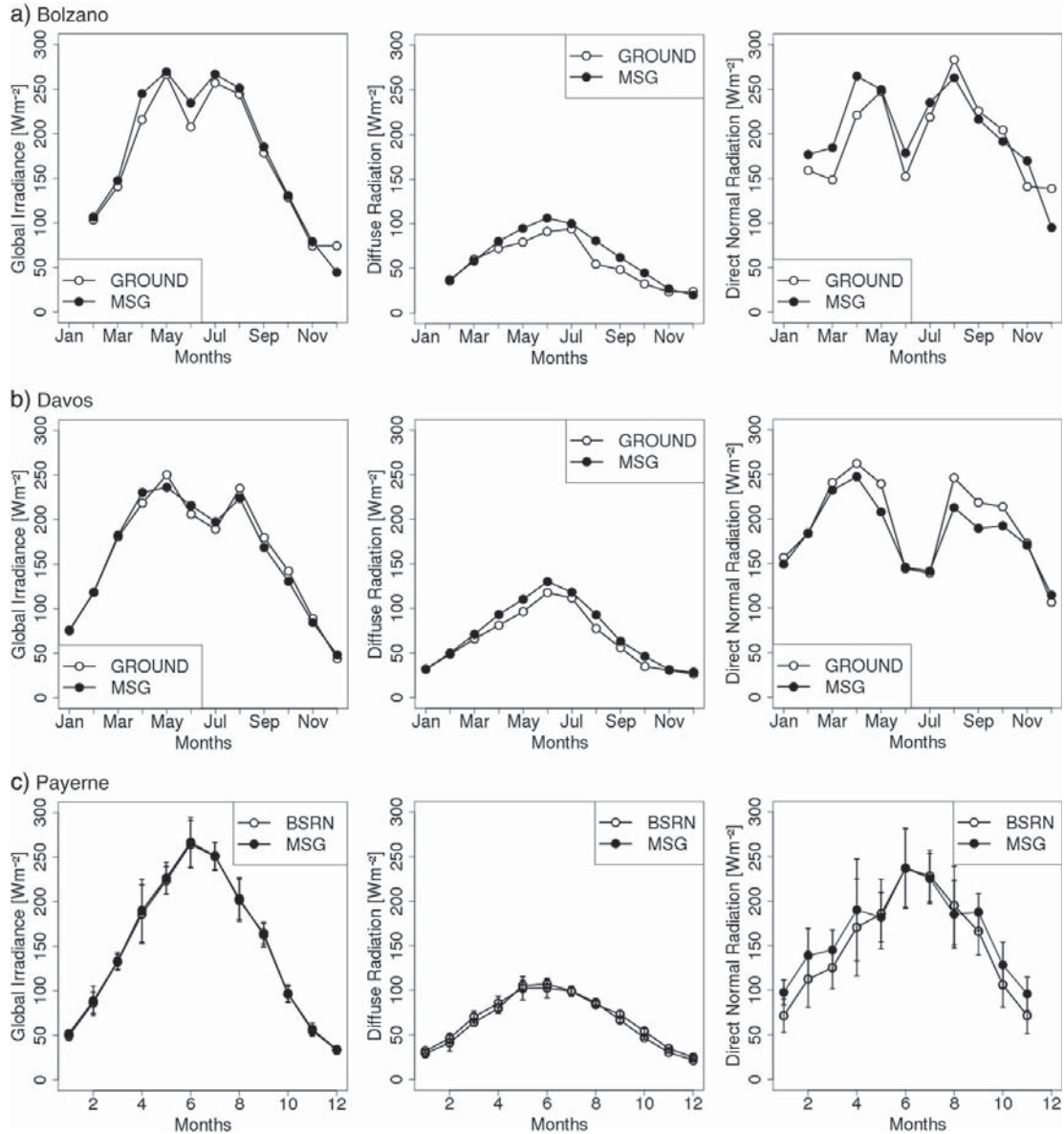


Fig. 2. Monthly averages of satellite and ground-based irradiance in Bolzano (2011), Davos (2011) and Payerne (2004–2009). The local minima of global and direct normal irradiance in June and July in Bolzano and Davos are due to the high percentage of cloudy days. In Bolzano no data were available for January because the radiometers were installed in February 2011. In panel (c) the error bars represent the inter-annual standard deviation of monthly averages of satellite and ground measurements. Given its low variability from year to year, the climatology of SISDIF can be considered representative of the single years.

global-scale $1^\circ \times 1^\circ$ aerosol data cannot represent the vertical stratification of aerosols within the atmospheric boundary layer in complex topography. AOT at high elevation locations is thus likely to be overestimated by the satellite retrieval;

- the global modeling approach of Kinne (2009) provides general information on amount, spatial distribution, and seasonality of aerosol properties at global scale, but is not representative for areas

characterized by local complex orography. Both in Bolzano and Davos, in fact, the aerosol Kinne climatology adopted in Stöckli (2013) overestimates AOT, with a MBD of 0.1 in Davos (9 months of continuous measurements available), and 0.09 in Bolzano (only 3 and half months of measurements available) with respect to monthly averages of AERONET AOT in 2011. This causes the overestimation of diffuse radiation from satellite data;

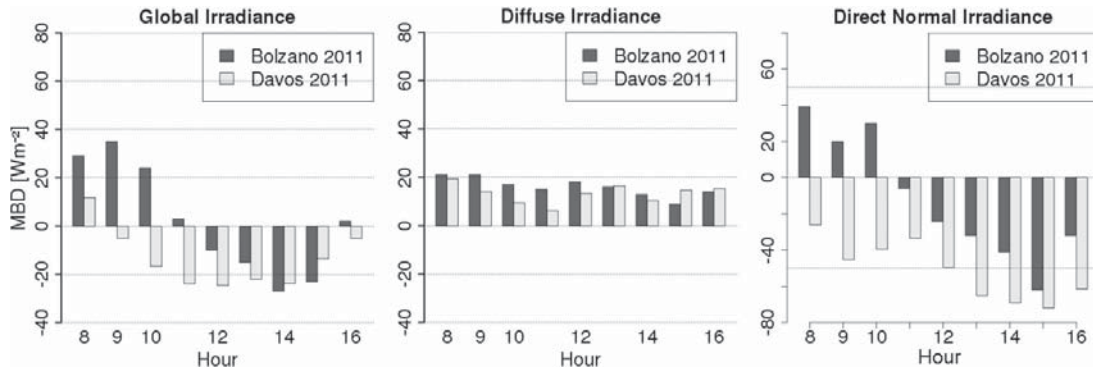


Fig. 3. Mean diurnal cycle of MBD of irradiance components in Bolzano and Davos. Only the data between 8 a.m. and 4 p.m. are represented because they are descriptive of the entire dataset, in fact in the remaining hours, during autumn and winter, the sun is below the local horizon.

- Rayleigh scattering by atmospheric gases, whose effectiveness is confined in the ultraviolet part of solar spectrum, is much less relevant than Mie scattering on broadband radiation: the model assumes a fixed atmospheric profile (US standard atmosphere) and uses the *Kato band-parameterization* (Kato et al., 1999);
- Surface reflection: the impact of surface albedo on clear-sky irradiance is approximated by using the clear-sky top-of-atmosphere reflectance as a surrogate for surface albedo. This approximation would need to be replaced by the estimation of an atmospherically corrected hemispherical surface albedo;
- The sky-view-factor (see the next section for its definition) reduces diffuse radiation according to the visible portion of the sky vault: it is calculated from the horizon angle, thus is affected by the low resolution of the DEM, originally set at a resolution of 100 m, and then upscaled to the MSG high resolution visible channel pixel size, which is around 1 km East–West and around 1.7 km North–South. It is thus likely that the local-scale sky-view-factor at the valley stations Bolzano and Davos is lower compared to the sky view factor of the mean MSG high resolution visible channel pixel;
- The diffuse-to-global ratio increases with optical air mass, i.e. with the sun zenith angle: this effect is considered by applying the *modified Lambert–Beer* relation, developed and validated in Müller et al. (2004) and EHF, UiB, and ARMINES (2003), and also verified in Ineichen (2006).

To summarize, the most critical approximations in the satellite-based clear-sky model are associated with aerosol scattering and surface reflectance. More in-depth examination is necessary for solving the surface-related issues. These problems have been partially addressed in Lee, Liou, and Hall (2011). In the next section we investigate the effects of aerosols and suggest a way to introduce more accurate data in the model.

4. Modeling the effect of aerosols

Since the validation study highlighted problems in the estimation of irradiance components under clear-sky conditions, it is interesting to quantify the influence of atmospheric absorption and scattering on direct and diffuse solar radiation. We carried out this study for Bolzano and Davos, which are equipped with a sun-photometer measuring aerosol optical properties and water vapor column amount, and are part of the AERONET network. The most interesting days to investigate would have been the summer days in which the largest discrepancy was observed. However data analysis had to be adapted to data availability, thus it was limited to the months containing most cloud-free days and for which most AERONET data were available, i.e. August for Bolzano and November for Davos.

We used AERONET measurements of AOT, SSA, and precipitable water. Then we calculated daily averages of these atmospheric parameters and

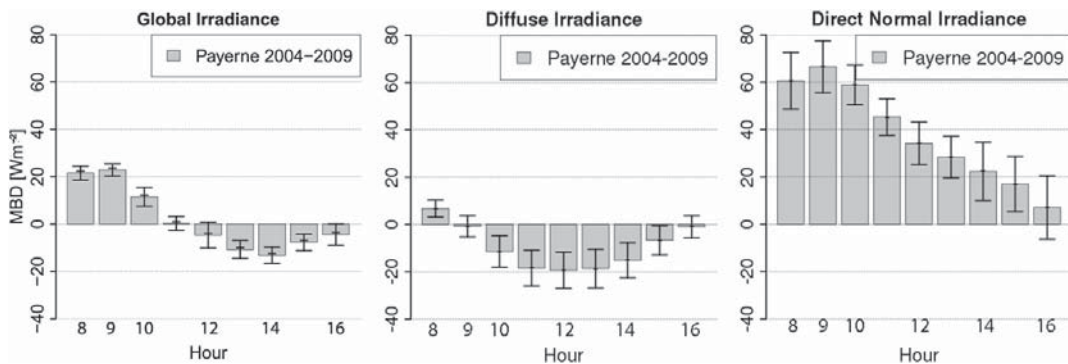


Fig. 4. Mean diurnal cycle of MBD of irradiance components in Payerne. Only the data between 8 a.m. and 4 p.m. are represented because they are descriptive of the entire dataset, in fact in the remaining hours, during autumn and winter, the sun is below the local horizon. The error bars represent the standard deviation of the daily cycle of MBD in the 6 years 2004–2009.

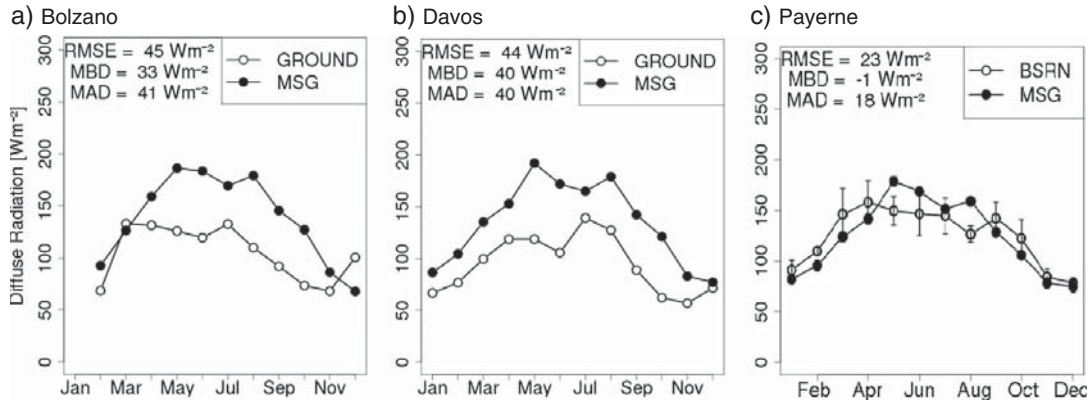


Fig. 5. Monthly averages of satellite and ground measurement of diffuse irradiance in Bolzano (2011), Davos (2011) and Payerne (2004–2009) under clear-sky conditions. Only the time interval between 10 a.m. and 2 p.m. was considered in the averaging of cloud mask and irradiance because in these hours most of the irradiance is available.

assumed them constant throughout each day in the simulations. The surface albedo was derived from the MODIS/Terra + Aqua Albedo 16-Day product (MCD43C3) with a resolution of 0.05° . Ozone column amount was set constant and equal to 300 Dobson units.

We modeled diffuse and direct radiation by the RTM libRadtran (Fig. 6), adopting as radiative transfer equation solver the discrete ordinate code *disort* (Stamnes et al., 1988) with 6 streams. The correlated- k approach of Kato et al. (1999) was used to compute the spectral transmittance assembling the absorption coefficients of different gases. We performed RTM runs every 15 min in the time interval between 10 a.m. and 2:45 p.m. in which the influence of shadowing is the smallest.

We reduced the simulated diffuse irradiance considering the sky view factor, f_s :

$$SISDIF_{cor} = SISDIF \times f_s + SISDIF \times \alpha(1-f_s) \quad (8)$$

where α is the surface albedo and f_s is the ratio between diffuse irradiance at a point and that on an unobstructed horizontal surface (Dozier & Marks, 1987) under the assumption of isotropic distribution of diffuse irradiance. The skyview factor was calculated for Bolzano and Davos from the horizon angle, and was equal, respectively, to 0.947 and 0.953.

As shown in Fig. 7(a) and (b), libRadtran simulates diffuse radiation with high accuracy when site-specific aerosol and water vapor measurements are used (MAB on hourly averages is 11 W m^{-2} in Bolzano and 5 W m^{-2} in Davos, MBD is 4 W m^{-2} in Bolzano and -5 W m^{-2} in Davos), while the satellite estimate significantly exceeds ground measurements in clear-sky days (MBD is 73 W m^{-2} in Bolzano and 32 W m^{-2} in Davos). Simulated direct irradiance is also very close to ground truth (MAB on hourly averages is 20 W m^{-2} in Bolzano and 10 W m^{-2} in Davos, MBD is 14 W m^{-2} in Bolzano and -4.5 W m^{-2}

Table 4

MAB and MBD (W m^{-2}) for the monthly averages of diffuse radiation in Bolzano (2011), Davos (2011) and Payerne (2004–2009) under thin clouds (TC) and overcast (OC) conditions. Only the time interval between 10 a.m. and 2 p.m. was considered in the averaging of cloud mask and irradiance because it was observed that most of the estimation error was concentrated in these hours, which are also those in which most of the irradiance is available.

	MBD [W m^{-2}]		MAD [W m^{-2}]	
	TC	OC	TC	OC
Bolzano	-9	-23	19	24
Davos	2	-14	38	22
Payerne	-21	-24	32	25

in Davos) compared to the satellite estimate (MAB is 83 W m^{-2} in Bolzano and 47 W m^{-2} in Davos). The latter result is significant, because direct irradiance is not sensitive to the effect of multiple scattering and surface albedo, and its inspection allows to better quantify the effect of aerosol absorption and single scattering.

Only four AERONET stations are based in the Alps at Davos, Bolzano, Laegern ($47^\circ.48 \text{ N}$, $8^\circ.35 \text{ E}$, 735 m MSL) and Jungfrau ($46^\circ.55 \text{ N}$, $7^\circ.98 \text{ E}$, 3580 m MSL). Consequently, in order to obtain spatially distributed information on aerosols, we used AOT from MODIS ($10 \text{ km} \times 10 \text{ km}$), SSA from OMI ($0.25^\circ \times 0.25^\circ$) and water vapor total column amount from the ERA Interim reanalysis of the ECMWF ($0.25^\circ \times 0.25^\circ$).

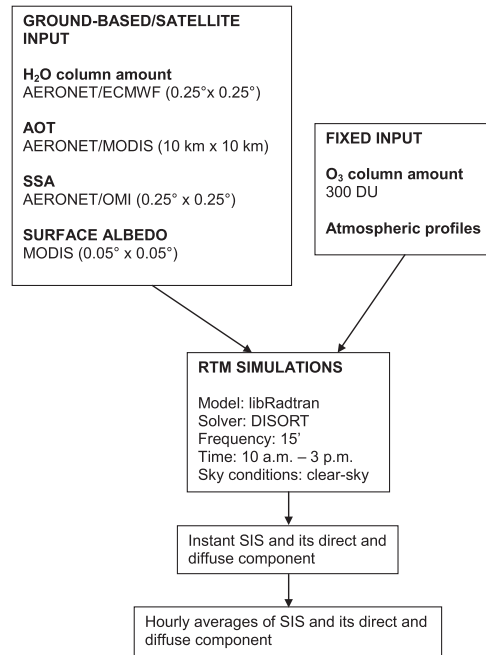


Fig. 6. Summary of the input used for performing RTM simulations in Bolzano and Davos.

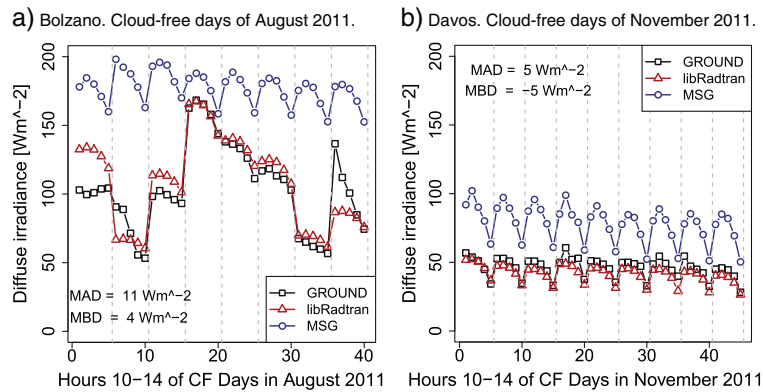


Fig. 7. Hourly averages of RTM simulations, ground measurements, and satellite retrieval of diffuse irradiance in Bolzano and Davos. MAD and MBD refer to the comparison between RTM simulations and ground measurements. Only the hours between 10 a.m. and 2 p.m. were considered. The daily averages of AOT, SSA and water vapor column amount measured by AERONET sun photometers were used as input for RTM simulations. The vertical dashed lines separate the days from each other. On the x axis there is the sequence cloud-free hours (40 for Bolzano, 45 for Davos) for which averages were computed.

In Bolzano we selected the clear-sky days of August 2011 in which MODIS data were available, and run simulations with the same settings as in the previous analysis. Finally we compared the hourly averages of simulated and ground-based data. The MAB of simulated diffuse irradiance against ground data resulted larger (27 W m^{-2}) than the one obtained by using AERONET data. Nevertheless results were much better than for the satellite estimation of diffuse radiation (MAB = 67 W m^{-2}). The same was observed for direct irradiance, in fact a MAB of 45 W m^{-2} was calculated, while for satellite data MAB was equal to 77 W m^{-2} .

These results suggest that an accurate satellite estimate of irradiance components requires at least daily data on the composition and optical properties of the atmosphere.

5. Conclusions

This study examined the performance of the HelioMont algorithm for estimating solar radiation from MSG data in complex terrain. The validation is based on ground-based measurements collected at three alpine sites, namely Bolzano, Davos and Payerne. The first two lie on a valley floor, and both are surrounded by a steep orography. The first is at low altitude, the second at high altitude. The third station is located on the Swiss Main Plateau. We analyzed the performance of the algorithm for different time scales, seasons and sky conditions in order to isolate specific drivers for the major remaining error sources.

The validation demonstrates that the algorithm is able to provide monthly climatologies of both global irradiance and its components over complex terrain. In addition the use of a cloud index based on the SEVIRI high resolution visible channel, as well as its subsequent extension with near-infrared and infrared channels over bright snow surfaces, provides a realistic radiative cloud forcing for the three sites of interest, as already shown by Stöckli (2013). However the estimation of the diffuse and direct components of irradiance on daily and hourly time scale is associated with considerable error. This problem is most prominent under clear-sky conditions, during summer-time, in the central hours of the day. In conclusion, the satellite algorithm overestimates atmospheric diffusivity, which in clear-sky conditions is mainly due to Mie scattering by aerosols and reflection by the Earth surface, and overestimates atmospheric absorption by aerosols and water vapor.

The clear-sky scheme of the satellite algorithm is driven with a monthly $1^\circ \times 1^\circ$ climatology of aerosol distribution in the atmosphere.

This external boundary condition offers a rather inadequate representation, both in spatial and in temporal resolution, of conditions occurring in Alpine valleys. To envisage how the estimation of the irradiance components can be improved, we used daily averages of accurate aerosol and water vapor data, available from the AERONET stations of Bolzano and Davos. For each station we selected the month with the highest number of cloud-free days and simulated the corresponding radiation by the RTM libRadtran, the same used in the satellite algorithm, also considering the sky view factor. Therefore we compared hourly averages of simulated, measured and estimated diffuse and direct irradiance. The low values of MBD and MAB between RTM simulations and ground measurements, compared to the high ones of satellite data, confirmed that model performance would benefit from more accurate local-scale aerosol boundary conditions.

AERONET stations provide very accurate information on aerosols, but are sparsely distributed all over the world. Consequently it is crucial to rely on other sources of data. The easiest choice is using satellite data. This option was tested in Bolzano running RTM simulations using MODIS AOT, OMI SSA and ERA Interim water vapor column amount. MAB duplicated compared to AERONET, but was still much lower than in satellite estimations. It can be concluded that despite having a reliable cloud forcing when deriving solar radiation from satellite data, there is room for improving such estimates by optimizing the prescribed atmospheric state under clear-sky conditions.

One option would be to use daily satellite-based aerosol maps. Known limitations of this method include the high retrieval errors of AOT over land with associated gaps in the dataset over regions with bright surfaces and cloud cover. Specifically non-vegetated mountainous regions with snow cover are often not sufficiently covered by satellite-based aerosol datasets. Nevertheless this choice is promising considering the availability of the new MODIS high resolution (1 km) AOT product obtained with the algorithm MAIAC (Multi-Angle Implementation of Atmospheric Correction) (Emili, Lyapustin, et al., 2011; Lyapustin, Wang, Laszlo, & Korokin, 2012). Another option could be that of integrating satellite and in-situ measurements (Emili, Popp, Wunderle, Zebisch, & Petitta, 2011) in order to reduce the uncertainty in satellite retrieval of AOT. Yet another promising approach are aerosol re-analysis projects like MACC (Inness et al., 2013) and GOCART (Chin, Rood, Lin, Müller, & Thompson, 2000; Chin et al., 2002), which assimilate satellite-based aerosol states, integrate them with known aerosol sources, and project their global distribution by use of atmospheric transport models.

6. Outlook

The proposed integration of surface aerosol measurements with satellite measurements enhances the applicability of satellite data and is more valuable than the analysis of single isolated stations or station networks (Grigante, Mottes, Zardi, & De Franceschi, 2011). The resulting method improves the reliability and precision of solar radiation estimates over complex terrain, which is a key requirement for applications pertaining both to short-term weather forecasting, and to long-term climatological assessment of available radiation.

One example of such an application is the mitigation of one main weakness of technologies based on solar energy, like photovoltaic and concentrated solar power systems, i.e. the fluctuating nature of the solar resource and its poor predictability. An accurate solar radiation estimate is useful for solar energy assessments since it supports decision-making in both the private and public sector, e.g. in building solar atlases, defining suitable plant locations, calculating the return of the investments, and assessing the solar energy potential and the energetic scenario of a region.

Agriculture and forest management are other examples of fields where such valuable information is required. Furthermore in the mountains incoming shortwave radiation is also the main driver of a number of typical atmospheric boundary-layer processes (Rotach & Zardi, 2007), especially in connection with the development of thermally driven winds along the inclines and the valleys (Laiti, Zardi, de Franceschi, & Rampanelli, 2013a,b; Serafini & Zardi, 2010a,b, 2011). The latter are key factors for the assessment of air quality in mountain valleys, where pollutants may arise from the main traffic corridors (de Franceschi & Zardi, 2009), as well as from major plants, such as waste incinerators (Ragazzi, Tirlor, Angelucci, Zardi, & Rada, 2013).

Acknowledgments

This work was partly supported by the EU ERDF (2-1a-97) funded project PV-Initiative and by the Interreg Italy-Switzerland project PV-Alps (27454223). The authors would like to thank EUMETSAT for providing SEVIRI data, MeteoSwiss for providing irradiance data calculated from SEVIRI, and in particular the Principal Investigator and Site Scientists of the BSRN station of Payerne for ensuring the high quality of the data, PMOD/WRC for providing ground-based radiation and for maintaining the AERONET station of Davos, the MODIS and OMI teams for providing aerosol data, and ECMWF for providing reanalysis data. CIMEL calibration was performed at the AERONET-EUROPE calibration center (GOA), supported by ACTRIS (European Union Seventh Framework Program (FP7/2007–2013) under grant agreement no. 262254).

Appendix A. List of acronyms and symbols

α	surface albedo
AERONET	AERosol RObotic NETwork
AOT	Aerosol Optical Thickness
AVHRR	Advanced Very High Resolution Radiometer
BSRN	Baseline Surface Radiation Network
CM-SAF	Satellite Application Facility on Climate Monitoring
ECMWF	European Centre for Medium-range Weather Forecasts
EOS	Earth Observing System
f_s	sky view factor
k	clear-sky index
MAB	Mean Absolute Bias
MBD	Mean Bias Deviation
MODIS	MODerate resolution Imaging Spectroradiometer
MSG	Meteosat Second Generation
n	cloud index
OMI	Ozone Monitoring Instrument
PV	Photovoltaic

RMSE	Root Mean Square Error
R	linear regression coefficient
RTM	Radiative Transfer Model
SEVIRI	Spinning Enhanced Visible and Infrared Imager
SIS	Surface Incoming Shortwave Radiation
SISDIF	Surface Incoming Shortwave Radiation – Diffuse component
SISDNI	Surface Incoming Shortwave Radiation – Direct Normal Irradiance
SPARC	Separation of Pixels using Aggregated Rating over Canada
SSA	Single Scattering Albedo
θ	sun zenith angle
WMO	World Meteorological Organization

References

- Barber, G., Hoertz, P., Lee, S.-H., Abrams, N., Mikulka, J., Mallouk, T., et al. (2011). Utilization of direct and diffuse sunlight in a dye-sensitized solar cell – Silicon photovoltaic hybrid concentrator system. *The Journal of Physical Chemistry Letters*, 2, 581–585.
- Betcke, J., Kühlemann, R., Hammer, A., Drews, A., Lorenz, E., Girodo, M., et al. (2006). Final report of the HELIOSAT-3 project. *Technical report*.
- Beyer, H., Costanzo, C., & Heinemann, D. (1996). Modifications of the Heliosat procedure for irradiance estimates from satellite images. *Solar Energy*, 56, 207–212.
- Bonan, G. B. (2002). *Ecological climatology: Concepts and applications*. Cambridge University Press.
- Cano, D., Monget, J., Albuissou, M., Guillard, H., Regas, N., & Wald, L. (1986). A method for the determination of the global solar radiation from meteorological satellite data. *Solar Energy*, 37, 31–39.
- Carrer, D., Lafont, S., Roujean, J.-L., Calvet, J.-C., Meurey, C., Le Moigne, P., et al. (2012). Incoming solar and infrared radiation derived from METEOSAT: Impact on the modeled land water and energy budget over France. *Journal of Hydrometeorology*, 13, 504–520.
- Chin, M., Ginoux, P., Kinne, S., Torres, O., Holben, B., Duncan, B., et al. (2002). Tropospheric aerosol optical thickness from the GOCART model and comparisons with satellite and sun photometer measurements. *Journal of the Atmospheric Sciences*, 59, 461–483.
- Chin, M., Rood, R., Lin, S.-J., Müller, J.-F., & Thompson, A. (2000). Atmospheric sulfur cycle simulated in the global model GOCART – Model description and global properties. *Journal of Geophysical Research*, 105, 24–671.
- de Franceschi, M., & Zardi, D. (2009). Study of wintertime high pollution episodes during the Brenner-South ALPNAP measurement campaign. *Meteorology and Atmospheric Physics*, 237–250.
- Dee, D., Uppala, S., Simmons, A., Berrisford, P., Poli, P., Kobayashi, S., et al. (2011). The ERA-Interim reanalysis: Configuration and performance of the data assimilation system. *Quarterly Journal of the Royal Meteorological Society*, 137, 553–597.
- Dozier, J., & Marks, D. (1987). Snow mapping and classification from Landsat Thematic Mapper data. *Annals of Glaciology*, 9, 97–103.
- Dubayah, R. (1992). Estimating net solar radiation using Landsat Thematic Mapper and digital elevation data. *Water Resources Research*, 28, 2469–2484.
- Dubayah, R., & Paul, M. (1995). Topographic solar radiation models for GIS. *International Journal of Geographical Information Systems*, 9, 405–419.
- Dür, B., & Zelenka, A. (2009). Deriving surface global irradiance over the alpine region from Meteosat Second Generation data by supplementing the HELIOSAT method. *International Journal of Remote Sensing*, 30, 5821–5841.
- Dür, B., Zelenka, A., Müller, R., & Philipona, R. (2010). Verification of CM-SAF and MeteoSwiss satellite based retrievals of surface shortwave irradiance over the Alpine region. *International Journal of Remote Sensing*, 31, 4179–4198.
- EHF, UIB, & ARMINES (2003). Report of the Heliosat-3 software package for solar irradiance retrieval, all sky working version. Deliverable D8.1 and D8.2. *Technical report*.
- Emili, E., Lyapustin, A., Wang, Y., Popp, C., Korkin, S., Zebisch, M., et al. (2011). High spatial resolution aerosol retrieval with MAIAC: Application to mountain regions. *Journal of Geophysical Research*, 116. <http://dx.doi.org/10.1029/2011JD016297>.
- Emili, E., Popp, C., Wunderle, S., Zebisch, M., & Petitta, M. (2011). Mapping particulate matter in alpine regions with satellite and ground-based measurements: An exploratory study for data assimilation. *Atmospheric Environment*, 45, 4344–4353. <http://dx.doi.org/10.1016/j.atmosenv.2011.05.051>.
- Fontana, F., Stöckli, R., & Wunderle, S. (2010). SPARC: A new scene identification algorithm for MSG SEVIRI. Report on modifications and validation. Visiting scientist report. EUMETSAT satellite application facility on climate monitoring.
- Fontoyont, M., Dumortier, D., Hammer, A., Olseth, J., Skartveit, A., Ineichen, P., et al. (1997). SATELLIGHT—Processing of METEOSAT data for the production of high quality daylight and solar radiation available on a world wide web internet server. Mid-term progress report, jor3-ct90041 SoDa-5-2-4. CNRS-ENTPE.
- Fontoyont, M., Dumortier, D., Heinemann, D., Hammer, A., Olseth, J., Skartveit, A., et al. (1998). SATELLIGHT – A www server which provides high quality daylight and solar radiation data for western and central Europe. *Proc. 9th Conference on Satellite Meteorology and Oceanography, Paris, France* (pp. 434–437).
- Giovannini, L., Zardi, D., & de Franceschi, M. (2011). Analysis of the urban thermal fingerprint of the city of Trento in the Alps. *Journal of Applied Meteorology and Climatology*, 50, 1145–1162.

- Giovannini, L., Zardi, D., & de Franceschi, M. (2013). Characterization of the thermal structure inside an urban canyon: Field measurements and validation of a simple model. *Journal of Applied Meteorology and Climatology*, 52, 64–81.
- Giovannini, L., Zardi, D., de Franceschi, M., & Chen, F. (2014). Numerical simulations of boundary-layer processes and urban-induced alterations in an Alpine valley. *International Journal of Climatology*, 34, 1111–1131. <http://dx.doi.org/10.1002/joc.375>.
- Grigante, M., Mottes, F., Zardi, D., & De Franceschi, M. (2011). Experimental solar radiation measurements and their effectiveness in setting up a real-sky irradiance model. *Renewable Energy*, 36, 1–8.
- Hammer, A., Heinemann, D., Hoyer, C., Kuhlmann, R., Lorenz, E., Müller, R., et al. (2003). Solar energy assessment using remote sensing technologies. *Remote Sensing of Environment*, 86, 423–432.
- Holben, B., Eck, T., Slutsker, I., Tanre, D., Buis, J., Setzer, A., et al. (1998). AERONET — A federated instrument network and data archive for aerosol characterization. *Remote Sensing of Environment*, 66, 1–16.
- Ineichen, P. (2006). Comparison of eight clear sky broadband models against 16 independent data banks. *Solar Energy*, 80, 468–478.
- Ineichen, P., Barroso, C., Geiger, B., Hollmann, R., Marsouin, A., & Mueller, R. (2009). Satellite application facilities irradiance products: Hourly time step comparison and validation over Europe. *International Journal of Remote Sensing*, 30, 5549–5571.
- Inness, A., Baier, F., Benedetti, A., Bouarar, I., Chabrilat, S., Clark, H., et al. (2013). The MACC reanalysis: An 8 yr data set of atmospheric composition. *Atmospheric Chemistry and Physics*, 13, 4073–4109.
- Journée, M., & Bertrand, C. (2010). Improving the spatio-temporal distribution of surface solar radiation data by merging ground and satellite measurements. *Remote Sensing of Environment*, 114, 2692–2704.
- Kasten, F., Dehne, K., Behr, H., & Bergholter, D. (1984). Spatial and temporal distribution of diffuse and direct solar radiation in Germany. *Research report N. 84*. German Federal Ministry of Research and Technology.
- Kato, S., Ackerman, T., Mather, J., & Clothiaux, E. (1999). The k-distribution method and correlated-k approximation for a shortwave radiative transfer model. *Journal of Quantitative Spectroscopy and Radiative Transfer*, 62, 109–121.
- Khlopenkov, K., & Trishchenko, A. (2007). SPARC: New cloud, snow, and cloud shadow detection scheme for historical 1-km AVHRR data over Canada. *Journal of Atmospheric and Oceanic Technology*, 24, 322–343.
- Kinne, S. (2009). *Clouds in the perturbed climate system. Chapter climatologies of cloud related aerosols. Part 1: Particle number and size*. Cambridge, Mass: MIT Press.
- Laiti, L., Zardi, D., de Franceschi, M., & Rampanelli, G. (2013a). Atmospheric boundary layer structures associated with the Ora del Garda wind in the Alps as revealed from airborne and surface measurements. *Atmospheric Research*, 132–133, 473–489. <http://dx.doi.org/10.1016/j.atmosres.2013.07.00> (URL: <http://www.sciencedirect.com/science/article/pii/S016980951300197X>).
- Laiti, L., Zardi, D., de Franceschi, M., & Rampanelli, G. (2013b). Residual kriging analysis of airborne measurements: Application to the mapping of atmospheric boundary-layer thermal structures in a mountain valley. *Atmospheric Science Letters*, 2013, 79–85.
- Lee, W., Liou, K., & Hall, A. (2011). Parameterization of solar fluxes over mountain surfaces for application to climate models. *Journal of Geophysical Research*, 116. <http://dx.doi.org/10.1029/2010JD014722>.
- Levy, R., Remer, L., Mattoo, S., Vermote, E., & Kaufman, Y. (2007). Second-generation operational algorithm: Retrieval of aerosol properties over land from inversion of moderate resolution imaging spectroradiometer spectral reflectance. *Journal of Geophysical Research*, 112. <http://dx.doi.org/10.1029/2006JD007811>.
- Liou, K. (2002). *An introduction to atmospheric radiation, Vol. 84*. Academic Press.
- Lyapustin, A., Wang, Y., Laszlo, I., & Korkin, S. (2012). Improved cloud and snow screening in MAIAC aerosol retrievals using spectral and spatial analysis. *Atmospheric Measurement Techniques*, 5, 843–850.
- Mayer, B., & Kylling, A. (2005). Technical note: The libRadtran software package for radiative transfer calculations: Description and examples of use. *Atmospheric Chemistry and Physics*, 5, 1855–1877.
- Müller, R., Dagestad, K., Ineichen, P., Schroedter-Homscheidt, M., Cros, S., Dumortier, D., et al. (2004). Rethinking satellite-based solar irradiance modelling: The SOLIS clear-sky module. *Remote Sensing of Environment*, 91, 160–174.
- Müller, R., Matsoukas, C., Gratzki, A., Behr, H., & Hollmann, R. (2009). The CM-SAF operational scheme for the satellite based retrieval of solar surface irradiance—A LUT based eigenvector hybrid approach. *Remote Sensing of Environment*, 113, 1012–1024.
- Ragazzi, M., Tirlir, W., Angelucci, G., Zardi, D., & Rada, E. (2013). Management of atmospheric pollutants from waste incineration processes: The case of Bozen. *Waste Management & Research*, 31, 235–240.
- Remund, J., Wald, L., Lefvre, M., Ranchin, T., & Page, J. (2003). Worldwide Linke turbidity information. *Proceedings of ISES Solar World Congress 2003, Vol. 400*.
- Rigollier, C., Lefèvre, M., & Wald, L. (2004). The method Heliosat-2 for deriving shortwave solar radiation from satellite images. *Solar Energy*, 77, 159–169.
- Rotach, M., & Zardi, D. (2007). On the boundary-layer structure over highly complex terrain: Key findings from MAP. *Quarterly Journal of the Royal Meteorological Society*, 133, 937–948.
- Sellers, P., Dickinson, R., Randall, D., Betts, A., Hall, F., Berry, J., et al. (1997). Modeling the exchanges of energy, water, and carbon between continents and the atmosphere. *Science*, 275, 502–509.
- Sellers, P., Randall, D., Collatz, G., Berry, J., Field, C., Dazlich, D., et al. (1996). A revised land surface parameterization (SiB2) for atmospheric GCMs. Part I: Model formulation. *Journal of Climate*, 9, 676–705.
- Serafin, S., & Zardi, D. (2010a). Daytime heat transfer processes related to slope flows and turbulent convection in an idealized mountain valley. *Journal of Atmospheric Science*, 3739–3756.
- Serafin, S., & Zardi, D. (2010b). Structure of the atmospheric boundary layer in the vicinity of a developing upslope flow system: A numerical model study. *Journal of Atmospheric Science*, 1171–1185.
- Serafin, S., & Zardi, D. (2011). Daytime development of the boundary layer over a plain and in a valley under fair weather conditions: A comparison by means of idealized numerical simulations. *Journal of Atmospheric Science*, 2128–2141.
- Stamnes, K., Tsay, S., Jayaweera, K., Wiscombe, W., et al. (1988). Numerically stable algorithm for discrete-ordinate-method radiative transfer in multiple scattering and emitting layered media. *Applied Optics*, 27, 2502–2509.
- Stamnes, K., Tsay, S., Wiscombe, W., & Laszlo, I. (2000). *DISORT, a general-purpose Fortran program for discrete-ordinate-method radiative transfer in scattering and emitting layered media: Documentation of methodology*. Goddard Space Flight Center, NASA.
- Stöckli, R. (2013). The HelioMont surface radiation processing. *Scientific report MeteoSwiss*, 93. MeteoSwiss: Federal Office of Meteorology and Climatology (119 pp.).
- Wilks, D. S. (2011). *Statistical methods in the atmospheric sciences volume 91 in the International Geophysics Series*. Academic Press.
- World Meteorological Organization, W. M. O. (2008). *Guide to meteorological instruments and methods of observation. N. 8* (7th ed.). World Meteorological Organization.

6.4 Publication IV

Solar spectral characterization of three different locations at Alpine latitudes using Average Photon Energy

Giorgio Belluardo, Marcus Rennhofer, Philipp Weihs, Mauro Pravettoni, Davide
Strepparava, Mark Olefs, Dietmar Baumgartner, David Moser

*Proceedings of the International Conference on Solar Energy and Buildings (EUROSUN).
Aix-les-Bains, France, 2014*

Solar Spectral Characterization of Three Different Locations at Alpine Latitudes Using Average Photon Energy

Giorgio Belluardo^{1,2,3}, Marcus Rennhofer², Philipp Weihs³, Mauro Pravettoni⁴, Davide Strepparava⁴, Marc Olefs⁵, Dietmar Baumgartner⁶ and David Moser¹

¹ EURAC Research - Institute for Renewable Energy, Bolzano (Italy)

² AIT Austrian Institute of Technology GmbH - Energy Department, Vienna (Austria)

³ University of Natural Resources and Life Sciences - Institute for Meteorology, Vienna (Austria)

⁴ University of Applied Sciences and Arts of Southern Switzerland - Department of Environment Construction and Design, Canobbio (Switzerland)

⁵ Central Institute for Meteorology and Geodynamics, Vienna (Austria)

⁶ University of Graz - Kanzelhöhe Observatory for Solar and Environmental Research, Treffen (Austria)

Abstract

The characteristic of the solar spectrum is one of the most important factors to be taken into account when evaluating the solar resource of a certain area, for photovoltaic applications. In fact, the spectral distribution of irradiance, coupled with the spectral responsivity of photovoltaic modules, is responsible for the effective performance of a photovoltaic system in real outdoor conditions. This paper investigates the variability of solar spectrum at three different locations at Alpine latitudes: Vienna (Austria), Kanzelhöhe (Austria) and Lugano (Switzerland). The Average Photon Energy (APE) index is used to quantify the spectral distribution. It is derived from outdoor measurements and computed for the range 350-900 nm. The diurnal and seasonal variability of APE is assessed under real conditions of cloudiness as well as under clear sky conditions. The results are interpreted considering the atmospheric properties of the investigated sites, and an example of assessment of how much the spectral variability influences the performance in generated current of photovoltaic modules is shown.

Keywords: solar spectrum, spectral effect, average photon energy, photovoltaic, spectral responsivity, spectral simulation

1. Introduction

Several studies (Gottschalg et al., 2005; Minemoto et al., 2009) have investigated the role of spectral variability on the performance of different photovoltaic (PV) technologies. Results demonstrate that the selection of the optimal PV material should also depend upon the spectral peculiarity of the installation site. The purpose of this work is to characterize and compare three locations at Alpine latitudes: Kanzelhöhe, Vienna and Lugano, with different altitudes and climatic conditions from the point of view of the solar spectrum variability. This is a first step towards an exhaustive comparison of the performance of different PV technologies with respect to the spectral distribution of the incoming irradiance at those sites.

In the last years an increasing number of sites in the world have been equipped with spectroradiometers thanks to decreasing costs and increasing accuracy of these instruments. To the authors' knowledge many studies exist that investigate the spectrum at specific locations (Cornaro and Andreotti, 2012; Gottschalg et al., 2003), but very few compare measurements at different sites, especially in Europe. Furthermore, a comparison of results from different studies is difficult, since a) different indexes (Average Photon Energy, Average Wavelength, Useful Fraction, Spectral Mismatch Correction, etc.) are used, b) the investigated spectra span

different wavelength ranges, or c) refer to different tilt angles of the plane of sensor installation.

2. Experimental setup

The three locations under investigation are equipped with spectroradiometers acquiring spectra with a frequency of one minute. The information concerning the sites and instrumentation is reported in Table 1.

Tab. 1: Characteristics of the investigated sites and related spectroradiometers

Location	Kanzelhöhe	Vienna	Lugano
Coordinates	46.678 N 13.902 E	48.269 N 16.427 E	46.026 N 8.961 E
Altitude (m a.s.l.)	1526	170	214
Spectroradiometer owner	University of Natural Resources and Life Sciences (BoKu)	Austrian Institute of Technology (AIT)	University of Applied Sciences and Arts of Southern Switzerland (SUPSI)
Spectroradiometer model	EKO MS-710	Ocean Optics HR2000A	EKO MS-710, MS-712
Wavelength (nm)	300-1100	300-1100	300-1700
Tilt	0°	0°	45°
Azimuth	-	-	173°
Number of months of available data	27	35	14

The database available from each site cover different time periods, ranging on the whole from July 2010 to December 2013, for a total of 76 months of spectral data.

In addition to spectral information, diffuse and global horizontal broadband irradiance is measured next to or in proximity of the spectroradiometers.

3. Methodology

3.1. Average photon energy

The APE is used in this study as the index to uniquely quantify the spectrum characteristics (Minemoto et al., 2009), i.e. the extent to which the spectral distribution is spread towards lower rather than higher wavelengths. According to Gottschalg et al. (2005), APE is defined as the average energy of the photons within the spectrum, as in the following equation:

$$APE = \frac{\int E(\lambda)d\lambda}{q \int \Phi(\lambda)d\lambda}$$

(eq. 1)

where q is the electronic charge, E the spectral irradiance and Φ the photon spectral flux density. High values of APE stand for a spectral distribution shifted towards lower wavelengths (blue shift), while low values of APE stand for a spectral distribution shifted towards higher wavelengths (red shift).

In this study, APE for the three sites is calculated in the range 350-900 nm in order to make the spectral information comparable between sites and to filter out possible noise in proximity of the spectroradiometer measurement window limits. Furthermore, data of diffuse and global horizontal irradiance are available for the calculation of the diffuse fraction (ratio of diffuse and global irradiance) in order to classify cloudiness in a specific time span.

3.2. Spectral simulation

In order to compare spectra measured on different planes and azimuth (0° tilt for Kanzelhöhe and Vienna, 45°

tilt and 173° azimuth for Lugano), a simulation of the spectra is needed. A simple translation of the measured spectral information from the horizontal to the tilted plane is in fact not possible in this case, since no spectral data of the direct or diffuse component are available.

The simulation of global, direct and diffuse spectral irradiance at a specific location and time is performed using the *uvspec* model, implemented within the library *libRadtran* (Mayer and Kylling, 2005). More specifically, the discrete ordinates radiative transfer (DISORT) code (Stamnes et. al, 1988) has been selected as radiative transfer solver. The most influencing atmospheric properties, such as aerosol optical thickness at different wavelengths, ozone column and precipitable water, are retrieved from aeronet network (NASA, 2014), when available. If this is not the case, data of atmospheric composition are retrieved from the MACC (Monitoring Atmospheric Composition and Climate, 2014) project. Transposition models (Padovan and Del Col, 2010) are then applied to translate the simulated spectral information of Kanzelhöhe and Vienna to the tilted plane as in Lugano. The sky model applied in this study assumes an isotropic distribution of diffuse irradiance (Liu and Jordan, 1963).

3.3. Photovoltaic performance assessment

In order to assess the influence of the solar spectrum on the performance of a generic PV device, the short circuit current (I_{sc}) is calculated using the following equation (Gottschalg et al., 2005):

$$I_{sc} = A \int SR(\lambda)G(\lambda)d\lambda$$

(eq. 2)

where A is the device area, SR is the spectral responsivity of the photovoltaic technology and G is the spectral irradiance.

4. Results and discussion

4.1. Spectral simulation and data verification

One winter and one summer clear sky days have been selected for each investigated location in order to perform a simulation of the solar spectrum with a frequency of one hour. The APE index has been therefore derived for each time step, and compared to the corresponding measured value. Figure 1 reports the simulated and measured values of APE for Kanzelhöhe (horizontal plane), Vienna (horizontal plane), and Lugano (45° tilted plane).

Information from aeronet network, which is considered the most reliable source since it derives from ground measurements, was available only in Kanzelhöhe for the winter day. In the case of Kanzelhöhe summer day, Lugano summer day and Vienna, atmospheric properties were derived from MACC project. Finally, neither aeronet nor MACC data were available for the winter day in Lugano.

It is evident that in the case of Kanzelhöhe the simulated values show a good agreement with the measurements, as well as in the case of the summer day in Lugano. As for Vienna, the strong discrepancies between simulated and measured values is due to a possible underestimation of the irradiances at VIS red and NIR wavelengths, occurring in the measurement process. Figure 2 shows a comparison of measured and simulated spectrum at 12 GMT of the considered summer day. Also AM1.5 standard spectrum is added as reference. It is evident that the spectral irradiance distribution at higher wavelengths (from around 750 nm) does not assume the characteristic shape, which is also visible in the AM1.5 standard spectrum. Another discrepancy seems to occur in the range 450-500 nm. This problem, which occurs in all spectra related to the two selected days, might be caused by a damping in the signal transmission through the optical fibre, and will be further investigated.

Also the simulated values of APE for the winter day in Lugano, based on default values of atmospheric properties, does not agree with the daily profile of measured APE. This fact confirms once more the validity of the spectral simulation methodology used in the other cases and the need for reliable sources of data describing the atmosphere composition.

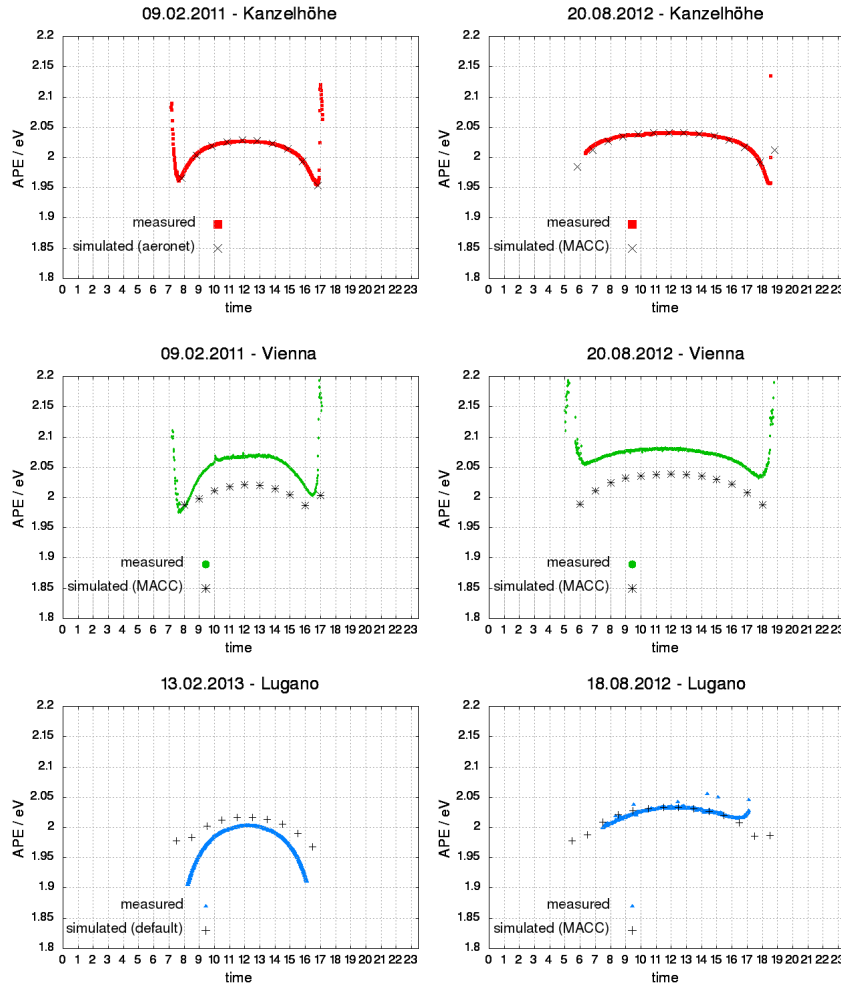


Fig. 1: Simulated and measured APE during a winter (left) and summer (right) clear sky day in the three investigated locations.

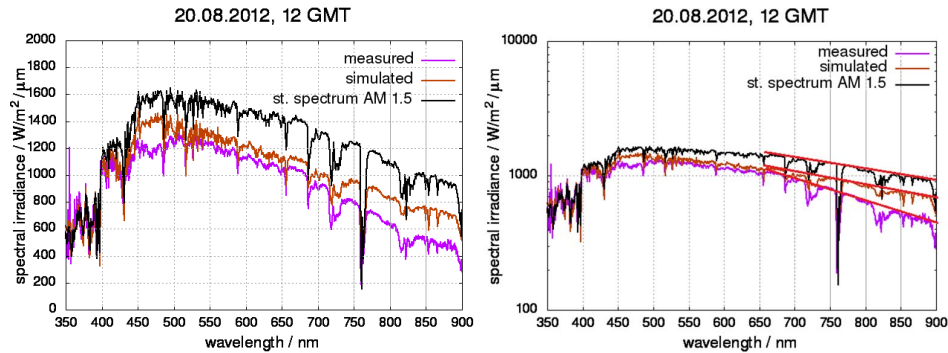


Fig. 2: Comparison of simulated and measured spectrum for a summer clear sky day in Vienna, in normal (left) and logarithmic (right) scale. AM 1.5 standard spectrum is also reported.

4.2. Daily APE profiles on the horizontal plane

As seen, the measurements of solar spectrum in Vienna seem to be affected by a systematic lowering of the spectral irradiance at VIS red and NIR wavelengths. On the other hand, the same methodology to simulate the solar spectrum in Vienna fits well the experimental measurements of Kanzelhöhe and, when reliable values of atmospheric properties are available, Lugano. It is therefore reasonable to focus only on the simulated values of APE in order to carry out a comparison between the locations of Vienna and Kanzelhöhe, on the horizontal plane.

Figure 3 reports the daily profiles of APE, of the relative difference in APE between the investigated sites, of the Aerosol Optical Depth (AOD) at 550 nm, of precipitable water, and of solar zenith angle. It is evident that in general the APE is lower in winter than in summer in both locations, i.e. the spectrum is more red-shifted. This is confirmed by several studies which analyze measured spectra at Northern sphere latitudes (Cornaro and Andreotti, 2013; Gottschalg et al., 2003; Schweiger et al., 2012; Ishii et al., 2013), and seems to be related to higher levels of precipitable water occurring during summer at those latitudes (Ortiz de Galisteo et al., 2013), as corroborated by the daily profiles measured at the two investigated locations.

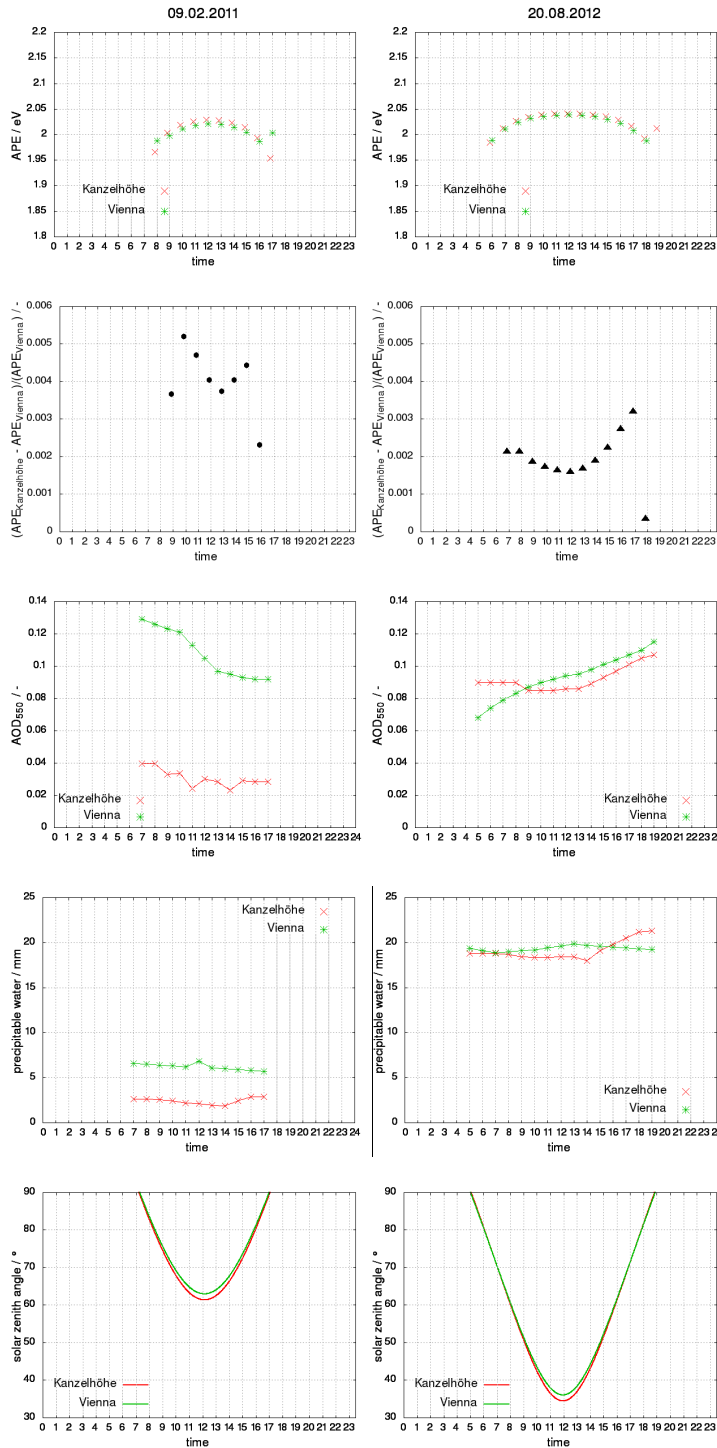


Fig. 3: From top to bottom. Simulated daily profiles of APE, relative difference of APE with respect to Vienna, aerosol optical depth, precipitable water and solar zenith angle for a winter (left) and summer (right) clear sky day.

In both seasons the solar spectrum in Kanzelhöhe results more blue shifted than in Vienna. This divergence is more evident in winter (0.45% difference in APE on average) than in summer (0.2% in APE on average). Focusing on the winter day, and looking at the related AOD, it is possible to explain this fact with a considerable difference in aerosol levels between the two locations registered on that day. In fact, as Behrendt et al. (2013) report, increasing values of AOD result in a gradual shift towards red wavelengths of the solar spectrum, i.e. lower values of APE.

Finally, the variability of APE differences between Kanzelhöhe and Vienna, which assumes a symmetric-like profile with a minimum value around noon, can be explained by the difference in the values of solar zenith angle (i.e. of irradiance incidence angle on the considered plane, in the horizontal case), which is minimum at noon.

It is therefore clear that an exhaustive analysis of spectral variability must take into account not only the geometric differences in the solar position, but also a complete characterization of the variability of aerosol and water vapor content of the atmosphere.

4.3. Daily APE profiles on the tilted plane

It is interesting to assess the characteristic of solar spectrum on a tilted plane, since photovoltaic modules are very often mounted on inclined surfaces to optimize the energy production. Figure 4 shows the daily profile of APE on a 45° tilt plane for the investigated winter and summer clear sky days. A comparison is possible in this case with the APE derived from solar spectrum measurements in Lugano.

The spread between Kanzelhöhe and Vienna APE detected for the horizontal plane case is still evident here, still more pronounced in winter than in summer. With respect to the horizontal case, the profile looks more pronounced, i.e. there is a higher variability during the day. In particular, Lugano shows a good agreement with the APE profiles of Kanzelhöhe.

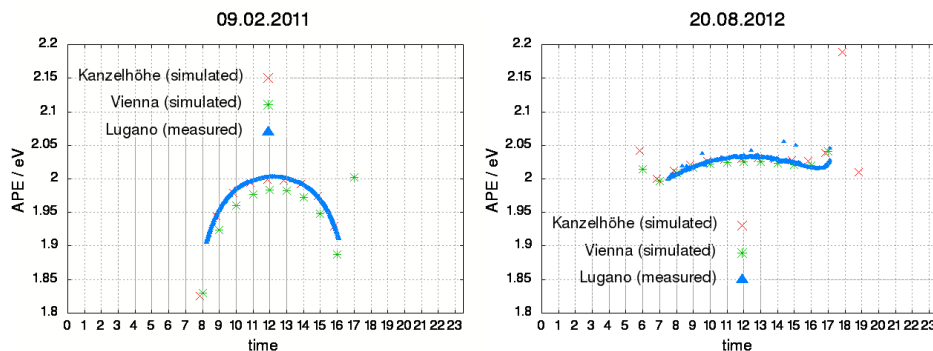


Fig. 4: Simulated daily profiles of APE in Vienna and Kanzelhöhe, for a winter (left) and summer (right) clear sky day, on the tilted (45° plane), and comparison with values measured in Lugano.

4.4. Seasonal variability of APE

The seasonal variability of APE index can be assessed by calculating daily or monthly values of APE as an average weighted on the broadband irradiance, i.e. on the integral value of the spectral irradiance. Figure 5 shows the variability of daily values of APE in a 42-months range, from July 2010 to December 2013, as well as a zoom from July 2012 only of points calculated during clear sky days. The values of APE in Vienna are likely to be affected by damping of the signal transmission and should not therefore be taken into consideration, as already discussed in section 4.1. Another problem affects the APE values of Vienna between July 2011 to March 2012, when they suddenly drop for more than 10% to a stable value around 1.85 eV. This malfunctioning is actually due to a damage occurred to the quartz dome, which broke leaving the sensor at open air and to the aging of the diffuser material.

Focusing on Kanzelhöhe and Lugano, it is possible to see a certain degree of seasonal variability. In general, APE is lower in winter than in summer, thus confirming the results of the analysis of daily profiles. In particular, this seasonal variability seems more pronounced with tilted angles as in Lugano (4% of relative difference in APE with respect to the summer values), rather than on the horizontal plane (1.2% for

Kanzelhöhe). This is a noteworthy fact, since it infers that PV plants installed on tilted planes are more prone to performance variability due to spectral effects than the horizontal case.

Finally, the values of APE on the tilted plane tend to diverge more from those on the horizontal plane when close to winter.

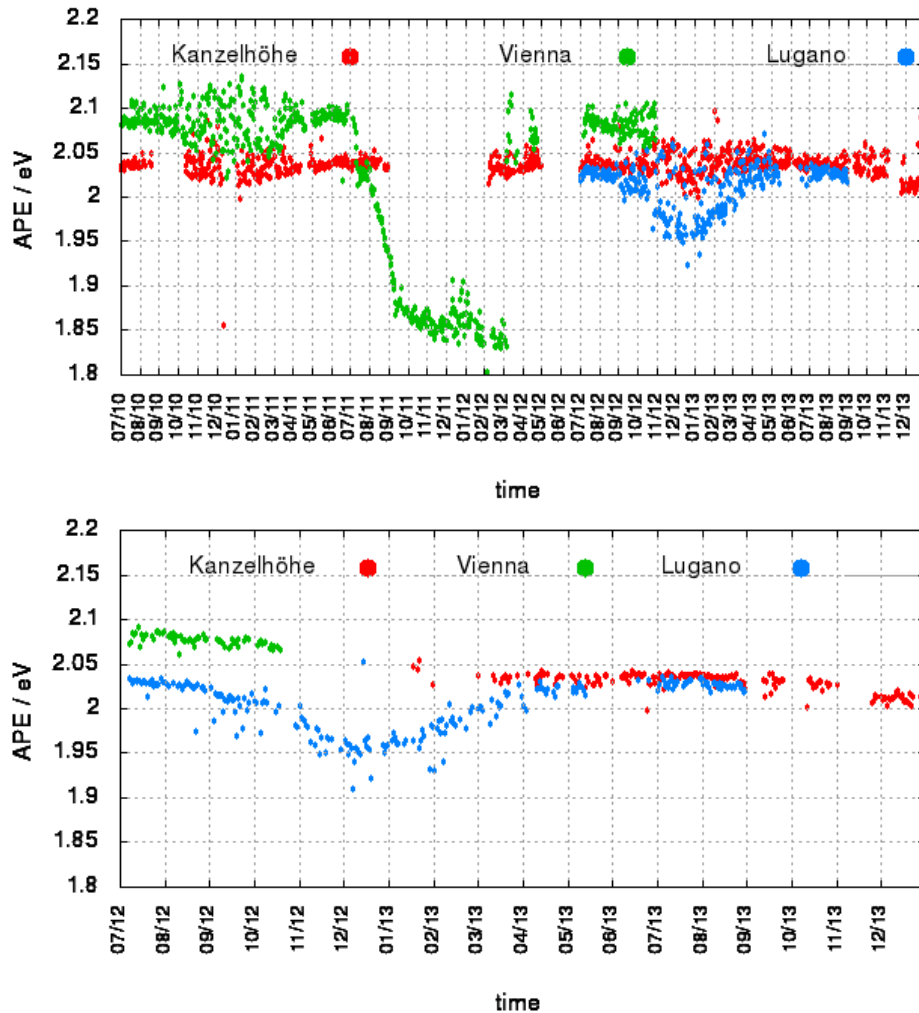


Fig. 5: Seasonal profiles of daily average APE for the three sites under investigation: a) real conditions of cloudiness, b) clear sky conditions (from July 2012)

4.5. Spectral effect on module performance

In order to evaluate to which extent the difference of solar spectrum in different locations affects the performance of a PV device, the same winter and summer clear sky days have been taken into consideration. A generic polycrystalline-silicon module, whose spectral responsivity is known, has been considered to calculate the short circuit current using equation 2. Figure 6 shows the relative difference in I_{sc} between the same module as it was installed in Vienna and in Kanzelhöhe. The simulated spectra have been previously normalized in order to make spectra with different broadband irradiance comparable.

The more red-shifted spectra (lower APE) seen in Vienna for both days result in a higher performance of the considered PV device in this location, in terms of I_{sc} . This is due to the increasing responsivity of polycrystalline silicon modules when moving from the VIS to the near-IR region. For example, around noon in a winter day the module installed in Vienna produces 0.6% more current than in Kanzelhöhe, while in summer almost 0.3% more. It has to be pointed out that a higher performance in terms of I_{sc} does not necessarily mean a higher performance in terms of energy production, since the module voltage is strongly dependent on the ambient temperature.

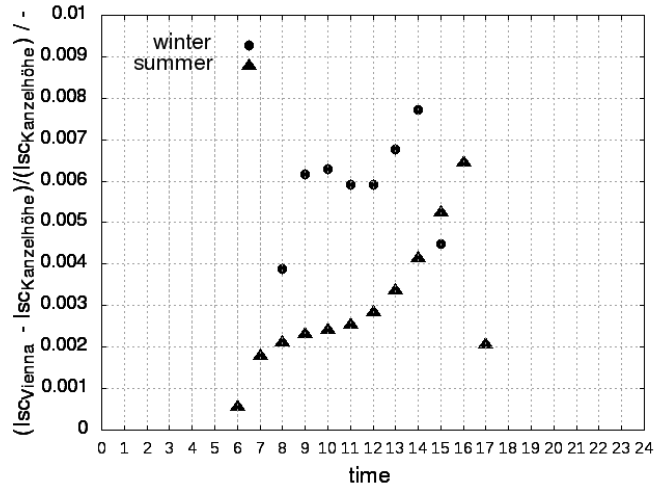


Fig. 6: Relative difference of I_{sc} of a polycrystalline silicon module installed in Vienna and Kanzelhöhe, for a winter and summer clear sky day.

5. Conclusions

Spectral irradiance measurements from three different sites and two different tilt angles have been collected for more than three years to assess the variability of solar spectrum at those locations. The study has been carried out using the APE index computed in the range 350-900 nm.

The analysis of data confirms a seasonal oscillation of solar spectrum towards more blue-rich contents in summer, and more red-rich contents in winter. This seasonal oscillation is more evident on tilted planes (4% in APE registered in Lugano on a 45° tilted plane). The relative difference of solar spectra between horizontal and tilted surfaces presents a minimum during summer and a maximum during winter.

The spectral characterization of a location strongly depends on its atmospheric characteristics, and especially on aerosol and precipitable water content. Furthermore also ground albedo, which depends on azimuth and tilt angle of the plane, and the azimuthal ground view factor of the location play an important role, especially for tilted planes. A deeper study of the variability of those factors in the considered locations is therefore worthy.

Results show that depending upon the photovoltaic technology and its responsivity to solar irradiance, the effect of the sole solar spectrum on its performance in generated current between different locations is not negligible (up to 0.8% between the locations of Vienna and Kanzelhöhe for a generic winter clear sky day and for a polycrystalline silicon PV device). This confirms once more the importance that the selection of the optimal PV material should also take into consideration the spectral peculiarity of the installation site. A more extensive study on the overall effect of spectral variability on the investigated sites will be object of a future study involving more photovoltaic technologies.

Simulations of solar spectrum carried out with DISORT radiative transfer equation solver and atmospheric input parameters from aeronet network or MACC project demonstrates the usefulness of this methodology in reconstructing solar spectral information, when measurements are missing, or in validating available on-site measurements to detect possible malfunctioning issues. The use of default or low temporal resolution (order of month) input values for atmospheric properties should be avoided.

6. Acknowledgements

The authors wish to acknowledge the European Regional Development Fund (ERDF) and the Stiftung Südtiroler Sparkasse for co-financing the project 2-1a-97 "PV Initiative".

7. References

- Behrendt, T., Kuehnert, J., Hammer, A., Lorenz, E., Betcke, J., Heinemann, D., 2013. Solar spectral irradiance derived from satellite data: a tool to improve thin film PV performance estimations?. *Solar Energy* 98, 100-110.
- Cornaro, C., Andreotti, A., 2012. Influence of average photon energy index on solar irradiance characteristics and outdoor performance of photovoltaic modules. *Prog. Photovolt: Res. Appl.* 21, 996-1003.
- Gottschalg, R., Infield, D.G., Kearney, M.J., 2003. Experimental study of variations of the solar spectrum of relevance to thin film solar cells. *Sol. Energ. Mat. Sol. Cells* 79, 527-537.
- Gottschalg, R., Betts, T.R., Infield, D.G., Kearney, M.J., 2005. The effect of spectral variations on the performance parameters of single and double junction amorphous silicon solar cells. *Sol. Energ. Mat. Sol. Cells* 85, 415-428.
- Ishii, T., Otani, K., Takashima, T., Xue, Y., 2013. Solar spectral influence on the performance of photovoltaic (PV) modules under fine weather and cloudy weather conditions. *Prog. Photovolt: Res. Appl.* 21, 481-489.
- Liu, B.Y.H., Jordan, R.C., 1963. The long-term average performance of flat-plate solar energy collectors. *Solar Energy* 7, 53-74.
- Mayer, B., Kylling, A., 2005. Technical note: the libRadtran software package for radiative transfer calculations – description and examples of use. *Atmos. Chem. Phys.* 5, 1855-1877.
- Minemoto, T., Nakada, Y., Takahashi, H., Takakura, H., 2009. Uniqueness verification of solar spectrum index of average photon energy for evaluating outdoor performance of photovoltaic devices. *Solar Energy* 83, 1294-1299.
- Monitoring Atmospheric Composition and Climate (MACC) [Online]. Available at <http://aeronet.gsfc.nasa.gov/> [Accessed: 04-Aug-2014].
- NASA: Aerosol Robotic Network (AERONET) [Online]. Available at <http://aeronet.gsfc.nasa.gov/> [Accessed: 04-Aug-2014].
- Ortiz de Galisteo, J.P., Bennouna, Y., Toledano, C., Cachorro, V., Romero, P., Andrés, M.I., Torres, B., 2013. Analysis of the annual cycle of the precipitable water vapour over Spain from 10-year homogenized series of GPS data. *Q. J. Roy. Meteor. Soc.* 140, 397-406.
- Padovan, A., Del Col, D., 2010. Measurement and modelling of solar irradiance component on horizontal and tilted planes. *Solar Energy* 84, 2068-2084.
- Schweiger, M., Ulrich, M., Nixdorf, I., Rimmelspacher L., Jahn, U., Herrmann, W., 2012. Spectral analysis of various thin-film modules using high precision spectral response data and solar spectral irradiance data. *Proc. 27th European Solar Energy Conference and Exhibition*, 3284-3290.
- Stamnes, K., Tsay, S.C., Wiscombe, W., Jayaweera, K., 1988. Numerically stable algorithm for discrete-ordinate-method radiative transfer in multiple scattering and emitting layered media. *Applied Optics* 27, 2502-2509.

6.5 Publication V

Uncertainty analysis of a radiative transfer model using Monte Carlo method within 280-2500 nm region

Giorgio Belluardo, Grazia Barchi, Dietmar Baumgartner, Marcus Rennhofer, Philipp
Weihs, David Moser

Solar Energy 132, 558-569



Uncertainty analysis of a radiative transfer model using Monte Carlo method within 280–2500 nm region

Giorgio Belluardo^{a,d,*}, Grazia Barchi^a, Dietmar Baumgartner^b, Marcus Rennhofer^c, Philipp Weihs^d, David Moser^a

^a Institute for Renewable Energy, EURAC Research, Viale Druso 1, 39100 Bolzano, Italy

^b Kanzelhöhe Observatory for Solar and Environmental Research, University of Graz, Kanzelhöhe 19, 9521 Treffen am Ossiacher See, Austria

^c Energy Department, AIT Austrian Institute of Technology GmbH, Giefinggasse 2, 1210 Vienna, Austria

^d Institute of Meteorology, University of Natural Resources and Life Sciences, Peter-Jordan-Straße 82, 1190 Vienna, Austria

Received 13 October 2015; received in revised form 23 February 2016; accepted 25 March 2016

Communicated by: Associate Editor David Renne

Abstract

Radiative transfer models (RTM) are used to calculate spectral and broadband irradiance, given a set of input parameters that are representative of the atmospheric state. While many studies exist on their accuracy, there is still a research gap in the assessment of their uncertainty, due to the nonlinear and not differentiable nature of the Radiative Transfer Equation, which is the core of a RTM. This study evaluates the uncertainty of both spectral and broadband irradiance calculated with the radiative transfer model SDISORT implemented in the tool UVSPEC within the range 280–2500 nm. A set of input values representing the atmospheric state at Kanzelhöhe Observatory (Austria) site at 10:00 on April 25th, 2013 is taken as reference and a Monte Carlo technique is used to propagate the uncertainty of input parameters to the model output. Both the effects of single input parameter uncertainty and of their combination are evaluated, as well as the influence of the deviation of input values from the reference set. Results show that ozone column is an important source of uncertainty in the UV-B region, while the uncertainties of Ångström aerosol turbidity coefficient and extraterrestrial spectrum affect the whole spectral range. Considering a reasonable variability range for all involved input parameters, the overall uncertainty of broadband global horizontal irradiance is between 2.9% and 5.9%. These values are higher, but still comparable, to typical uncertainty values of outdoor-deployed spectroradiometers.

© 2016 Elsevier Ltd. All rights reserved.

Keywords: Radiative transfer model; Uncertainty evaluation; Spectral irradiance

1. Introduction

A reliable assessment of solar resource is important for the development of the renewable energy sector. The uncertainty in modelled or measured irradiance values

propagates into models for radiation and energy predictions, performance estimators for energy systems, degradation assessment tools. The attractiveness for investments on solar energy projects is therefore dependent upon the quality of broadband and spectral data.

Simulation of irradiance is useful when measurements are not available at a certain site, or information about the irradiance distribution and variability on a certain area is needed. In order to satisfy these purposes, nowadays

* Corresponding author at: Institute for Renewable Energy, EURAC Research, Viale Druso 1, 39100 Bolzano, Italy. Tel.: +39 471 055626; fax: +39 471 055699.

E-mail address: giorgio.belluardo@eurac.edu (G. Belluardo).

many tools have been developed that differ on the spectral region resolved, computation algorithm, geometrical schematization, licence type etc. An overview and classification of the most commonly used tools is given by Myers (2005) and by Seidel et al. (2010).

Many authors have reported about accuracy of simulation tools by comparing broadband or spectral irradiance measurements with simulations results, especially under clear-sky conditions (Gueymard, 1995; Myers, 2005; Ding et al., 2011; Clough et al., 2005). Other authors have focused on the estimation of uncertainty of parameters (aerosols, water vapor, ozone etc.) used as input to simulation tools (Gueymard, 2004; Xia et al., 2007; Holben et al., 2001; Perez-Ramirez et al., 2014; Schuster et al., 2006; Toledano et al., 2007; Dubovik et al., 2000; Andrews et al., 2006). However, few studies exist on how much the input uncertainty propagates into the simulation tools generating uncertainty in the output. Among these, Weihs and Webb (1997) and Román et al. (2014a), Román et al. (2014b) calculate the contribution of each input quantity x by performing simulations of broadband irradiance at $x - e$ and $x + e$, where x is a reference value and e is the combined uncertainty associated to x , and assuming their difference with the reference output as the output uncertainty. The two mentioned studies differ on the method used to combine the uncertainties of the different input parameters: Weihs and Webb (1997) sum up these single uncertainty contributions, Román et al. (2014b) perform all possible combinations of input parameters to find the one giving the highest output uncertainty. This way, possible correlations between input parameters are properly taken into account. Another method is proposed by Cordero et al. (2007): using Monte Carlo technique, it is possible to calculate the output uncertainty due to the effect of a single input parameter or of the combination of more input parameters by calculating statistics on a series of $N \gg 1$ randomly generated spectra. This way, the analysis can easily be performed both on broadband and spectral model output irradiance. Nevertheless, the analysis performed by Cordero et al. (2007) is limited to the UV region (280 nm to 400 nm). The main objective of the present work is to extend the analysis of Cordero et al. (2007) to a broader spectral region (280 nm to 2500 nm). The usefulness is twofold: investigating uncertainty propagation at wavelengths that are important (a) for photovoltaic sensitivity to sunlight, and therefore concur to the generation of current, (b) for the sensitivity of the available spectroradiometers, in order to add information on uncertainty when comparing spectral simulations and measurements. The Radiative Transfer Model (RTM) used in the investigation is SDISORT implemented in the tool UVSPEC, and simulations are performed under clear-sky conditions. The paper is structured as follows: Section 2 introduces the RTM SDISORT, the tool UVSPEC and the uncertainty propagation method based on Monte Carlo technique. Section 3 focuses on the obtained results. In particular, Section 3.1 identifies the contributions of each input

parameter to SDISORT output uncertainty, considering different levels of input uncertainty. In Section 3.2 realistic uncertainty levels associated to each input parameter are introduced to see which parameters realistically contribute more to the model output uncertainty. Section 3.3 investigates how the variation of input parameters influences the output uncertainty. From this analysis, minimum and maximum limits of output uncertainty are derived within which a spectral simulation based on the same sources of input parameters is supposed to lie. Finally, the main conclusions are summarized in Section 4.

2. Methodology

2.1. SDISORT and the radiative transfer tool UVSPEC

The propagation of energy in form of electromagnetic radiation from Sun to Earth's surface is affected by phenomena of scattering, absorption and emission caused by the interaction with the Earth's atmosphere. This process is mathematically described by the Radiative Transfer Equation (RTE) (Smith, 1985) that, given a set of input parameters, can be solved in a numerical way with a RTM. One of the most used RTE solvers is the Discrete Ordinates Radiative Transfer Program for a Multi-Layered Plane-Parallel Medium (DISORT) (Stamnes et al., 1988). A complete description of DISORT and its implementation can be found in Stamnes et al. (2000). In this study a modified version of DISORT is used to take the sphericity of the Earth's atmosphere into account, namely SDISORT (Dahlback and Stamnes, 1991). Both DISORT and SDISORT are implemented in the UVSPEC tool (Kylling, 1992; Mayer et al., 1997) and included in the libRadtran software package (Mayer and Kylling, 2005). In addition to ten different RTE solvers, UVSPEC provides several options to define the properties of multilayer atmospheric constituents (molecules, aerosol particles, water and ice clouds), and a surface as lower boundary. Several parameters are considered as input to model: surface albedo, extraterrestrial spectrum, solar zenith angle, aerosol properties, water and ozone column. These parameters are widely recognized as those that influence the output most (Manninen et al., 2012; Eltbaakh et al., 2011; Betts, 2005). Each input parameter and its source is introduced below. In general, data time series are collected from available online datasets or tools.

The extraterrestrial spectrum (S) used in this study is derived by Gueymard (2004) from the analysis and synthesis of twenty-three existing measured or modelled spectra.

Solar zenith angle (θ) is determined with the tool SolPos distributed by the National Renewable Energy Laboratory (NREL, 2015), by giving a specific location and time of the day as input.

Surface albedo (A), i.e. the ratio of reflected radiation from the surface to incident radiation upon it, can be downloaded from CMSAF platform (CMSAF, 2015), which collects data retrieved from the Advanced Very High

Resolution Radiometer (AVHRR) onboard the polar orbiting NOAA and MetOp satellites. These values are wavelength-independent weekly averages on $15 \times 15 \text{ km}^2$ surfaces.

Values of total ozone column (o) are available from the WDC platform (WDC, 2015), level 3 data quality. They are retrieved from GOME-2 instrument mounted onboard the EUMETSATs MetOp-A satellite, and refer to daily averages with a spatial resolution of $80 \times 40 \text{ km}^2$.

Total precipitable water (or water vapor, w) and aerosol properties are obtained from NASA AERONET network (Holben et al., 1998) from values measured with a CIMEL sunphotometer at Kanzelhöhe Observatory station (Austria). This site is in fact taken as a reference for the calculations performed in this study. Values are measured several times per day, and are interpolated in order to get the value corresponding to a specific time of the day. In particular, the aerosol properties used in this study are the Ångström exponent (α) and Ångström turbidity coefficient (β), single scattering albedo (ω) and asymmetry factor (g). Ångström parameters α and β are derived from the Ångström law $\delta = \beta \cdot \lambda^\alpha$, where λ is the wavelength in μm and δ is the Aerosol Optical Depth (AOD) at that wavelength. The parameter α is related to the distribution of aerosol particle size. In particular, higher values of α indicate a predominance of small particles, while lower values of α indicate a predominance of big particles. The parameter β is related to the amount of aerosol particles. In our case, the Ångström exponent α is obtained from AERONET AOD measurements between 440 nm and 870 nm, while the turbidity β is obtained from the α value and AOD at 1020 nm. Single scattering albedo ω represents the ratio of scattering efficiency to total extinction (absorption plus scattering) efficiency. This parameter therefore indicates the probability that the incoming irradiance will be scattered rather than absorbed when interacting with aerosol particles. The parameter ω is determined as the weighted average of ω from AERONET in the wavelengths 441, 674, 870 and 1020 nm. Finally, aerosol asymmetry factor g indicates states between a complete forward scattering ($g = 1$) and a complete backward scattering ($g = -1$). It is determined as the value of g from AERONET at 441 nm.

In addition to the nine input parameters described above, the following information and options are set:

- A standard atmosphere referred to as *US Standard, 1976* (NASA, 1976). This model describes the idealized, steady-state atmosphere for moderate solar activity by providing single profiles of temperature, pressure, density, acceleration caused by gravity, pressure scale height, number density, mean particle speed, mean collision frequency, mean free path, mean molecular weight, sound speed, dynamic viscosity, kinematic viscosity, thermal conductivity and geopotential altitude, from 0 to 1000 km. Computations are based on the perfect gas theory and a series of adopted constants, and have been

corroborated by rocket and satellite data. The standard atmospheric profile is then scaled according to the values of the different input parameters. No scaling is performed for trace gases since their influence on the spectrum at Earth's surface was found to be negligible.

- Spectral range: from 280 nm to 2500 nm. This spectral range contains the regions: ultraviolet-B (UV-B, from 280 nm to 315 nm), ultraviolet-A (UV-A, from 315 nm to 380 nm), visible (VIS, from 380 nm to 780 nm), near infrared (NIR, from 780 nm to 1400 nm) and part of short wave infrared (SWIR, from 1400 nm to 3000 nm). The range is broad enough to include the spectral responsivity of all commercially available photovoltaic modules, usually ranging from 300 nm to 1300 nm (Silverman et al., 2014), and next generation PV technologies currently in the lab stadium, as well as of spectroradiometers (Galleano et al., 2015).
- An aerosol model, which is then modified according to the aerosol properties provided as input, referred to as *aerosol default*, and corresponding to the model by Shettle and aerosols (1990): a rural type aerosol in the boundary layer, background aerosol above 2 km, spring-summer conditions and a visibility of 50 km.
- Six streams approximation for the solution of the radiative transfer equation.

A reference set of input parameters is set, corresponding to the atmospheric state at 10:00 (UTC0 time) on April 25th, 2013 at Kanzelhöhe Observatory (N 46.678°, E 13.907°, altitude 1526 m a.s.l.). This time is chosen since the quality of data measured with a sunphotometer is high for that day (level 2 observations: cloud-screened and quality-assured), and the sky is clear for the whole day. The above mentioned conditions are of course not representative of all the possible atmospheric conditions under clear sky. In any case, the effect of the deviation of input parameters from the reference values on the model output uncertainty is also discussed in Section 3.3.

A first run of UVSPEC program is performed with the set of values shown in Table 1, in order to generate the reference spectrum of global horizontal irradiance (GHI), diffuse horizontal irradiance (DiffHI), and direct horizontal irradiance (DirHI). The spectrally resolved GHI is compared to the measurement taken at the same time

Table 1

Reference set of input parameters for SDISORT model. Values refer to 10:00 (UTC0 time) on April 25th, 2013 at Kanzelhöhe Observatory site.

Parameter	Reference value
extraterrestrial spectrum (S)	Gueymard (2004)
solar zenith angle (θ)	35.85°
surface albedo (A)	0.12
ozone column (o)	321.27 DU
water vapor (w)	7.43 mm
Ångström exponent (α)	1.13
Ångström turbidity coefficient (β)	0.025
aerosol single scattering albedo (ω)	0.99
aerosol asymmetry factor (g)	0.67

and place with a spectroradiometer EKO MS-710 in the range 350–900 nm, as shown in Fig. 1. The broadband irradiance value (integral value of the spectrum) is 469.9 W/m² for measured spectrum and 466.3 W/m² for simulated spectrum, while the corresponding Mean Absolute Error (MAE), Mean Bias Error (MBE) and Root Mean Square Error (RMSE) are, respectively, −6.4 W/m², 20.1 W/m² and 23.7 W/m². The absolute values of MAE, MBE, and RMSE, divided by the integral of the measured solar spectrum, give a relative value of −1.4% for MAE, of 4.3% for MBE and of 5.0% for RMSE. These results are in line with the values of MBE and RMSE calculated from an outdoor intercomparison of ten spectroradiometers from five institutions (Habte et al., 2014), ranging between −3.5% and 5.7% for MBE and between 2.7% and 7.9% for RMSE (values determined considering only the spectral range between 380 nm and 900 nm). The instrumental uncertainty of the EKO MS-710 has not been experimentally determined. However, this is the combination of calibration uncertainty and measurement repeatability once the spectroradiometer is positioned outdoor. In particular, the calibration uncertainty is dependent upon the metrology laboratory conditions during calibration, such as the quality of spectral irradiance lamp standards, the relative humidity, the ambient temperature and the geometry of source and optical receiver (Yoon and Gibson, 2011; Myers and Andreas, 2004). A summary of calibration uncertainties of spectroradiometers from different research institutes is given by Galleano et al. (2014).

2.2. Monte Carlo method for uncertainty propagation

Given a quantity Q , resulting from a measurement process, the uncertainty associated to Q is defined as the dispersion of the value that could be attributed to the measurand (GUM - JCGM 100, 2008). The dispersion of values for Q is described by a Probability Density Function (PDF). If the PDF is known, the standard uncertainty of Q corresponds to its standard deviation. In most cases, the measurand Q is not measured directly, but is determined

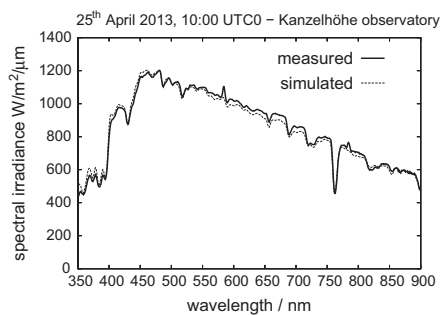


Fig. 1. Comparison of solar spectrum measured with an EKO MS-710 spectroradiometer at 10:00 (UTC0 time) on April 25th, 2013 at Kanzelhöhe Observatory site and the solar spectrum simulated with SDISORT using the reference set of input parameters as in Table 1.

through a measurement model, i.e. $Q = M(\mathbf{P})$, where $\mathbf{P} = (P_1, P_2, \dots, P_{N_{par}})$ is a vector of N_{par} input quantities that can be themselves measured or dependent from other quantities. The dispersion of the values of such N_{par} input quantities is defined by PDFs. If the model $Q = M(\mathbf{P})$ is linear or nonlinear, but differentiable, the standard uncertainty of Q can be obtained from the law of propagation of uncertainty (GUM - JCGM 100, 2008). This turns to be a difficult task when the model is nonlinear and not differentiable. In this case, the Monte Carlo method is more appropriate. This technique consists in approximating the PDF of the quantity Q in a numerical way, by making random draws from the probability distributions of the input quantities, and evaluating the model at the resulting values. In a first step, PDFs are assigned to input quantities $P_1, P_2, \dots, P_{N_{par}}$. Next, a computer algorithm generates an input vector $p_1 = (p_{1,1}, p_{1,2}, \dots, p_{1,N_{par}})$, where each element $p_{1,j}$ of the vector is calculated according to the PDF of the j th input parameter. The input vector is applied to the model $Q = M(\mathbf{P})$, in order to generate the output value q_1 . The generation of input vectors and corresponding output values is repeated N times, where $N \gg 1$. At the end of the process, a series of N output values is available, the frequency distribution of which corresponds to the PDF of the quantity Q . The standard uncertainty of Q is finally determined by calculating the standard deviation of the series of N output values.

The numerically-solved Radiative Transfer Equation implemented in SDISORT can be assimilated to a model $Q = M(\mathbf{P})$ where \mathbf{P} is the vector of input parameters. Being not linear and not differentiable, the Monte Carlo approach can be applied to determine model uncertainty. This requires the knowledge of the PDF of all model input parameters. Unfortunately, SDISORT input values correspond to meteorological and climatological measurements that are not possible to perform directly under repeatability conditions. In other words, it is not possible to assign a PDF to each input parameter simply from measurements. A possible approach to follow is the methodology described by Cordero et al. (2007), that consists in assigning PDFs according to the principle of maximum entropy (GUM - JCGM 101, 2008). This means to select one of the most probable PDFs among those that comply with the restrictions imposed by the available information. In our case for a single measured value p_j of the input quantity P_j , an error bound d_j that corresponds to the maximum error reasonably attributed to p_j is chosen based on experience or from literature. When only the error bound information is available, the most probable PDF is a rectangular distribution over the interval $(p_j - d_j, p_j + d_j)$ (Cordero et al., 2007), i.e. a distribution that associates the same probability to all value in the considered interval, and the standard uncertainty related to p_j is:

$$u(p_j) = \frac{d_j}{\sqrt{3}} \quad (1)$$

Once the PDF shape, the error bound and a single measured value are known for each input parameter, it is possible to perform $N \gg 1$ draws, i.e. to generate $N \gg 1$ values of each input parameter. In our case the free software Statistics101 implementing the Monte Carlo algorithm (Grosberg, 2015) is used and a number of $N = 500$ draws is found to be sufficient for the analysis. The generated values are combined in $N = 500$ input vectors and fed into SDISORT in order to generate $N = 500$ outputs of GHI, DiffHI and DirHI spectra. A statistical analysis is therefore performed, consisting in the calculation of the standard deviation u_G , the mean value I_G and the ratio u_G/I_G of the pool of $N = 500$ spectral irradiance values at each wavelength between 280 nm and 2500 nm. The first of the mentioned quantities corresponds to the standard uncertainty (or absolute uncertainty, expressed in $\text{W/m}^2/\text{nm}$), the latter to the relative standard uncertainty (expressed as a percentage). In this work the term *relative standard uncertainty* is often substituted with the term *uncertainty* for simplification reasons. The same kind of analysis is performed also on the pool of $N = 500$ values of broadband irradiance (corresponding to the integral values of the spectra), and can be theoretically performed on any kind of quantity deriving from spectral irradiance.

The application of the methodology is schematized in Fig. 2. In particular, the described methodology involves simultaneous draws of all input parameters and is used to analyze the combined effect of the input parameters uncertainty on SDISORT output uncertainty. Instead, Fig. 3 represents a similar process that involves draws of an input parameter at a time, while leaving the other input parameters equal to their reference value as in Table 1. This second option is applied to study the effect of one specific input parameter uncertainty on SDISORT output uncertainty.

3. Simulation results

3.1. Impact of input parameters uncertainty on SDISORT uncertainty

In a first instance, we perform a sensitivity analysis of the uncertainty of SDISORT ascribable to each input quantity: by assuming different values of error bounds for each input parameter, we want to investigate how the

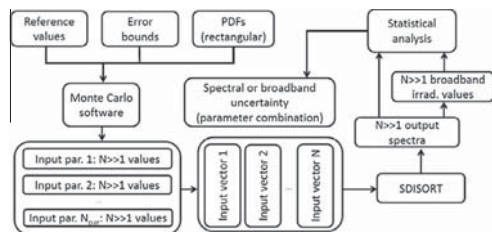


Fig. 2. Schematization of the methodology involving the use of Monte Carlo technique for the evaluation of SDISORT uncertainty given by the simultaneous propagation of the uncertainties of all input parameters.

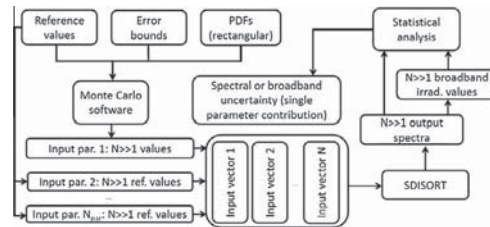


Fig. 3. Schematization of the methodology involving the use of Monte Carlo technique for the evaluation of SDISORT uncertainty given by the propagation of the uncertainty of only one specific input parameter (in the example, input parameter 1).

uncertainty of the model output varies. Therefore, ten different error bounds are assigned, indicated as percentage: $\pm 0.1\%$, $\pm 0.2\%$, $\pm 0.5\%$, $\pm 1\%$, $\pm 2\%$, $\pm 5\%$, $\pm 10\%$, $\pm 20\%$, $\pm 50\%$, $\pm 100\%$. Each percentage corresponds to the maximum variation of input value with respect to the corresponding reference value listed in Table 1. Note that for the extraterrestrial spectrum the error bound corresponds to the same percent shift at all wavelengths with respect to the reference one. Therefore for this case, by applying the assigned error bounds, only the integral value of the input extraterrestrial spectrum changes, while the shape remains the same.

The methodology described in the previous section and schematized in Fig. 3 is therefore applied. Table 2 shows the values of relative standard uncertainty of broadband irradiance values generated by UVSPEC tool. This is useful to get a hint on the contribution of each input parameter to the uncertainty of the model output, once a specific error bound has been assigned. In particular, the highest values of uncertainty seem to be related to the diffuse component of solar spectrum. It is also interesting to see that the effect of the variability of extraterrestrial spectrum uncertainty propagates in the same way within GHI, DiffHI and DirHI. On the other hand, no indication can be inferred for the combined effect of two or more input parameters from the calculation of the sum of squares of each contribution, since correlations exist and affect the combined uncertainty.

3.2. Analysis of SDISORT uncertainty contributors

In the previous section, the relative standard uncertainty of the model output has been evaluated after assigning several levels of error bounds to the different input parameters. In order to deepen our analysis, we now assign a specific and reasonable set of error bounds to the input parameters. We therefore focus on a real case to see which parameters contribute more to the model output uncertainty, and how their effect varies at different spectral regions, as well as on a broadband level. As mentioned in Section 2.2, the value of error bound strictly depends upon the characteristics of the measurement instrument and

Table 2

Relative standard uncertainty (values in percentage) of SDISORT due to the uncertainty of input parameters, at varying error bound, for each component GHI, DiffHI and DirHI. The results are obtained considering the uncertainty of one input parameter at time applied (as schematized in Fig. 3) to the corresponding reference value as in Table 1. n.a.: not affected. S : extraterrestrial spectrum, θ : solar zenith angle, A : surface albedo, o : ozone column, w : water vapor, α : Angström exponent, β : Angström turbidity coefficient, ω : aerosol single scattering albedo, g : aerosol asymmetry factor.

Parameter	0.1%	0.2%	0.5%	1%	2%	5%	10%	20%	50%	100%
<i>Error bound – global horizontal irradiance</i>										
S	0.06	0.12	0.29	0.58	1.11	2.95	5.61	11.60	29.17	56.69
θ	0.03	0.06	0.15	0.29	0.56	1.47	2.81	5.77	14.64	31.75
A	<0.01	<0.01	<0.01	<0.01	0.01	0.03	0.05	0.10	0.25	0.51
o	<0.01	<0.01	<0.01	0.01	0.01	0.04	0.07	0.15	0.37	0.80
w	<0.01	<0.01	0.01	0.02	0.04	0.09	0.18	0.37	0.96	2.47
α	<0.01	<0.01	<0.01	<0.01	<0.01	0.01	0.02	0.04	0.09	0.21
β	<0.01	<0.01	<0.01	<0.01	0.01	0.02	0.03	0.06	0.16	0.32
ω	<0.01	0.01	0.01	0.03	0.05	0.13	0.24	0.46	1.04	1.95
g	<0.01	<0.01	<0.01	0.01	0.01	0.04	0.07	0.15	0.36	0.60
<i>Error bound – diffuse horizontal irradiance</i>										
S	0.06	0.12	0.29	0.58	1.11	2.95	5.61	11.60	29.17	56.69
θ	0.01	0.02	0.05	0.09	0.18	0.47	0.89	1.84	4.88	12.03
A	0.01	0.01	0.03	0.05	0.10	0.27	0.51	1.06	2.66	5.37
o	<0.01	<0.01	0.01	0.02	0.03	0.08	0.15	0.32	0.82	2.06
w	<0.01	<0.01	<0.01	0.01	0.01	0.03	0.06	0.13	0.34	0.83
α	0.01	0.02	0.06	0.12	0.23	0.60	1.15	2.37	6.01	12.47
β	0.02	0.05	0.12	0.23	0.44	1.16	2.21	4.56	11.47	22.92
ω	0.03	0.06	0.15	0.30	0.57	1.40	2.52	4.90	11.45	21.99
g	0.01	0.02	0.04	0.08	0.15	0.41	0.77	1.59	3.85	6.68
<i>Error bound – direct horizontal irradiance</i>										
S	0.06	0.12	0.29	0.58	1.11	2.95	5.61	11.60	29.17	56.69
θ	0.03	0.06	0.16	0.31	0.60	1.58	3.01	6.17	15.66	33.92
A	n.a.	n.a.	n.a.	n.a.	n.a.	n.a.	n.a.	n.a.	n.a.	n.a.
o	<0.01	<0.01	<0.01	0.01	0.01	0.03	0.06	0.13	0.32	0.68
w	<0.01	<0.01	0.01	0.02	0.04	0.10	0.19	0.40	1.03	2.64
α	<0.01	<0.01	0.01	0.01	0.03	0.07	0.14	0.29	0.73	1.58
β	<0.01	0.01	0.01	0.03	0.05	0.14	0.26	0.54	1.36	2.77
ω	n.a.	n.a.	n.a.	n.a.	n.a.	n.a.	n.a.	n.a.	n.a.	n.a.
g	n.a.	n.a.	n.a.	n.a.	n.a.	n.a.	n.a.	n.a.	n.a.	n.a.

method, and can be derived either from previous studies or from experience. In our case we apply a security factor to values of uncertainty available in the literature, provided that the data type, the measurement instruments and the boundary conditions (for example, some values of uncertainty are valid at specific ranges of solar zenith angle or are associated to other specific atmospheric conditions) are ascribable to our case. The set of selected error bounds and the literature source for input uncertainties are reported in Table 3.

As before, for each input parameter a series of $N = 500$ values lying within the error bounds specified in Table 3 is generated according to a uniform distribution with a Monte Carlo based computer software. In a first step, the generated values are fed into SDISORT to generate just as many GHI, DiffHI and DirHI spectra, in such a way that only one input parameter at a time varied, while assigning reference values to the remaining ones (methodology as in Fig. 3). Later, all generated values are fed into SDISORT simultaneously, in order to account for the simultaneous and interacting effect of the uncertainty of input parameters (methodology as in Fig. 2). Results are shown in Fig. 4. Plots on the left show the whole spectral

range 280–2500 nm and is useful to identify the major contributors in the VIS, NIR and SWIR regions, while plots on the right are scaled in order to focus on the UV-B and UV-A parts. The values of output uncertainty of broadband GHI, DiffHI and DirHI, for each considered spectral region and for the whole range, are reported in Table 4. First of all, it is verified that the combined uncertainty does not correspond to the sum of squares of each contributor. This is expected, since some correlation exist between input parameters within the radiative transfer equation, and confirms the suitability of a Monte Carlo based approach for this kind of analysis.

The major contributors of SDISORT output uncertainty for GHI, given the set of error bounds shown in Table 3, are extraterrestrial spectrum and Angström turbidity coefficient β . The effect of extraterrestrial spectrum on uncertainty propagation is constant for the whole spectral range, around 2.95%. The influence of Angström turbidity coefficient β is more evident in the UV region (broadband uncertainty of 0.84% at UV-B and 0.65% at UV-A, with a local spectral uncertainty peak of around 1.4%), while it decreases at increasing wavelengths, with

Table 3
Error bounds associated to the input parameters measured at 10:00 on April 25th, 2013 at Kanzelhöhe Observatory site, and listed in Table 1.

Parameter	Error bound	Source
S	5%	Gueymard (2004)
θ	0.03°	NREL (2015)
A	25%	Xia et al. (2007)
o	5%	Valks et al. (2011)
w	10%	Holben et al. (2001), Perez-Ramirez et al. (2014)
α	0.08	Schuster et al. (2006), Toledano et al. (2007)
β	0.025	Holben et al. (1998), Eck et al. (2001)
ω	0.05	Dubovik et al. (2000)
g	0.05	Xia et al. (2007), Andrews et al. (2006)

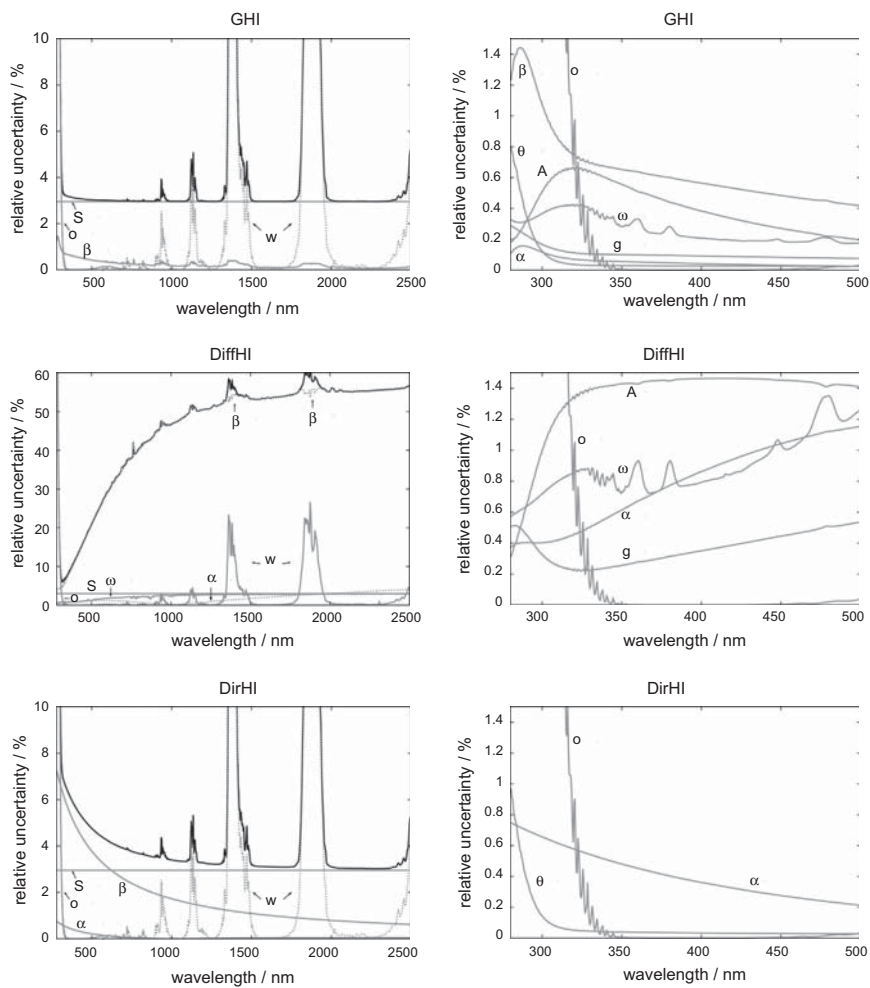


Fig. 4. Relative uncertainty (values in percentage) of the SDISORT output at varying wavelength, due to the uncertainty of each input parameter and to the combined effect of all input parameters, for GHI, DiffHI and DirHI. (left) view of the whole investigated spectral range (uncertainty due to combined effect is in black). (right) zoom on the UV part of the spectrum. S : extraterrestrial spectrum, θ : solar zenith angle, A : surface albedo, o : ozone column, w : water vapor, α : Ångström exponent, β : Ångström turbidity coefficient, ω : aerosol single scattering albedo, g : aerosol asymmetry factor.

Table 4

Uncertainty of SDISORT output ascribable to the uncertainty of the different input parameters and to their simultaneous effect (in italics) computed on the broadband values of GHI, DiffHI and DirHI in several spectral regions, and in the whole considered spectral range. n.a.: not affected. S : extraterrestrial spectrum, θ : solar zenith angle, A : surface albedo, o : ozone column, w : water vapor, α : Ångström exponent, β : Ångström turbidity coefficient, ω : aerosol single scattering albedo, g : aerosol asymmetry factor.

Spectral range	S	θ	A	o	w	α	β	ω	g	Simultaneous effects
<i>Global horizontal irradiance</i>										
UV-B (280–315 nm)	2.95	0.05	0.63	3.02	<0.01	0.08	0.84	0.41	0.13	<i>4.42</i>
UV-A (315–380 nm)	2.95	0.03	0.55	0.09	<0.01	0.05	0.65	0.31	0.10	<i>3.13</i>
VIS (380–780 nm)	2.95	0.02	0.16	0.05	0.03	0.02	0.38	0.16	0.07	<i>3.00</i>
NIR (780–1400 nm)	2.95	0.02	0.03	<0.01	0.34	0.00	0.20	0.08	0.04	<i>2.98</i>
SWIR (1400–2500 nm)	2.95	0.03	0.01	<0.01	0.62	0.01	0.11	0.04	0.02	<i>3.02</i>
all spectrum (280–2500 nm)	2.95	0.02	0.12	0.04	0.18	0.01	0.31	0.13	0.06	<i>2.99</i>
<i>Diffuse horizontal irradiance</i>										
UV-B (280–315 nm)	2.95	0.04	1.24	3.17	<0.01	0.42	4.61	0.81	0.25	<i>6.69</i>
UV-A (315–380 nm)	2.95	0.01	1.42	0.12	<0.01	0.61	7.28	0.81	0.26	<i>8.19</i>
VIS (380–780 nm)	2.95	0.01	1.35	0.05	0.02	1.06	21.81	1.34	0.57	<i>22.11</i>
NIR (780–1400 nm)	2.95	0.01	0.82	<0.01	0.35	0.13	45.28	2.35	1.16	<i>44.83</i>
SWIR (1400–2500 nm)	2.95	0.01	0.56	<0.01	0.68	2.35	54.05	2.81	1.47	<i>53.19</i>
all spectrum (280–2500 nm)	2.95	0.01	1.29	0.08	0.06	0.82	22.20	1.37	0.59	<i>22.47</i>
<i>Direct horizontal irradiance</i>										
UV-B (280–315 nm)	2.95	0.07	n.a.	2.86	<0.01	0.61	6.46	n.a.	n.a.	<i>7.80</i>
UV-A (315–380 nm)	2.95	0.04	n.a.	0.07	<0.01	0.47	5.60	n.a.	n.a.	<i>6.42</i>
VIS (380–780 nm)	2.95	0.03	n.a.	0.05	0.03	0.16	3.35	n.a.	n.a.	<i>4.51</i>
NIR (780–1400 nm)	2.95	0.02	n.a.	<0.01	0.34	0.00	1.76	n.a.	n.a.	<i>3.46</i>
SWIR (1400–2500 nm)	2.95	0.03	n.a.	<0.01	0.62	0.04	0.92	n.a.	n.a.	<i>3.15</i>
all spectrum (280–2500 nm)	2.95	0.03	n.a.	0.03	0.20	0.10	2.62	n.a.	n.a.	<i>3.98</i>

local peaks at water absorption bands. Focusing on the short-wavelength region, the influence of ozone on uncertainty propagation affects only the UV-B region (3.02% broadband uncertainty), while it can vary locally from around 110% to 4%. Nevertheless, the effect of the uncertainty of this atmospheric gas on the whole spectral range is negligible. Water vapor is an important source of uncertainty at water absorption bands, especially in the range 1350–1425 nm and 1800–1950 nm, where the value of spectral uncertainty can be higher than 10%.

The relative uncertainty of DirHI presents similarities with that of GHI, with the only exceptions of Ångström turbidity coefficient β and Ångström exponent α . The first is responsible for a broadband uncertainty of 6% in the UV region, which decreases but still remain considerable also in the VIS, NIR and SWIR regions with, respectively, 3.35%, 1.76% and 0.92% broadband uncertainty. The second has a lower influence than β , with more effects on the UV region of the spectrum.

The simultaneous uncertainty propagation of input parameters to the model output in DiffHI presents different characteristics for wavelengths higher than 315 nm than the previous cases, with increasing values reaching local peaks of spectral uncertainty of around 60% in the water absorption region 1800–1950 nm. On the whole spectral range, the uncertainty of broadband DiffHI is 22.37%. This behavior is almost completely attributable to Ångström turbidity coefficient β . The reason for these high values of uncertainty due to β is mostly explained by the high uncertainty associated to the AERONET source (100%, being the reference value equal to 0.025 and the associated error

bound equal to 0.025), which derives by the temperature-sensitivity of CIMEL sensor at wavelength 1020 nm where AOD is measured and from which β is derived. In the Version 3 of AERONET database, which will be released in 2016 (Eck, 2015), some corrections will be applied in order to reduce the effects of extreme temperature on AOD (and therefore β) accuracy, thus improving the associated uncertainty (Holben, 2013). The influence of the uncertainty of parameters representing aerosol properties is in general higher for DiffHI than for other cases, and is therefore not negligible: Ångström exponent α effect is higher in SWIR region (2.35% broadband uncertainty), while the effect of single scattering albedo and asymmetry factor is higher in NIR and SWIR regions (broadband uncertainties around 2.6% for ω and around 1.3% for g). The latter presents local peaks of spectral uncertainty at water absorption bands 1350–1425 nm and 1800–1950 nm (not visible in Fig. 4, for clarity reasons).

It is important to underline that this analysis is performed at specific values of input parameters referring to reference conditions of Table 1, and uncertainty values cannot therefore be generalized. However, the effect of deviation of input parameters from the reference set will be investigated in Section 3.3 in order to define a validity area within a minimum and maximum uncertainty limits, representing all possible combinations of input parameters.

3.3. Influence of variability of input parameters

In this section we analyze the effect of deviation of input parameters from the reference set on SDISORT output,

supposing that the set of error bounds remain the same as in Table 3. This way, it is possible to define an uncertainty area delimited by a minimum and maximum uncertainty boundaries, and satisfying all possible combinations of input parameters. Different values are assigned to each input parameter based on a specific step and within defined physical limits, and simulations are run in which one input parameter at a time varies according to the error bounds assigned in Table 3, while assigning reference values to the remaining ones (methodology as in Fig. 3). Results are summarized only for broadband GHI in Table 5 that shows, in addition to the selected steps and variability ranges used for the simulations, the values of input parameters that correspond respectively to the minimum and to the maximum output calculated uncertainty, and the values of uncertainties themselves. For example, values within the physical range from 0 nm to 50 mm are assigned to water vapor with a 5 mm step. The associated minimum output uncertainty is at 0 nm, while the maximum output uncertainty is at 50 nm and corresponds to 0.32%. In the case of extraterrestrial spectrum, no variability range and no step can be assigned since it is not possible to let a reference spectrum (in this case, the one by Gueymard (2004)) vary from a minimum to a maximum physical value. For this case, only an uncertainty value of 2.95% is assigned, as calculated in Section 3.2 and corresponding to an error bound of 5%.

In general the uncertainty of the model output depends on the value of the input parameter. When error bounds are defined as percentage, the output uncertainty tends to increase at increasing values of input parameter. The only exception is represented by surface albedo, which shows a peak of uncertainty at values around 0.75. As for error bounds defined as absolute value, the uncertainty of the model output can either increase (as in the case of solar zenith angle, Ångström exponent and Ångström turbidity coefficient), or decrease (as in the case of aerosol single scattering albedo and aerosol asymmetry factor) at increasing values of input parameters. Surface albedo and total precipitable water parameter variation affect the output uncertainty most, with a total variation of output uncertainty of, respectively, 0.86% and 0.32%. On the other hand, solar zenith angle does not seem to significantly

affect SDISORT output uncertainty. The latter result confirms the outcome of the work by Cordero et al. (2007) and extends it to wavelengths higher than 400 nm.

In addition, under the same set of error bounds as in Table 3, two additional simulations are run:

- one with a set of input parameters corresponding to the lowest output uncertainties of broadband GHI (column 3 of Table 5);
- one other with a set of input parameter values corresponding to the highest output uncertainties of broadband GHI (column 4 of Table 5).

This way, it is possible to identify a sort of uncertainty area within which all possible combinations of input parameters with error bounds as in Table 3 are likely to lie. This is reported in Fig. 5 (left), together with the spectral uncertainty due to simultaneous effect of reference input parameters, calculated in Section 3.2. Fig. 5 (right) shows the corresponding values of broadband uncertainty for GHI, for each spectral region. A high variability of SDISORT uncertainty occurs in the UV-B, UV-A and VIS regions, while the maximum and minimum output broadband uncertainties are comparable in the NIR and SWIR regions.

SDISORT uncertainty of broadband GHI in the investigated range 280–2500 nm ranges between a minimum of 2.9% and a maximum of 5.9%. It is interesting to notice that the latter value is higher than the value obtained from a simple sum of squares of the single uncertainties ascribable to each input parameter (equal to 3.1%), thus confirming once more the suitability of Monte Carlo to such a kind of analysis.

The obtained range of uncertainty can be compared with the uncertainty of spectra measured with spectroradiometers. As mentioned in Section 2.1, the latter is a combination of instrument calibration uncertainty and of repeatability of measurements performed outdoor. For example, Vasiliki et al. (2013) calculate a combined standard uncertainty of 2.5% ($k = 1$) for outdoor spectral measurements of the global normal irradiance (GNI). This value is lower but still comparable with the uncertainty calculated in this study. Furthermore, the gradual improve-

Table 5

Series of input parameters values selected to run UVSPEC tool, and values corresponding to maximum and minimum output broadband uncertainty for broadband GHI, respectively. Corresponding output uncertainty is displayed into brackets.

Parameter	Min–max value, step	Min value (unc.)	Max value (unc.)
S	Gueymard (2004)	– (2.95%)	– (2.95%)
θ	10°–70°, 10°	10° (0.01%)	70° (0.10%)
A	0.05–0.95, 0.10	0.05 (0.05%)	0.75 (0.91%)
o	250–500DU, 25DU	250DU (0.03%)	500DU (0.05%)
w	0–50 mm, 5 mm	0 (0.00%)	50 (0.32%)
α	0.5–2.5, 0.25	0.5 (0.01%)	2.5 (0.04%)
β	0–0.5, 0.05	0 (0.16%)	0.5 (0.36%)
ω	0.6–1, 0.05	1 (0.12%)	0.6 (0.14%)
g	0.5–0.9, 0.05	0.9 (0.04%)	0.5 (0.06%)

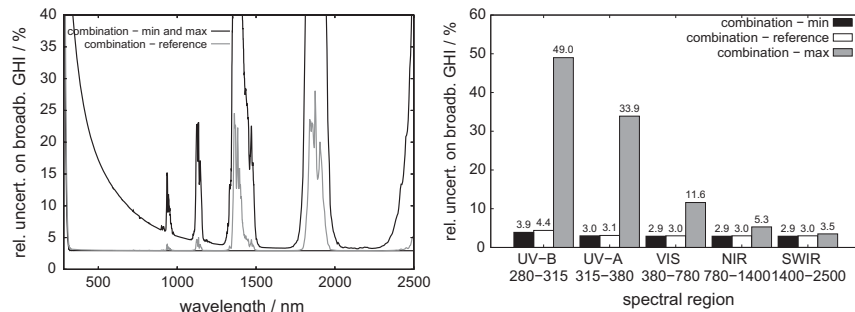


Fig. 5. Max and min relative spectral uncertainty of the SDISORT outputs for GHI due to the combination of input parameters generating, respectively, the highest and lowest uncertainty, and with values of error bounds as defined in Table 3. (left) output spectral uncertainties (right) output broadband uncertainties. Output spectral uncertainty from the reference set of input parameters as in Table 1 is also displayed.

ment of instruments and procedures for the retrieval of RTM input parameters looks promising and will push towards a reduction of uncertainty levels.

4. Conclusions

An analysis of uncertainty of SDISORT radiative transfer model implemented in the UVSPEC tool is presented in this paper. A Monte Carlo technique is used to investigate the propagation of the uncertainty of nine different input parameters into the model output. The uncertainty contribution of every single input parameter as well as of their combination to the uncertainty of spectral and broadband modelled irradiance is evaluated. The analysis is performed on the global horizontal irradiance (GHI), the diffuse horizontal irradiance (DiffHI), and the direct horizontal irradiance (DirHI). Results show that DiffHI is generally more affected by uncertainty than DirHI and GHI, both on the spectral and broadband level.

Considering a reference set of input parameters representing the atmospheric state at Kanzelhöhe Observatory (Austria) site at 10:00 on April 25th, 2013, and a set of associated error bounds, it is found that Ångström turbidity coefficient β explains most of the uncertainty in the broadband DiffHI (22.47% in the range 280–2500 nm), with increasing values at increasing wavelength. The effect of the uncertainty of this parameter is also evident in the broadband DirHI. The prominent role of β is mostly explained by the high value of error bound associated to AERONET source (100%, being the reference value equal to 0.025 and the associated error bound equal to 0.025). The uncertainty of this parameter must be therefore properly taken into consideration especially when dealing with DiffHI. On the other hand, in a new version of AERONET database that will be soon released (Eck, 2015) some corrections should be applied in order to reduce the associated uncertainty of this parameter.

As for the other input parameters, ozone column is an important source of uncertainty for all irradiance components at UV-B regions (280–315 nm), with values of output

spectral uncertainty of around 3%, and local peaks reaching also 110%. Extraterrestrial spectrum contributes for 2.95% of output uncertainty on the whole spectral range. However, efforts done in the last years in synthesizing less uncertain extraterrestrial spectra look promising (Gueymard, 2004). Minor contributions come from Ångström exponent α , evident in the SWIR region of DiffHI (2.35% broadband uncertainty) and aerosol single scattering albedo in the NIR and SWIR regions of DiffHI (2.35% and 2.81% broadband uncertainty, respectively). Finally, water vapor seems not to contribute significantly to the broadband output uncertainty (less than 0.70% on all spectral regions and for all broadband irradiance components), but can result in local peaks higher than 10% at water absorption bands, especially between 1350–1425 nm and 1800–1950 nm.

By studying the effect of deviation of input parameters from the above mentioned reference set, it is possible to conclude that the maximum uncertainty of broadband GHI calculated with SDISORT in the spectral regions included in the range 280–2500 nm is significantly high in UV-B, UV-A and VIS regions (49.0%, 33.9% and 11.6% respectively), while it tends to be closer to the corresponding minimum levels at NIR and SWIR (5.3% and 3.5% respectively). On the whole considered spectral range 280–2500 nm, the broadband uncertainty of GHI can vary between a minimum of 2.9% and a maximum of 5.9%. This range is higher, but still comparable to typical uncertainty values of global irradiance measurements performed with spectroradiometers. However, the gradual improvement of instruments and methodology for the derivation of RTM input quantities is bound to decrease the associated levels of uncertainty. The gradual reduction in model uncertainties must go in parallel with a reduction of uncertainty in spectral irradiance calibration and measurement. In fact, a low value of uncertainty of simulated spectrum is useful and valuable only when the model is used to simulate a measured spectrum that is close to the true value. Considering a model uncertainty of around 3–6% as found by this study, and a current state of the art spectral irradiance measurement uncertainty of 3–5%, combined values

of 6–11% actually represent a real estimate of the state of the art limit of error uncertainty in terrestrial solar spectral radiation estimates.

In general this study proves that, provided that the uncertainty of every single input parameter is known, the derivation of the output combined uncertainty with a classical propagation of error always underestimates the more realistic values obtained with a more appropriate technique like Monte Carlo, taking the correlation of input parameters into account.

Acknowledgements

The authors wish to acknowledge the European Regional Development Fund (ERDF) and the Stiftung Südtiroler Sparkasse for co-financing the Project 2-1a-97 “PV Initiative” and the Project 5-1a-232 “Flexi-BIPV”. The author David Moser wishes to acknowledge the European Union’s Horizon 2020 research and innovation programme under Grant Agreement No. 649997, Project “Solar Bankability”. The author Giorgio Belluardo would like to thank R. Galleano for the fruitful discussion on spectroradiometers uncertainty and T. Eck for the helpful suggestions concerning AERONET data.

References

- Andrews, E., Sheridan, P.J., Fiebig, M., McComiskey, A., Ogren, J.A., Arnott, P., Covert, D., Elleman, R., Gasparini, R., Collins, D., Jonsson, H., Schmid, B., Wang, J., 2006. Comparison of methods for deriving aerosol asymmetry parameter. *J. Geophys. Res. Atmos.* 111, D05S04.
- Betts, T.R., 2005. Investigation of photovoltaic device operation under varying spectral conditions Ph.D. Thesis. Loughborough University.
- Clough, S.A., Shephard, M.W., Mlawer, E.J., Delamere, J.S., Iacono, M. J., Cady-Pereira, K., Boukabara, S., Brown, P.D., 2005. Atmospheric radiative transfer modeling: a summary of the AER codes. *J. Quant. Spectrosc. Radiat. Transfer* 91 (2), 233–244.
- CMSAF, 2015. Surface radiation products <https://wui.cmsaf.eu/safira/action/viewProduktList?id=2> (accessed: 2015-05-25).
- Cordero, R., Seckmeyer, G., Pissulla, D., Dasilva, L., Labbe, F., 2007. Uncertainty evaluation of the spectral UV irradiance evaluated by using the UVSPEC radiative transfer model. *Opt. Commun.* 276, 44–53.
- Dahlback, A., Stamnes, K., 1991. A new spherical model for computing the radiation field available for photolysis and heating at twilight. *Planet. Space Sci.* 39, 671–683.
- Ding, S., Yang, P., Weng, F., Liu, Q., Han, Y., van Delst, P., Li, J., Baum, B., 2011. Validation of the community radiative transfer model. *J. Quant. Spectrosc. Radiat. Transfer* 112, 1050–1064.
- Dubovik, O., Smirnov, A., Holben, B.N., King, M.D., Kaufman, Y.J., Eck, T.F., Slutsker, I., 2000. Accuracy assessments of aerosol optical properties retrieved from Aerosol Robotic Network (AERONET) Sun and sky radiance measurements. *J. Geophys. Res. Atmos.* 105, 9791–9806.
- Eck, T., 2015. Private communication.
- Eck, T.F., Holben, B.N., Dubovik, O., Smirnov, A., Slutsker, I., Lobert, J.M., Ramanathan, V., 2001. Column-integrated aerosol optical properties over the Maldives during the northeast monsoon for 1998–2000. *J. Geophys. Res. Atmos.* 106, 28555–28566.
- Eltbaakh, Y.A., Ruslan, M.H., Alghoul, M.A., Othman, M.Y., Zaharim, A., Sopian, K., 2011. Effect of cloudless sky parameters on global spectral solar radiation within 0.3–1.1 μm region. *Proc. 4th WSEAS International Conference on Energy and Development, Environment and Biomedicine*, pp. 209–213.
- Galleano, R., Zaaiman, W., Strati, C., Bartocci, S., Pravettoni, M., Marzoli, M., Fucci, R., Leanza, G., Timó, G., Minuto, A., Catena, M., Aleo, F., Takagi, S., Akiyama, A., Nuez, R., Belluardo, G., 2015. Second international spectroradiometer intercomparison: results and impact on PV device calibration. *Prog. Photovolt.: Res. Appl.* 23 (7), 929–938.
- Galleano, R., Zaaiman, W., Virtuani, A., Pavanello, D., Morabito, P., Minuto, A., Spena, A., Bartocci, S., Fucci, R., Leanza, G., Fasanaro, D., Catena, M., 2014. Intercomparison campaign of spectroradiometers for a correct estimation of solar spectral irradiance and potential impact on photovoltaic devices calibration. *Prog. Photovolt.: Res. Appl.* 22 (11), 1128–1137.
- Grosberg, J., 2015. Statistics 101 [computer software] <http://www.statistics101.net/> (accessed: 2015-05-26).
- Gueymard, C., 1995. Simple model of the atmospheric radiative transfer of sunshine, version 2 (SMARTS2): algorithms description and performance assessment. Tech. Rep. FSEC-PF-270-95, Florida Solar Energy Center.
- Gueymard, C.A., 2004. The sun’s total and spectral irradiance for solar energy applications and solar radiation models. *Sol. Energy* 76 (4), 423–453.
- GUM - JCGM 100:2008, 2008. Evaluation of measurement data – guide to the expression of uncertainty in measurement.
- GUM - JCGM 101:2008, 2008. Evaluation of measurement data: supplement 1 to the guide to the expression of uncertainty in measurement: propagation of distributions using a Monte Carlo method.
- Habte, A., Andreas, A., Ottoson, L., Gueymard, C., Fedor, G., Fowler, S., Peterson, J., Naranen, E., Kobashi, T., Akiyama, A., Takagi, S., 2014. Indoor and outdoor spectroradiometer intercomparison for spectral irradiance measurement Tech. Rep. NREL/TP-5D00-61476. National Renewable Energy Laboratory.
- Holben, B., 2013. AERONET update: development of version 3 http://aeronet.gsfc.nasa.gov/new_web/Publications/quarterlies/Update_Mar7_Version_3.pdf (accessed: 2015-10-01).
- Holben, B., Tanr, D., Smirnov, A., Eck, T.F., Slutsker, I., Abuhassan, N., Newcomb, W., Schafer, J.S., Chatenet, B., Lavenu, F., Kaufman, Y.J., Vande Castle, J., Setzer, A., Markham, B., Clark, D., Frouin, R., Halthore, R., Karneli, A., O’Neill, N., Pietras, C., Pinker, R., Voss, K., Zibordi, G., 2001. An emerging ground-based aerosol climatology: aerosol optical depth from AERONET. *J. Geophys. Res. Atmos.* 106, 12067–12097.
- Holben, B.N., Eck, T.F., Slutsker, I., Tanr, D., Buis, J.P., Setzer, A., Vermote, E., Reagan, J.A., Kaufman, Y.J., Nakajima, T., Lavenu, F., Jankowiak, I., Smirnov, A., 1998. AERONET – a federated instrument network and data archive for aerosol characterization. *Remote Sens. Environ.* 66 (1), 1–16.
- Kylling, A., 1992. Radiation transport in cloudy and aerosol loaded atmospheres Ph.D. Thesis. Alaska University.
- Manninen, T., Riihel, A., de Leeuw, G., 2012. Atmospheric effect on the ground-based measurements of broadband surface albedo. *Atmos. Meas. Tech.* 5 (11), 2675–2688.
- Mayer, B., Kylling, A., 2005. Technical note: the libRadtran software package for radiative transfer calculations – description and examples of use. *Atmos. Chem. Phys.* 5, 1855–1877.
- Mayer, B., Seckmeyer, G., Kylling, A., 1997. Systematic long-term comparison of spectral UV measurements and UVSPEC modeling results. *J. Geophys. Res. Atmos.* 102, 8755–8767.
- Myers, D., Andreas, A., 2004. Sensitivity of spectroradiometric calibrations in the near infrared to variations in atmospheric water vapor. *Proc. American Solar Energy Society Annual Conference*, Portland, Oregon.
- Myers, D.R., 2005. Solar radiation modeling and measurements for renewable energy applications: data and model quality. *Energy* 30 (9), 1517–1531.

- NASA, 1976. U.S. Standard Atmosphere, 1976. Tech. rep., NASA TM-X-74335.
- NREL, 2015. Solar position and intensity calculator (SOLPOS) <http://www.nrel.gov/midc/solpos/solpos.html> (accessed: 2015-05-22).
- Perez-Ramirez, D., Whiteman, D.N., Smirnov, A., Lyamani, H., Holben, B.N., Pinker, R., Andrade, M., Alados-Arboledas, L., 2014. Evaluation of AERONET precipitable water vapor versus microwave radiometry, GPS, and radiosondes at ARM sites. *J. Geophys. Res. Atmos.* 119 (15), 2014JD021730.
- Román, R., Bilbao, J., de Miguel, A., 2014a. Solar radiation simulations in the Iberian Peninsula: accuracy and sensitivity to uncertainties in inputs of a radiative transfer model. *J. Quant. Spectrosc. Radiat. Transfer* 145, 95–109.
- Román, R., Bilbao, J., de Miguel, A., 2014b. Uncertainty and variability in satellite-based water vapor column, aerosol optical depth and Ångström exponent, and its effect on radiative transfer simulations in the Iberian Peninsula. *Atmos. Environ.* 89, 556–569.
- Schuster, G.L., Dubovik, O., Holben, B.N., 2006. Ångström exponent and bimodal aerosol size distributions. *J. Geophys. Res. Atmos.* 111, D07207.
- Seidel, F.C., Kokhanovsky, A.A., Schaepman, M.E., 2010. Fast and simple model for atmospheric radiative transfer. *Atmos. Meas. Tech.* 3 (4), 1129–1141.
- Shettle, E., aerosols, Models of, 1990. clouds and precipitation for atmospheric propagation studies. In: *Proc. AGARD Conference*, vol. 454.
- Silverman, T., Jahn, U., Friesen, G., Pravettoni, M., Apolloni, M., Louwen, A., van Sark, W., Schweiger, M., Belluardo, G., Wagner, J., Tetzlaff, A., Ingenhoven, P., Moser, D., 2014. IEA-PVPS T13-02:2014. Characterisation of performance of thin-film photovoltaic technologies.
- Smith, W.L., 1985. Satellites. In: *Handbook of Applied Meteorology*. John Wiley & Sons, New York (Chapter 10).
- Stamnes, K., Tsay, S.-C., Wiscombe, W., Laszlo, I., 2000. DISORT, a general-purpose Fortran program for discrete-ordinate-method radiative transfer in scattering and emitting layered media: documentation of methodology Tech. rep., Department of Physics and Engineering Physics, Stevens Institute of Technology.
- Stamnes, K., Tsay, S.-C., Wiscombe, W., Jayaweera, K., 1988. Numerically stable algorithm for discrete-ordinate-method radiative transfer in multiple scattering and emitting layered media. *Appl. Opt.* 27 (12), 2502.
- Toledano, C., Cachorro, V.E., Berjon, A., de Frutos, A.M., Sorribas, M., de la Morena, B.A., Goloub, P., 2007. Aerosol optical depth and Ångström exponent climatology at El Arenosillo AERONET site (Huelva, Spain). *Q. J. Roy. Meteor. Soc.* 133 (624), 795–807.
- Valks, P., Loyola, D., Hao, N., Rix, M., 2011. Algorithm theoretical basis document for GOME-2 total column products of ozone, minor trace gases and cloud properties. Tech. Rep. DLR/GOME-2/ATBD/01, German Aerospace Center.
- Vasiliki, P., Norton, M., Hadjipanayi, M., Georghiou, G., 2013. Calibration of spectroradiometers for outdoor direct solar spectral irradiance measurements. *Proc. 28th European Photovoltaic Solar Energy Conference and Exhibition*, Paris, France, pp. 3466–3471.
- WDC, 2015. Global ozone monitoring experiment GOME-2 <https://wdc.dlr.de/sensors/gome2/> (accessed: 2015-05-25).
- Weihs, P., Webb, A., 1997. Accuracy of spectral UV model calculations: 1. Consideration of uncertainties in input parameters. *J. Geophys. Res. Atmos.* 102, 1541–1550.
- Xia, X., Chen, H., Goloub, P., Zhang, W., Chatenet, B., Wang, P., 2007. A compilation of aerosol optical properties and calculation of direct radiative forcing over an urban region in northern China. *J. Geophys. Res. Atmos.* 112, D12203.
- Yoon, H., Gibson, C., 2011. NIST Special Publication 250-89 NIST measurement services: spectral irradiance calibrations.

6.6 Publication VI

Uncertainty analysis of a radiative transfer model using Monte Carlo method: impact on PV device calibration parameters

Giorgio Belluardo, Grazia Barchi, Dietmar Baumgartner, Marcus Rennhofer, Philipp Weihs, David Moser

*Proceedings of the OTTI's 31st Symposium Photovoltaic Solar Energy.
Bad Staffelstein, Germany, 2016*

Uncertainty analysis of a radiative transfer model using Monte Carlo method: impact on PV device calibration parameters

Giorgio Belluardo, Grazia Barchi, David Moser
Institute for Renewable Energy, EURAC Research, Viale Druso 1, 39100 Bolzano
Tel.: +39 471 055626, Fax: +39 471 055699
E-Mail: giorgio.belluardo@eurac.edu
Internet: www.eurac.edu

Dietmar Baumgartner
Kanzelhöhe Observatory for Solar and Environmental Research, University of Graz,
Kanzelhöhe 19, 9521 Treffen am Ossiacher See

Marcus Rennhofer
Energy Department, AIT Austrian Institute of Technology GmbH, Giefinggasse 2,
1210 Vienna

Philipp Weihs
Institute of Meteorology, University of Natural Resources and Life Sciences, Peter-
Jordan-Straße 82, 1190 Vienna

Abstract

Many tools implementing Radiative Transfer Equation solvers are used nowadays for the calculation of spectral irradiance. Although many studies proved their accuracy, few of them exist that focus on the uncertainty of these models. This study evaluates how the uncertainty of the input parameters of Radiative Transfer solver SDISORT propagates into the generated spectra and how this in turn affects the uncertainty of two photovoltaic (PV) device calibration parameters: short circuit current (I_{sc}) and spectral mismatch factor (MM). In particular, both the propagation of single input parameter uncertainty and of their combination are evaluated, as well as the definition of possible maximum and minimum uncertainty levels referring to input combinations that differ from a defined reference set.

The analysis considers the spectral range 280 nm - 2500 nm and the spectral response of seven different photovoltaic technologies. Monte Carlo technique is used as a statistical method for evaluating uncertainty propagation, by assuming a rectangular probability density function of SDISORT input parameters as well as defined uncertainty levels. Results show that the lowest uncertainty variability occurs for mono-crystalline silicon technology (2.94% to 7.74% for I_{sc} and 0.01% to 2.13% for MM), the highest for organic technology (2.94% to 14.54% for I_{sc} and 0.01% to 9.45% for MM).

1. Introduction

Solar spectral and broadband simulation models are useful and important tools for the solar energy sector. They are mostly employed to calculate solar information at a specific site or region, and due to their fast computation time they can also retrieve long time series of data. For this reason, their application is manifold. For example, simulation of solar irradiance is useful when no sensor is installed or when there is a gap in measurement records. This is true in particular for solar spectra, since spectroradiometers are not so widespread due to the difficulty of instrument setting-up, maintenance and costs. On the other hand, simulations of spectral irradiance can be used to validate measurements (Belluardo et al., 2014; Marzo and Ballestrin, 2010).

Nowadays many simulation software are available. They differ on the spectral region resolved, computation algorithm, geometrical schematization, licence type etc. An overview and classification of the most commonly used tools is given by Myers (2005) and by Seidel et al. (2010). The accuracy of these tools has been assessed by many authors by comparing simulation results of both spectral and broadband irradiance with measurements taken in different Earth regions. In general, most of them have proven to be enough accurate, especially under clear-sky conditions.

Simulation tools can assess solar resource both in quantitative and qualitative terms. In the first case, they allow to calculate the solar resource of a specific place up to a specific region. They can be therefore involved in specific solar energy projects (design and production forecast of a future PV system), they can help understanding the actual performance of a PV system where irradiance sensor is not available, they can support policy makers and stakeholders in decisions concerning the energy development of a district up to a region. When spectral information is retrieved, spectral effects on PV systems can be assessed. This way the spectral behavior of a specific PV technology is fully characterized, and consequently corrections can be applied in PV modelling, e.g. for the accurate estimation of PV system degradation (Belluardo et al., 2015).

It is therefore clear that tools for the simulation of solar irradiance are fully part of the PV energy conversion chain. Being the bankability of solar energy projects strictly dependent upon a reliable and accurate assessment of every step of energy conversion, it is important to correctly estimate their uncertainty. Unfortunately, at the authors' knowledge few authors focused on this topic. On the other hand, many studies have focused on the uncertainty assessment of the input parameters used in these tools. The aim of the first part of this study is therefore to calculate the uncertainty of spectral and broadband irradiance generated with one common radiative transfer model. The approach is the one used by Cordero et al. (2007) that involves Monte Carlo statistical technique: the output uncertainty due to the effect of a single input parameter or of the combination of more input parameters is evaluated by calculating statistics on a series of $N \gg 1$ randomly generated spectra. The analysis performed by Cordero et al. (2007) on the UV spectral range (280 nm to 400 nm) is here broadened to 2500 nm in order to include a) sensitivity regions of all photovoltaic technologies (those concurring to the generation of current) and b) sensitivity regions of the available spectroradiometers, in order to compare results with uncertainty from spectral measurements.

In a second part, the propagation of uncertainty to PV device calibration factors, such as short circuit current (I_{sc}) and spectral mismatch factor (MM), is assessed. For this reason, seven different photovoltaic technologies are considered, whose spectral response has been measured in laboratory: monocrystalline (mc-Si) and polycrystalline (pc-Si) Silicon, double junction amorphous Silicon (a-Si), Copper Indium Gallium Selenide (CIGS), Cadmium Telluride (CdTe), organic cell (organic) and Copper Zinc Tin Sulfide (CZTS).

2. Methodology

2.1 The Radiative Transfer Equation solver SDISORT

The propagation of solar electromagnetic radiation to Earth's surface is described in mathematical terms by the Radiative Transfer Equation (RTE). This equation accounts for all interactions, such as scattering, absorption and emission, occurring between sunlight and Earth's atmospheric constituents.

RTE can be analytically solved only in a restricted number of simplified cases. In most of the cases a numerical approach, such as discrete ordinate method, is applied for its solution indeed. Many tools exist that implement RTE numerical solvers. In some cases, these tools are physically based and can be solved either line-by-line or by applying some simplifications in the algorithm to speed the computation up. In other cases, RTE is substituted with a parametrization in order to result much faster. In this study, the pseudospherical version of the Discrete Ordinates Radiative Transfer Program for a Multi-Layered Plane-Parallel Medium (DISORT), namely SDISORT (Dahlback and Stamnes, 1991), implemented in the UVSPEC tool (Kylling, 1992) and included in the libRadtran software package (Mayer and Kylling, 2005), is used as solar spectral simulation tool. Nine different atmospheric parameters are selected as input, as they are widely recognized as being the ones influencing solar spectral results at most: extraterrestrial spectrum (S), solar zenith angle (θ), surface albedo (A), ozone column (o), water vapor (w), Ångström exponent (α), Ångström turbidity coefficient (β), aerosol single scattering albedo (ω), aerosol asymmetry factor (g). An exhaustive description of them can be found in Smith (1985). The site Kanzelhöhe Observatory (N 46.678°, E 13.907°, altitude 1526 m a.s.l.) is selected as reference place for the retrieval of input parameters, while the solar spectrum measured with a EKO MS-710 spectroradiometer at 10:00 (UTC time) on 25th April, 2013 is taken as the reference measurement. The selection of the reference time derives from a high level of quality of data available for the site at that moment, especially for aerosol information, and for the clear-sky conditions on that whole day.

The values of SDISORT input parameters describing the atmospheric state at Kanzelhöhe Observatory at the moment of reference measurement, as well as their source, are reported in Table 1. In particular, the aerosol information is retrieved from measurements performed with a CIMEL sunphotometer available at the site, and part of the NASA's AERONET network. In fact, as demonstrated by Belluardo et al. (2014), spectral simulations performed with high quality data of aerosol from AERONET database are more accurate than simulations that use satellite-retrieved aerosol as input.

SDISORT model output consists in spectra of global horizontal irradiance (GHI), diffuse horizontal irradiance (DiffHI), and direct horizontal irradiance (DirHI). In particular, the GHI spectrum simulated with SDISORT using reference values of input parameters as in Table 1 has been compared with the reference spectrum measured in the range 350 nm - 900 nm. Figure 1 shows that the difference between simulated and measured spectrum, divided by the peak in measured spectrum, is mostly within $\pm 5\%$. The broadband irradiance value (integral value of the spectrum) results 611.4 W/m² for measured spectrum and 606.7 W/m² for simulated spectrum, while the corresponding Mean Absolute Error (MAE), Mean Bias Error (MBE) and Root Mean Square Error (RMSE) are, respectively, -8.7 W/m², 31.5 W/m² and 39.5 W/m².

Table 1: Reference set of input parameters for SDISORT model, and their source. Values refer to 10:00 (UTC0 time) on April 25th, 2013 at Kanzelhöhe Observatory site.

Parameter	Ref. value	Source
extraterrestrial spectrum (S)	-	Gueymard (2004)
solar zenith angle	35.85°	NREL (2015)
surface albedo	0.12	CMSAF (2015)
ozone column	321.27 DU	WDC (2015)
water vapor	7.43 mm	NASA (2015)
Ångström exponent	1.13	NASA (2015)
Ångström turbidity coefficient	0.025	NASA (2015)
aerosol single scattering albedo	0.99	NASA (2015)
aerosol asymmetry factor	0.67	NASA (2015)

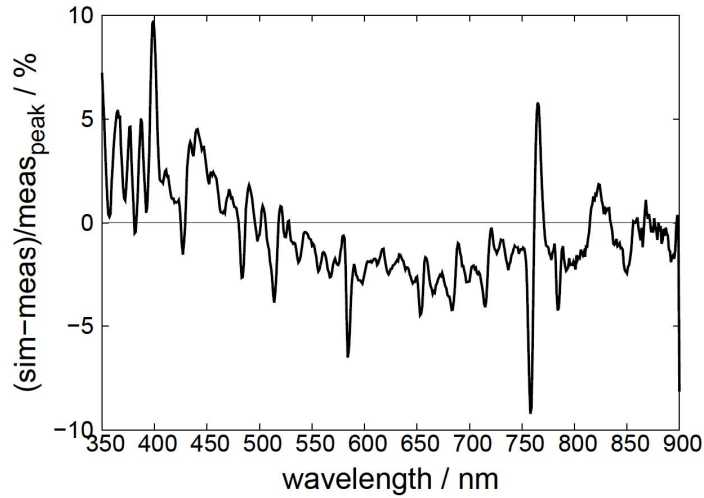


Figure 1: Relative difference between the solar spectrum measured with an EKO MS-710 spectroradiometer at 10:00 (UTC0 time) on April 25th, 2013 at Kanzelhöhe Observatory site and the solar spectrum simulated with SDISORT using the reference set of input parameters as in Table 1. Only the range 350 nm - 900 nm is displayed, corresponding to the spectroradiometer sensitivity range.

2.2 Monte Carlo method for uncertainty propagation

If we consider a measurement q of the quantity Q , and suppose to repeat the measurement under repeatability conditions, the dispersion of measurements around an average value is described by the Probability Density Function (PDF) of Q . If PDF is known, then the calculated standard deviation corresponds to the standard uncertainty of Q (GUM - JCGM 100:2008, 2008). In the same way, if we see SDISORT as a model $Q = M(\mathbf{P})$ where $\mathbf{P} = (P_1, P_2, \dots, P_{N_{par}})$ is the vector of N_{par} input quantities, it is possible to calculate its standard uncertainty once the model's PDF is reconstructed.

If the model $Q = M(\mathbf{P})$ is linear or nonlinear, but differentiable, the standard uncertainty of Q can be obtained from the law of propagation of uncertainty (GUM - JCGM 100:2008, 2008). This turns to be a difficult task when the model is nonlinear and not differentiable, such in the case of Radiative Transfer Equation. In this case, the Monte Carlo method is more appropriate. The Monte Carlo technique consists in determining the PDF of Q in a numerical way, by making random draws from the PDFs of the input quantities, and evaluating the model at the resulting values. In other words, Monte Carlo allows to reconstruct the PDF of Q starting from information on the PDF of all input quantities.

Given a generic value of one input parameter derived from meteorological or climatological measurements, it is actually not possible to reconstruct its PDF, since measurements cannot be performed under repeatability conditions. In this case, a suitable PDF can be assigned according to the principle of maximum entropy (GUM - JCGM 101:2008, 2008), i.e. by selecting one of the most probable PDFs among those which comply with the restrictions imposed by the available information. In our case, for a single measured value p_j of the input quantity P_j , an error bound d_j that corresponds to the maximum error reasonably attributed to p_j is chosen based on experience or from literature. As demonstrated by Cordero et al. (2007), when only the error bound information is available, the most probable PDF is rectangular distribution over the interval $(p_j - d_j, p_j + d_j)$, i.e. a distribution that associates the same probability to all values in the considered interval.

Once the PDF shape, the error bound and a single measured value (e.g. the reference value) are known for each input parameter, it is possible to perform $N \gg 1$ draws, i.e. to generate $N \gg 1$ values of each input parameter. In our case the free software *Statistics101* implementing the Monte Carlo algorithm (Grosberg, 2015) is used and a number of $N = 500$ draws is assumed sufficient for the analysis. The generated values are combined in $N = 500$ input vectors and fed into SDISORT. In particular, there are two ways of creating input vectors:

- Option 1: if we are interested in evaluating the influence of uncertainty of a specific input parameter to the model's output uncertainty, only the values of this input parameter change within the input vector, while the values of the other input parameters are kept equal to their reference value
- Option 2: if we are interested in evaluating how the combination of uncertainty of all N_{par} input parameters affect the model output uncertainty, the values of all input parameters change simultaneously within the input vector.

Once $N = 500$ outputs of GHI spectra are obtained from SDISORT, a statistical analysis is performed. The standard deviation u_G , the mean value I_G and the ratio u_G/I_G of the pool of $N = 500$ spectral irradiance values at each wavelength between 280 nm and 2500 nm are calculated. The first of the mentioned quantities corresponds to the standard uncertainty (or absolute uncertainty, expressed in $W/m^2/nm$), the latter to the relative standard uncertainty (expressed as a percentage). In this work the term *relative standard uncertainty* is substituted with the term *uncertainty* for simplification reasons.

2.3 Selection of error bounds

Given an input parameter, the associated error bound corresponds to the maximum variation of input value with respect to the corresponding reference value listed in Table 1, under hypothetical repeatability conditions. The error bound strictly depends upon the characteristics of the measurement instrument and method, and not simply from the temporal variability of the associated measured values. For this reason, it can be derived either from previous studies or from experience. In our case we applied a security factor to values of uncertainty available in literature, provided that the data type, the measurement instruments and the boundary conditions (for example, some values of uncertainty are valid at specific ranges of solar zenith angle or are associated to other specific atmospheric conditions) are ascribable to our case. The set of selected error bounds and the literature source for input uncertainties are reported in Table 2.

Table 2: Error bounds associated to the input parameters measured at 10:00 on April 25th, 2013 at Kanzelhöhe Observatory site, and listed in Table 1. Literature sources used as reference for their derivation are also reported.

Parameter	Ref. value	Source
S	5%	Gueymard (2004)
θ	0.03°	NREL (2015)
A	25%	Xia et al. (2007)
o	5%	Valks et al. (2011)
w	10%	Holben et al. (2001); Perez-Ramirez et al. (2014)
α	0.08	Schuster et al. (2006); Toledano et al. (2007)
β	0.025	Holben et al. (1998); Eck et al. (2001)
ω	0.05	Dubovik et al. (2000)
g	0.05	Xia et al. (2007); Andrews et al. (2006)

2.4 PV device calibration factors

Once $N = 500$ outputs of GHI spectra are obtained from SDISORT using the methodology described in Section 2.2, a statistical analysis can be performed on any parameter that can be derived from the spectra. In this study we focus in particular on two parameters related to the PV device calibration: the short circuit current, or photocurrent, (I_{sc}) and the spectral mismatch factor (MM). The short circuit current is expressed by Equation 1. This is the most common expression used to model the photovoltaic conversion of incoming spectrally resolved irradiance $GHI_{sim}(\lambda)$ - in this case simulated - into photocurrent $I_{sc_{dut}}$, performed by a PV device characterized by spectral response $SR_{dut}(\lambda)$ and area.

$$Isc_{dut} = Area \cdot \int_{280}^{2500} GHI_{sim}(\lambda) SR_{dut}(\lambda) d\lambda$$

Spectral mismatch factor is used to correct the results of the Isc simulation to the spectral conditions of Standard Test Conditions STC, i.e. to the standard spectrum AM1.5:

$$MM = \frac{\int_{280}^{2500} GHI_{ref}(\lambda) d\lambda}{\int_{280}^{2500} GHI_{sim}(\lambda) d\lambda} \cdot \frac{\int_{280}^{2500} GHI_{sim}(\lambda) SR_{dut}(\lambda) d\lambda}{\int_{280}^{2500} GHI_{ref}(\lambda) SR_{dut}(\lambda) d\lambda}$$

This becomes:

$$MM = \frac{992.6 W/m^2}{GHI_{sim}} \cdot \frac{Isc_{dut}}{Isc_{ref}}$$

Seven PV devices characterized by different material technology have been considered in this study: monocrystalline (mc-Si) and polycrystalline (pc-Si) Silicon, double junction amorphous Silicon (a-Si), Copper Indium Gallium Selenide (CIGS), Cadmium Telluride (CdTe), organic cell (organic) and Copper Zinc Tin Sulfide (CZTS). Their spectral response has been measured in laboratory, and is reported in Figure 2. SR measurement is obviously affected by a value of uncertainty, but it has been neglected in this study in order to isolate the only uncertainty ascribable to spectral simulation model SDISORT. This has been done also for the uncertainty of the AM1.5 standard spectrum.

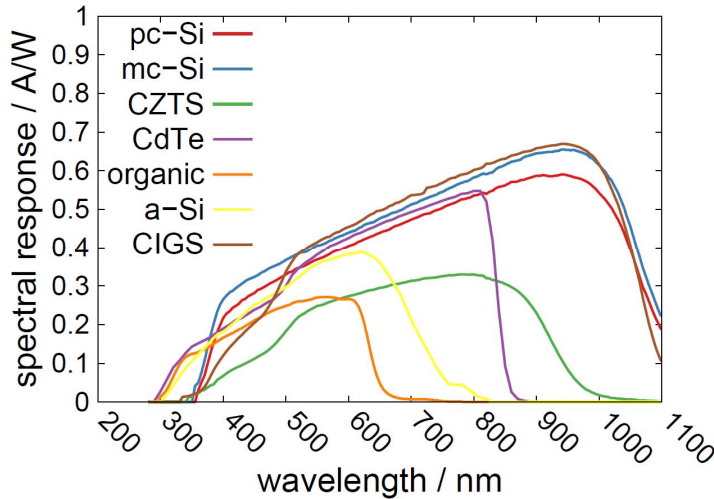


Figure 2: Spectral Response of the seven investigated PV technologies, measured in laboratory. pc-Si: polycrystalline Silicon, mc-Si: monocrystalline Silicon, CZTS: Copper Zinc Tin Sulfide, CdTe: Cadmium Telluride, organic: organic cell, a-Si: double junction amorphous Silicon, CIGS: Copper Indium Gallium Selenide.

3. Simulation results

3.1 Analysis of SDISORT uncertainty contributors

The methodology described in Section 2.2 is applied to the set of reference input values reported in Table 1, and using the error bound as in Table 2. In a first instance Option 1, corresponding to the generation of input vectors by changing the values of one input parameter at a time, is followed in order to study the contribution of the uncertainty of each considered input parameter to the model output uncertainty. Results are displayed in Figure 3. Plots on the left show the whole spectral range 280 nm - 2500 nm and is useful to identify the major contributors in the VIS, NIR and SWIR regions, while plots

on the right are scaled in order to focus on the UVB and UVA parts. The combined effect of uncertainty propagation of all input parameters to model output (Option 2) is also reported in black line. The contributions to SDISORT uncertainty on GHI irradiance is different depending on the input parameter. The effect of extraterrestrial spectrum on uncertainty propagation is constant for the whole spectral range, and results in 2.95% for the broadband irradiance. The influence of Ångström turbidity coefficient is more evident in the UV region, with a local spectral uncertainty peak of around 1.4%, while it decreases at increasing wavelengths, with local peaks at water absorption bands. Focusing on the short-wavelength region, the influence of ozone on uncertainty propagation affects only the UVB region, where it varies locally from around 110% to 4%. Nevertheless, the effect of the uncertainty of this atmospheric gas on the whole spectral range is negligible. Finally, water vapor is an important source of uncertainty at water absorption bands, especially in the range 1350 nm - 1425 nm and 1800 nm - 1950 nm, where the value of spectral uncertainty can be higher than 10%. The uncertainty of broadband GHI due to the simultaneous propagation of input parameters uncertainty is 3%.

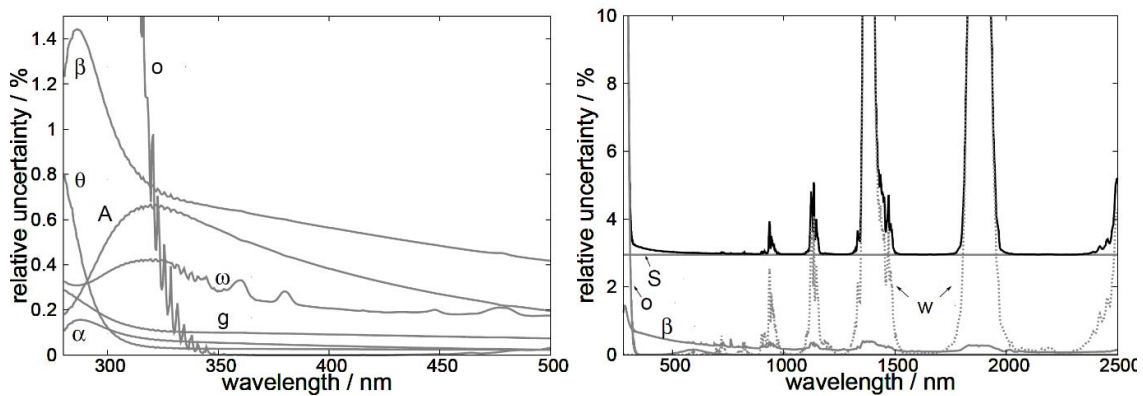


Figure 3: Relative uncertainty of the SDISORT output at varying wavelength, due to the uncertainty of each input parameter and to the combined effect of all input parameters, for GHI. Uncertainty due to combined effect is in black. (left) view of the whole investigated spectral range (right) zoom on the UV part of the spectrum. S: extraterrestrial spectrum, θ : solar zenith angle, A: surface albedo, α : ozone column, w: water vapor, α : Ångström exponent, β : Ångström turbidity coefficient, ω : aerosol single scattering albedo, g: aerosol asymmetry factor.

3.2 Uncertainty limits for spectral irradiance

The set of input parameters displayed in Table 1 is of course not representative of all possible combinations occurring at Kanzelhöhe Observatory or in another location. It is therefore interesting to assess the uncertainty related to other sets of input parameters, and in particular the ones corresponding, respectively, to the minimum and to the maximum possible level of uncertainty. Therefore, different values are assigned to each input parameter on the base of a specific step, and simulations are ran in which one input parameter at a time varies according to the error bounds assigned in Table 2, while assigning reference values to the remaining ones (Option 1 described in Section 2.2). For each input parameter, the values corresponding to the minimum and to the maximum single contribution to the uncertainty of model-generated broadband GHI are selected to compose two new sets of input values, i.e. two new input vectors. This way, the resulting uncertainties due to the simultaneous propagation of input parameters' uncertainty very likely approximate the minimum and the maximum possible uncertainty that can be associated to the assigned error bounds. This assumption is not entirely correct, since some constructive or destructive interferences may occur in the simultaneous propagation of uncertainties of two or more correlated parameters. Anyway, it is reasonably expected that the two input vectors well approximate the minimum and maximum possible uncertainty. Table 3 shows, in addition to the selected steps used for the simulations, the values of input parameters that

correspond respectively to the minimum and to the maximum output calculated uncertainty, and the values of uncertainties themselves. The spectral uncertainty limits due to the combined effect of input parameters' uncertainty are reported in Figure 4, together with the spectral uncertainty due to simultaneous effect of reference input parameters, calculated in Section 3.1. SDISORT uncertainty of broadband GHI in the investigated range 280 nm - 2500 nm ranges between a minimum of 2.9% and a maximum of 5.9%. It is interesting to notice that the latter value is higher than the value obtained from a simple sum of squares of the single uncertainties ascribable to each input parameter (equal to 3.1%), thus confirming once more the suitability of Monte Carlo to such a kind of analysis. The obtained range of uncertainty can be compared with the uncertainty of spectra measured with spectroradiometers. The latter is a combination of instrument calibration uncertainty (a calculation and a summary of calibration uncertainties of spectroradiometers from different research institutes is given by Galleano et al. (2014)) and of repeatability of measurement performed outdoor, plus other factors depending by the instrument itself and the measurement setup. For example, Vasiliiki et al. (2013) calculate a combined standard uncertainty of 2.5% ($k=1$) for outdoor spectral measurements of the global normal irradiance (GNI). This value is lower but still comparable with the uncertainty calculated in this study. Furthermore, the gradual improvement of instruments and procedures for the retrieval of RTM input parameters looks promising and will push towards a reduction of uncertainty levels.

Table 3: Selected ranges of values for each considered input parameter, and values corresponding to maximum and minimum output broadband uncertainty for broadband GHI, respectively. Corresponding values of output uncertainty are displayed into brackets.

Parameter	min-max value, step	min value (unc.)	max value (unc.)
S	-	nd (2.95%)	nd (2.95%)
θ	10°-70°, 10°	10° (0.01%)	70° (0.10%)
A	0.05-0.95, 0.10	0.05 (0.05%)	0.75 (0.91%)
o	250-500DU, 25DU	250DU (0.03%)	500DU (0.05%)
w	5mm-50mm, 5mm	0 (0.00%)	50 (0.32%)
α	0.5-2.5, 0.25	0.5 (0.01%)	2.5 (0.04%)
β	0-0.5, 0.05	0 (0.16%)	0.5 (0.36%)
ω	0.6-1, 0.05	1 (0.12%)	0.6 (0.14%)
g	0.5-0.9, 0.05	0.9 (0.04%)	0.5 (0.06%)

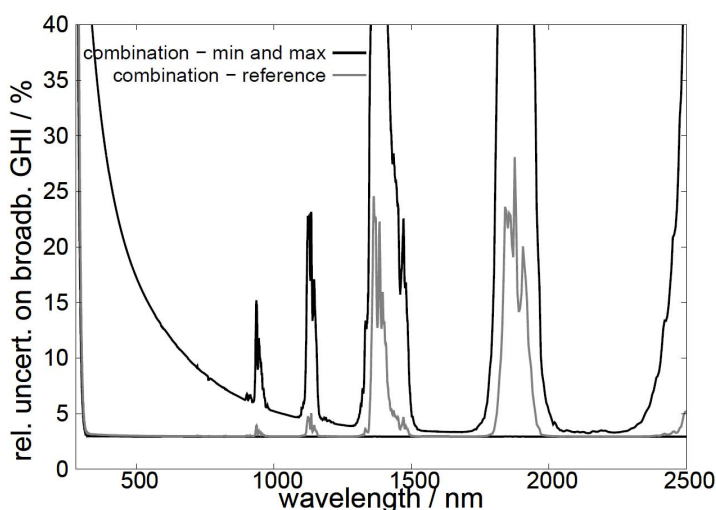


Figure 4: Max and min relative spectral uncertainty of the SDISORT outputs for GHI due to the combination of input parameters generating, respectively, the highest and lowest uncertainty, and with values of error bounds as defined in Table 2. Output spectral uncertainty from the reference set of input parameters as in Table 1 is also displayed.

3.2 Uncertainty propagation to PV device calibration factors

Results presented in the previous sections concern the uncertainty of solar spectral and broadband irradiance simulated with SDISORT. In this section the propagation of this uncertainty to PV device calibration factors I_{sc} and MM is analyzed. First of all, the uncertainty values of I_{sc} and MM ascribable to both the uncertainty of each model input parameter and to their simultaneous propagation is reported. The analysis is repeated for each of the seven investigated PV technologies and focus is put also on the uncertainty behavior in the spectral regions involved (UVB, UVA, VIS and NIR). Finally, uncertainty limits are calculated in order to account for any possible combination of input parameter different from the reference set of Table 1.

Table 4 shows the uncertainty of parameters I_{sc} and MM due to the propagation of the uncertainty value of every SDISORT input parameter. The uncertainty associated to the simultaneous propagation of input parameters uncertainty is also reported in italics. The latter does not change significantly amongst technologies, and is around 3%. Focusing on single uncertainty contributions, the highest one is ascribable to extraterrestrial spectrum, that alone accounts for a 2.95% uncertainty and is the same for all technologies. Technologies with SR more shifted towards lower wavelengths - and in particular sensitive at wavelengths lower than 330 nm such as organic, a-Si and CdTe - are associated to the highest values of uncertainty ascribable to surface albedo A , ozone column o , Ångström turbidity coefficient β and single scattering albedo ω . This result is explained by Figure 5, that shows the contribution to I_{sc} uncertainty deriving from uncertainty propagation of every single input parameter, for each spectral region and for each investigated technology. It is clear that the propagation of input parameters uncertainty in the UVB region has an effect only on technologies which are sensitive at that wavelengths, and is in general more pronounced than in other spectral regions.

Table 4: Uncertainty of the PV device calibration factors I_{sc} and MM calculated using spectral irradiance computed with SDISORT (values in percentage). Both the contribution of single input parameter's uncertainty and of their combination (in italics) are reported. S : extraterrestrial spectrum, θ : solar zenith angle, A : surface albedo, o : ozone column, w : water vapor, α : Ångström exponent, β : Ångström turbidity coefficient, ω : aerosol single scattering albedo, g : aerosol asymmetry factor.

Parameter	I_{sc}									
	S	θ	A	o	w	α	β	ω	g	Simult. effect
mc-Si	2.95	0.02	0.1	0.03	0.11	0.01	0.31	0.13	0.06	2.98
pc-Si	2.95	0.02	0.1	0.03	0.11	0.01	0.3	0.13	0.06	2.98
a-Si	2.95	0.02	0.17	0.07	0.02	0.02	0.38	0.17	0.07	3.00
CIGS	2.95	0.02	0.09	0.04	0.11	0.01	0.29	0.13	0.06	2.98
CdTe	2.95	0.02	0.13	0.05	0.04	0.02	0.34	0.15	0.06	2.99
organic	2.95	0.02	0.21	0.07	0.01	0.02	0.42	0.18	0.07	3.01
CZTS	2.95	0.02	0.11	0.05	0.07	0.01	0.31	0.14	0.06	2.99
Parameter	MM									
	S	θ	A	o	w	α	β	ω	g	Simult. effect
mc-Si	<0.01	<0.01	0.02	<0.01	0.08	<0.01	<0.01	<0.01	<0.01	0.08
pc-Si	<0.01	<0.01	0.02	<0.01	0.08	<0.01	<0.01	<0.01	<0.01	0.08
a-Si	<0.01	<0.01	0.05	0.03	0.16	0.01	0.08	0.04	0.01	0.19
CIGS	<0.01	<0.01	0.03	<0.01	0.07	<0.01	0.01	<0.01	<0.01	0.08
CdTe	<0.01	<0.01	0.01	0.01	0.14	<0.01	0.03	0.02	0.01	0.15
organic	<0.01	<0.01	0.09	0.03	0.17	0.01	0.11	0.05	0.02	0.23
CZTS	<0.01	<0.01	0.02	0.01	0.11	<0.01	0.01	0.01	<0.01	0.11

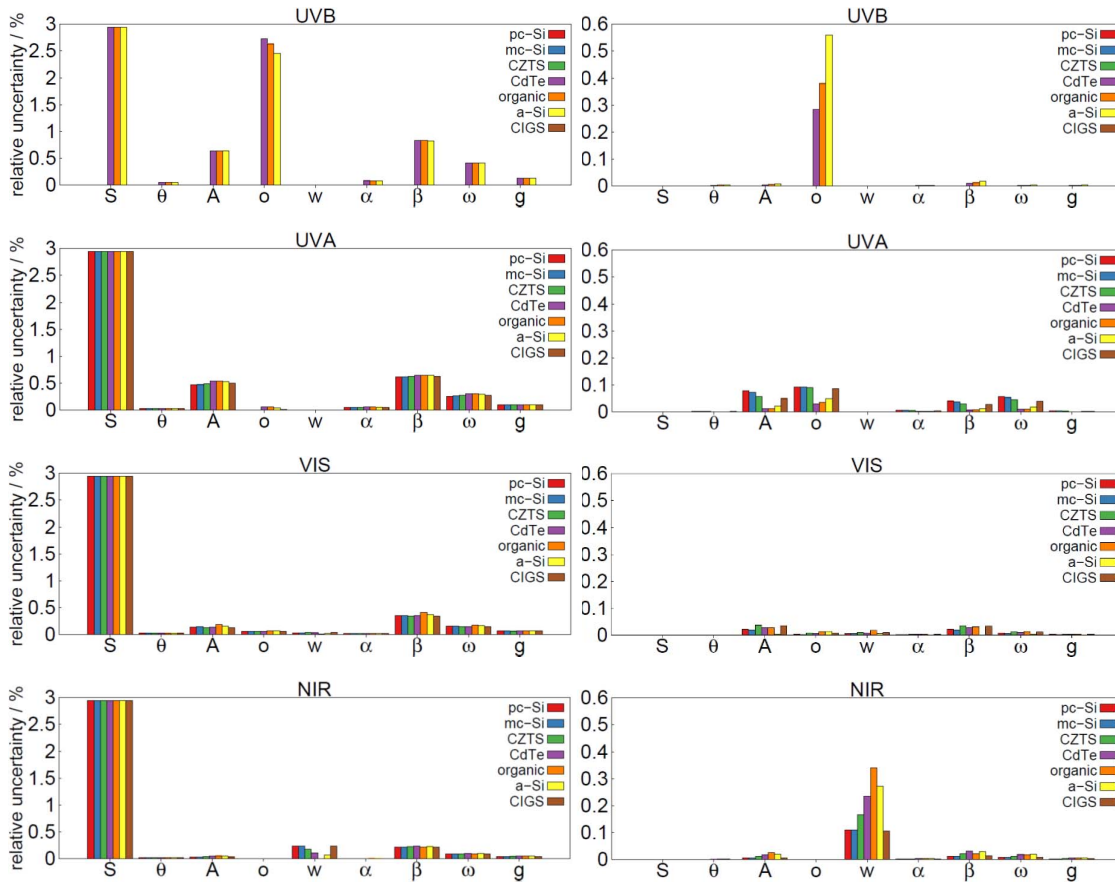


Figure 5: Contribution to the uncertainty of the PV device calibration factors I_{sc} (left) and MM (right) propagating from each SDISORT input parameter, for each investigated technology and for each spectral region.

On the other hand, technologies with a narrower SR are less affected by the uncertainty of precipitable water with respect to technologies with broader SR, such as mono- and poly-crystalline silicon and CIGS. This is due to the fact that the sensitivity region of these technologies includes several absorption bands of precipitable water. This is confirmed by Figure 5, that shows that the major uncertainty contribution of precipitable water's uncertainty is in the NIR part of the spectrum, and is higher for mc-Si, pc-Si and CIGS while lower, or even null, for the other technologies.

Different uncertainty values and distributions result for spectral mismatch factor MM . The contribution of extraterrestrial spectrum uncertainty is null. In fact, as shown in Equation 3, being $I_{sc,ref}$ constant and therefore not contributing to the overall uncertainty, the only uncertainty contributions derive from $I_{sc,dut}$ and GHI_{sim} . In the case of extraterrestrial spectrum, whose uncertainty in both $I_{sc,dut}$ and GHI_{sim} is the same for all wavelengths, uncertainties cancel out. As for other input parameters, such as surface albedo A , ozone column o , Ångström turbidity coefficient β and single scattering albedo ω , the values of uncertainty are lower than in I_{sc} case but characterized by the same trend previously seen: higher values for technologies sensitive in the UVB region (organic, a-Si, CdTe), lower values for technologies sensitive at wavelengths higher than 330 nm and with broader SR (mc-Si, pc-Si, CIGS). As shown in Figure 5, in this case the major contribution of the uncertainty of these input parameters is in the UVA region rather than in the UVB region, with the sole exception of ozone column uncertainty.

The same Figure shows that in the NIR region most of the uncertainty contribution is given by precipitable water uncertainty. In particular, a different behavior than in the I_{sc} case is visible. Higher uncertainty values concern technologies that are sensitive in the UVB region and have a narrower SR,

and therefore are supposed to include a lower portion of water absorption bands. It is reasonable to suppose that some interferences come into play when precipitable water uncertainty propagates into the components of Equation 2 defining MM. The consequence of such a behavior is that MM uncertainty due to the simultaneous propagation of input parameters uncertainty is more variable amongst technologies, in relative terms. In fact, despite the values are much lower than in I_{sc} case (they range from 0.08% for mc-Si, pc-Si and CIGS and 0.23% for organic), there is a higher variability than in I_{sc} case. This is explained by the fact that in this case precipitable water uncertainty contribution to MM uncertainty follows the same trend as for other input parameters, instead of counteracting them as in the case of I_{sc} .

Table 5: Minimum and maximum levels of uncertainty of the PV device calibration factors I_{sc} and MM due to the simultaneous propagation of uncertainty from SDISORT input parameters (values in percentage).

	I_{sc}		MM	
	min	max	min	max
mc-Si	2.94	7.74	0.01	2.13
pc-Si	2.94	7.77	0.01	2.16
a-Si	2.94	12.38	0.03	7.16
CIGS	2.94	7.76	0.01	2.14
CdTe	2.94	10.00	0.01	4.61
organic	2.94	14.54	0.04	9.45
CZTS	2.94	9.04	0.01	3.56

This analysis, and the resulting values of uncertainty, concerns the propagation of uncertainty defined with error bounds as in Table 2 and reference values of input parameters as in Table 1. As in the case of spectral and broadband irradiance, it is interesting to study how the deviation of input parameters values from the reference set influence the simultaneous propagation of uncertainty to PV device calibration factors I_{sc} and MM. Therefore, the same methodology described in Section 3.2 has been applied in order to construct input vectors associated to minimum and maximum levels of I_{sc} and MM uncertainty. All possible combinations of input parameters ranging between the limits reported in Table 3 are very likely to lie between them.

Results are reported in Table 5. Compared with the maximum limit of 5.9% of the uncertainty of broadband irradiance found in Section 3.2, the maximum limits of I_{sc} are higher for all investigated technologies. Therefore, the uncertainty tends to amplify when propagating to this parameter. As for MM, the maximum limits are higher than 5.9% only for a-Si and organic, thus confirming that in the propagation of uncertainty to this parameter some contributions cancel out or destructively interfere. In general, mc-Si presents the narrowest uncertainty limits, ranging from 2.94% to 7.74% for I_{sc} and from 0.01% to 2.13% for MM. On the other hand, organic technology has the broadest uncertainty limits, ranging from 2.94% to 14.54% for I_{sc} and from 0.04% to 9.45% for MM.

4. Conclusions

This paper presents an analysis of the uncertainty propagation from the input parameters of SDISORT radiative transfer model to spectral and broadband simulated irradiance. The uncertainty of PV device calibration factors short circuit current I_{sc} and spectral mismatch factor MM of seven different photovoltaic technologies is also assessed. The study focuses of the range 280 nm - 2500 nm in order to include the spectral response SR of all PV technologies and of all available commercial spectroradiometers. Being the general law of error propagation not applicable due to the nondifferentiable and nonlinear nature of the Radiative Transfer Equation implemented in SDISORT, the statistical method Monte Carlo has been applied. A set of reference values of SDISORT input

parameters describing the atmospheric state above Kanzelhöhe Observatory (Austria) site at 10:00 on April 25th, 2013 has been defined, as well as the values of the associated error bounds.

As for the uncertainty of spectral and broadband irradiance, one of the major contributions derive from ozone column, especially in the UVB region (280 nm - 315 nm), with a local peak reaching some 110%. Extraterrestrial spectrum contributes for 2.95% of output uncertainty on the whole spectral range. Other contributions come from Ångström exponent β , with a peak of 1.4% in the UVB region, gradually degrading at higher wavelengths. Finally, uncertainty due to water vapor results in local peaks higher than 10% at absorption bands, especially between 1350 nm - 1425 nm and 1800 nm - 1950 nm. Under the reference set of input parameters, the uncertainty of broadband irradiance generated with SDISORT is 3%.

Considering all possible combinations of input parameters within defined limits, and assuming the same set of error bounds initially defined, it is possible to conclude that the uncertainty of broadband uncertainty simulated with SDISORT and deriving from the simultaneous propagation of uncertainty of all input parameters is between 2.9% and 5.9%. This range is higher, but still comparable to typical uncertainty values of global irradiance measurements performed with spectroradiometers.

The propagation of uncertainty from spectral irradiance to PV device calibrations factors has some similarities and some differences amongst I_{sc} and MM. In the case of I_{sc} , the uncertainty tends to increase independently from the considered technology. In the case of MM, the same trend is verified only for a-Si and organic technologies, characterized by a sensitivity at lower wavelengths (lower than 330 nm) and a narrower SR. As for other technologies, values of uncertainty of MM are actually lower than the uncertainty of spectral irradiance. This is mostly explained by the absence of influence of uncertainty deriving from extraterrestrial spectrum, that cancels out in the propagation to MM. As for the uncertainty limits, I_{sc} uncertainty spans between 2.94% to 7.74% for mc-Si technology and 2.94% to 14.54% for organic technology. Higher variability exists amongst technologies for MM, ranging from 0.01% to 2.13% for mc-Si technology and 0.04% to 9.45% for organic technology. The gradual improvement of instruments and methodologies for the derivation of Radiative Transfer Models input quantities (especially extraterrestrial spectrum and Ångström exponent β) is bound to decrease the associated levels of uncertainty.

In general this study proves that, provided that the uncertainty of every single input parameter is known, the derivation of the output combined uncertainty with a classical propagation of error always underestimates the more realistic values obtained with a more appropriate technique like Monte Carlo, taking the correlation of input parameters into account.

5. Acknowledgements

The authors wish to acknowledge the European Regional Development Fund (ERDF) and the Stiftung Südtiroler Sparkasse for co-financing the project 2-1a-97 "PV Initiative" and the project 5-1a-232 "Flexi-BIPV". The author David Moser wishes to acknowledge the European Union's Horizon 2020 research and innovation programme under grant agreement No 649997, project "Solar Bankability". The author Giorgio Belluardo would like to thank R. Galleano for the fruitful discussion on spectroradiometers uncertainty and T. Eck for the helpful suggestions concerning AERONET data.

6. References

- Andrews, E., Sheridan, P. J., Fiebig, M., McComiskey, A., Ogren, J. A., Arnott, P., Covert, D., Elleman, R., Gasparini, R., Collins, D., Jonsson, H., Schmid, B., Wang, J., 2006. Comparison of methods for deriving aerosol asymmetry parameter. *J. Geophys. Res-Atmos.* 111, D05S04.
- Belluardo, G., Baumgartner, D., Moser, D., Olfes, M., Pravettoni, M., Rennhofer, M., Strepparava, D., Weihs, P., 2014. Solar spectral characterization of three different locations at alpine latitudes using average photon energy. In: ISES, Proc. Eurosun 2014, Aix-les-Bains, France.

- Belluardo, G., Ingenhoven, P., Sparber, W., Wagner, J., Weihs, P., Moser, D., 2015. Novel method for the improvement in the evaluation of outdoor performance loss rate in different PV technologies and comparison with two other methods. *Sol. Energy* 117, 139–152.
- CMSAF, 2015. Surface radiation products. <https://wui.cmsaf.eu/safira/action/viewProduktList?id=2>, accessed: 2015-05-25.
- Cordero, R., Seckmeyer, G., Pissulla, D., Dasilva, L., Labbe, F., 2007. Uncertainty evaluation of the spectral UV irradiance evaluated by using the UVSPEC radiative transfer model. *Opt. Commun.* 276, 44–53.
- Dahlback, A., Stamnes, K., 1991. A new spherical model for computing the radiation field available for photolysis and heating at twilight. *Planet. Space Sci.* 39, 671–683.
- Dubovik, O., Smirnov, A., Holben, B. N., King, M. D., Kaufman, Y. J., Eck, T. F., Slutsker, I., 2000. Accuracy assessments of aerosol optical properties retrieved from aerosol robotic network (AERONET) sun and sky radiance measurements. *J. Geophys. Res-Atmos.* 105, 9791–9806.
- Eck, T. F., Holben, B. N., Dubovik, O., Smirnov, A., Slutsker, I., Lobert, J. M., Ramanathan, V., 2001. Column-integrated aerosol optical properties over the maldives during the northeast monsoon for 1998-2000. *J. Geophys. Res-Atmos.* 106, 28555–28566.
- Galleano, R., Zaïman, W., Virtuani, A., Pavanello, D., Morabito, P., Minuto, A., Spena, A., Bartocci, S., Fucci, R., Leanza, G., Fasanaro, D., Catena, M., 2014. Intercomparison campaign of spectroradiometers for a correct estimation of solar spectral irradiance: results and potential impact on photovoltaic devices calibration. *Progr. Photovolt.: Res. Appl.* 22 (11), 1128–1137.
- Grosberg, J., 2015. Statistics 101 [computer software]. <http://www.statistics101.net/>, accessed: 2015-05-26.
- Gueymard, C. A., 2004. The suns total and spectral irradiance for solar energy applications and solar radiation models. *Sol. Energy* 76 (4), 423–453.
- GUM - JCGM 100:2008, 2008. Evaluation of measurement data guide to the expression of uncertainty in measurement.
- GUM - JCGM 101:2008, 2008. Evaluation of measurement data: Supplement 1 to the guide to the expression of uncertainty in measurement: Propagation of distributions using a Monte Carlo method.
- Holben, B., Tanr, D., Smirnov, A., Eck, T. F., Slutsker, I., Abuhassan, N., Newcomb, W., Schafer, J. S., Chatenet, B., Lavenu, F., Kaufman, Y. J., Vande Castle, J., Setzer, A., Markham, B., Clark, D., Frouin, R., Halthore, R., Karneli, A., O'Neill, N., Pietras, C., Pinker, R., Voss, K., Zibordi, G., 2001. An emerging ground-based aerosol climatology: Aerosol optical depth from aeronet. *J. Geophys. Res-Atmos.* 106, 12067–12097.
- Holben, B. N., Eck, T. F., Slutsker, I., Tanr, D., Buis, J. P., Setzer, A., Vermote, E., Reagan, J. A., Kaufman, Y. J., Nakajima, T., Lavenu, F., Jankowiak, I., Smirnov, A., 1998. AERONETa federated instrument network and data archive for aerosol characterization. *Remote Sens. Environ.* 66 (1), 1–16.
- Kylling, A., 1992. Radiation transport in cloudy and aerosol loaded atmospheres. Ph.D. Thesis, 21.
- Marzo, A., Ballestrin, J., 2010. A realistic test for validate solar spectral measurements. In: *SolarPACES International Symposium on Concentrated Solar Power and Chemical Energy Technologies*, Perpignan, France.
- Mayer, B., Kylling, A., 2005. Technical note: the libRadtran software package for radiative transfer calculations description and examples of use. *Atmos. Chem. Phys.* 5, 1855–1877.
- Myers, D. R., 2005. Solar radiation modeling and measurements for renewable energy applications: data and model quality. *Energy* 30 (9), 1517–1531.

- NASA, 2015. Aerosol robotic network (AERONET). <http://aeronet.gsfc.nasa.gov/>, accessed: 2015-05-25.
- NREL, 2015. Solar position and intensity calculator (SOLPOS). <http://www.nrel.gov/midc/solpos/solpos.html>, accessed: 2015-05-22.
- Perez-Ramirez, D., Whiteman, D. N., Smirnov, A., Lyamani, H., Holben, B. N., Pinker, R., Andrade, M., Alados-Arboledas, L., 2014. Evaluation of AERONET precipitable water vapor versus microwave radiometry, GPS, and radiosondes at ARM sites. *J. Geophys. Res-Atmos.* 119 (15), 2014JD021730.
- Schuster, G. L., Dubovik, O., Holben, B. N., 2006. Ångström exponent and bimodal aerosol size distributions. *J. Geophys. Res-Atmos.* 111, D07207.
- Seidel, F. C., Kokhanovsky, A. A., Schaepman, M. E., 2010. Fast and simple model for atmospheric radiative transfer. *Atmos. Meas. Tech.* 3 (4), 1129–1141.
- Smith, W. L., 1985. *Handbook of applied meteorology*. John Wiley & Sons, New York.
- Toledano, C., Cachorro, V. E., Berjon, A., de Frutos, A. M., Sorribas, M., de la Morena, B. A., Goloub, P., 2007. Aerosol optical depth and Ångström exponent climatology at El Arenosillo AERONET site (Huelva, Spain). *Q. J. Roy. Meteor. Soc.* 133 (624), 795–807.
- Valks, P., Loyola, D., Hao, N., Rix, M., Slijkhuis, S., 2011. Algorithm theoretical basis document for GOME-2 total column products of ozone, minor trace gases and cloud properties. Tech. rep., DLR/GOME-2/ATBD/01, German Aerospace Center.
- Vasiliki, P., Norton, M., Hadjipanayi, M., Georghiou, G., 2013. Calibration of spectroradiometers for outdoor direct solar spectral irradiance measurements. In: 28th European Photovoltaic Solar Energy Conference and Exhibition, Paris, France. pp. 3466–3471.
- WDC, 2015. Global ozone monitoring experiment GOME-2. <https://wdc.dlr.de/sensors/gome2/>, accessed: 2015-05-25.
- Xia, X., Chen, H., Goloub, P., Zhang, W., Chatenet, B., Wang, P., 2007. A compilation of aerosol optical properties and calculation of direct radiative forcing over an urban region in northern China. *J. Geophys. Res-Atmos.* 112.

7 CV

Personal Information

Name: Giorgio Belluardo
Nationality: Italian
Date of birth: 08.07.1982 in Siracusa (Italy)

Professional Qualification and Education

From 04/2013 Doctoral Student of Natural Sources and Life Science
University BoKu, Vienna (Austria)

Focus: study of the effect of solar spectrum variability on PV performance; spectral modelling

07/2013 Summer school “From Renewable Energy Production to End Users”
COST Action ES1002 “Wire”
Montegut (France)

Forecast of renewable energy production for wind and solar energy for the efficient management of electrical grids; measurement techniques

06/2012 – 08/2012 Innovation School 2012
TIS Innovation Park, Bolzano
EURAC Research, Bolzano (Italy)

Training on innovative technologies for sustainable buildings

03/2009 – 07/2009 Renewable Energy Technician
AgenForm s.r.l., Cuneo (Italy)

Training in photovoltaics, solar thermal, biomass energy valorisation and energy efficiency in buildings

12/2004 – 03/2008 Environmental Engineer (Master)
Curriculum of Prediction and Prevention of Hydrogeological Hazards
Università degli Studi di Brescia – Facoltà di Ingegneria,
Brescia (Italy)

10/2001 – 11/2004 Environmental Engineer (Bachelor)
Curriculum of Sanitary Engineering
Università degli Studi di Brescia – Facoltà di Ingegneria,
Brescia (Italy)

09/1996 – 07/2001 High School Diploma
Liceo Scientifico

Istituto Superiore Statale “Lorenzo Lotto”, Trescore Balneario
(Italy)

Work Experience and Internships

From 11/2011 Researcher in the field of Photovoltaic Systems
Institute for Renewable Energy - EURAC Research, Bolzano
(Italy)

Focus: monitoring of photovoltaic systems; analysis of performance and reliability; irradiation data acquisition, handling and mining

11/2013 – 10/2014 Research Collaborator
Photovoltaic Systems Unit - AIT, Vienna (Austria)

Focus: simulation of solar spectra in Vienna under real outdoor conditions

09/2012 Innovation School 2012 internship
Leitner Solar SpA, Brunico (Italy)

Development of innovative concepts concerning efficient use of energy in the residential sector

05/2010 – 04/2011 Sales Export Trainee
alfasolar GmbH, Hanover (Germany)

Focus: configuration and sale of photovoltaic systems; technical support to costumers

09/2009 – 03/2010 Intern and collaborator on European Projects within a non-
governmental organisation
KMGNE gGmbH, Berlin (Germany)

Focus: communication projects on climate change and sustainable lifestyles

07/2009 Collaborator on European and Regional Projects
Is.pa.ro. Società Cooperativa Sociale – Onlus, Corte Franca
(Italy)

Focus: energetic valorisation of vegetal and animal biomass

06/2008 – 01/2009 Temporary Research Associate in Hydraulics
Università degli Studi di Brescia – Facoltà di Ingegneria,
Brescia (Italy)

Focus: field study of the hydrodynamics of Lake Iseo (north Italy)

Languages

Italian as mother tongue
English: Cambridge ESOL Examinations – CAE (advanced)
German: Goethe Zertifikat C1
Basic Spanish knowledge (A2)

IT-skills

Microsoft Office, Outlook, Internet, LaTeX
AutoCad, gnuplot, Unix Shell Scripting, PV*Sol, Sage
ArcGis and Python: basic knowledge